

Jan 22 1979

Item 830-H-15

NASA 6011317

NASA Technical Paper 1317

**COMPLETED**  
ORIGINAL

# Experimental Perfect-Gas Study of Expansion-Tube Flow Characteristics

Judy L. Shinn and Charles G. Miller III

DECEMBER 1978

**NASA**

88

**NASA Technical Paper 1317**

# **Experimental Perfect-Gas Study of Expansion-Tube Flow Characteristics**

**Judy L. Shinn and Charles G. Miller III**  
*Langley Research Center*  
*Hampton, Virginia*



National Aeronautics  
and Space Administration

**Scientific and Technical  
Information Office**

1978

## SUMMARY

An experimental investigation of flow characteristics in the Langley expansion tube has been performed using helium as the test gas and acceleration gas. The use of helium, which behaves ideally for the conditions encountered in this study, eliminates complex real-gas chemistry in the comparison of measured and predicted flow quantities. The driver gas was unheated helium at a nominal pressure of 33 MN/m<sup>2</sup>. Flow diagnostics used to examine flow characteristics were time histories of tube-wall pressure, pitot pressure, and tube-wall heat transfer; incident shock velocity measurements; and pitot-pressure profiles measured at several locations downstream of the tube exit. The quiescent test-gas pressure was varied from 0.7 to 50 kN/m<sup>2</sup> and quiescent acceleration-gas pressure from 2.5 to 53 N/m<sup>2</sup>. The effects of tube-wall boundary-layer growth and finite secondary-diaphragm opening time were examined through the variation of the quiescent gas pressures and secondary-diaphragm thickness. Optimum operating conditions were also sought.

The results indicate that the optimum operating conditions defined for a test time of 300  $\mu$ s are 3.45 kN/m<sup>2</sup> for quiescent test-gas pressure and 16 N/m<sup>2</sup> for quiescent acceleration-gas pressure. Pitot-pressure surveys indicate the existence of a laterally and axially uniform test core having a diameter approximately half the tube diameter and a length up to 16 cm downstream of the tube exit. The tube-wall boundary-layer growth introduces a downstream-facing expansion wave, which causes significant attenuation in the incident shock velocity and reduction in wall pressure along the tube. Comparisons of measured wall pressure at several locations along the acceleration section with theory which was corrected for the effect of flow attenuation support the hypothesis that the test gas was processed by a reflected shock from the secondary diaphragm. The theory of Mirels was used to infer the test-gas velocity from the measured shock velocity. The dip observed in pitot-pressure time history appears to be the result of the tube-wall boundary-layer transition and is clearly not due to nonequilibrium flow chemistry. The effect of inviscid wave interaction near the secondary diaphragm due to the finite secondary-diaphragm opening time was found to be significant. Use of a heavy secondary diaphragm also caused a severe deficit in the measured pitot pressure immediately behind the interface.

## INTRODUCTION

With the launch of Sputnik by the U.S.S.R. 2 decades ago came a sense of urgency for ground-based experimental facilities that could provide information on the level of heating and the aerodynamic performance of vehicles entering the atmosphere of Earth. This need stimulated the development of different types of hypersonic, high-enthalpy facilities which simulated or duplicated certain aspects of the entry phenomena.

In the early 1950's, a unique method of generating hypersonic and hypervelocity flow by energy addition to a supersonic flow was proposed (ref. 1). The

energy-addition mechanism was an unsteady expansion wave which transfers energy from one part of a test gas to another part. The first detailed analytical study of such a device was performed by Trimpi (ref. 2), who named this device an expansion tube. The expansion tube may be thought of as two shock tubes in tandem. During the first phase of the flow sequence, the test gas is the driven gas and is heated by an incident shock wave; during the second phase, the shock-heated test gas becomes the driver gas. Using existing shock-tube technology, Trimpi demonstrated, analytically, the potential of the expansion tube to duplicate velocity in ambient atmospheric conditions for Earth entry from orbit and lunar reentry. Advantages and disadvantages or problem areas of the expansion tube are discussed in reference 2. This facility appeared to circumvent many of the difficulties associated with high-enthalpy facilities in which energy is added to the test gas at stagnation and then the gas is expanded through a nozzle to generate supersonic or hypersonic flow conditions. The proposed method of using an unsteady expansion process to generate hypersonic-hypervelocity flow was received favorably by the scientific community, as evident by a number of conversions of shock tubes to expansion tubes in the early 1960's. (For example, see ref. 3.) Experimenters sought to determine what real-life limitations might restrict the predicted performance of the expansion tube.

The theoretical analysis of reference 2 was idealized, in that viscous effects, finite diaphragm opening times, chemical relaxation rates, and departure from one-dimensional, isentropic flow were neglected. In general, relatively poor agreement between predicted (ref. 2) and measured expansion-tube performance was observed. (See ref. 4.) Thus, the experimenters were confronted with the problem of uncoupling these phenomena to determine the contribution of each to the differences observed between measurement and prediction. One problem area which received considerable attention was flow chemistry. Because of the rapid expansion of the flow through the expansion fan, vibrational relaxation and dissociative recombination may lag translation, resulting in a nonequilibrium unsteady expansion process. Bounds on the effect of flow chemistry on predicted expansion-tube performance are established by considering an equilibrium expansion process and a frozen expansion process (refs. 4 to 6). As demonstrated in references 4 to 8, the uncertainty of the thermochemical state of the test gas during the unsteady expansion process results in a large, corresponding uncertainty in predicted flow conditions. In a recent study (ref. 9), shock shapes about blunt bodies were obtained in the Langley expansion tube using several test gases, one of which was helium. Helium was used primarily to provide (1) a lower limit to the range of normal-shock density ratio and (2) comparison with perfect-gas flow-field predictions, since the helium flow behaved as a perfect gas (was not ionized). Thus, the versatility of the expansion tube in performing aerothermodynamic studies is greatly enhanced by using helium as the test gas. To perform such studies requires optimization of test flow conditions by variation of the initial pressures in the intermediate and acceleration sections of the expansion tube for given tube lengths and driver condition. Also, using a test gas and acceleration gas that behave as a perfect gas throughout the expansion-tube flow sequence eliminates the complex problem of nonequilibrium flow effects. Although other nonideal flow phenomena are not uncoupled, use of a perfect gas as the test gas should provide an improved understanding of the gas dynamics of the expansion-tube flow sequence.



The purpose of this report is to present results obtained using helium as the test gas and acceleration gas in the Langley expansion tube. Comparisons of measured flow quantities with idealized prediction (ref. 5) are performed, and possible explanations for differences observed in these comparisons are discussed. The effects of quiescent test-gas pressure, quiescent acceleration-gas pressure, secondary-diaphragm thickness, and axial station downstream of the tube exit on flow characteristics are presented. Measured time histories of test-section pitot pressure and tube-wall pressure are used to define the period of quasi-steady flow, and pitot-pressure profiles are used to determine the test-core size and flow uniformity. The variation in flow velocity along the tube is examined and the flow velocity at the test section is used in conjunction with the pressure measurements to compute test-section flow conditions according to the method of reference 10.

Use of trade names or names of manufacturers in this report does not constitute an official endorsement of such products or manufacturers, either expressed or implied, by the National Aeronautics and Space Administration.

#### SYMBOLS

$a$	speed of sound, m/s
$\vec{C}_1$	contact surface between test gas and driver gas
$l$	distance between incident shock in acceleration section and acceleration-gas/test-gas interface, m
$M$	Mach number
$N_{Re}$	unit Reynolds number, per meter
$p$	static pressure, N/m <sup>2</sup>
$p_t$	pitot pressure, N/m <sup>2</sup>
$\dot{q}$	heat-transfer rate, W/m <sup>2</sup>
$r$	expansion-tube inside radius, m
$\vec{R}_1$	reflected shock from secondary diaphragm
$\vec{R}_1'$	partially reflected wave from contact surface between test gas and driver gas
$\vec{s}_1$	incident shock in test gas
$\vec{s}_{10}$	incident shock in acceleration gas
$T$	temperature, K
$t$	time after arrival of incident shock into acceleration gas, s

U	velocity, m/s
V	output of heat-transfer gage, volts
W	secondary-diaphragm thickness, m
x	horizontal distance from tube centerline, m
$z_d$	distance measured downstream from diaphragm (secondary diaphragm in expansion tube), m
$z_e$	position of survey rake measured downstream from acceleration-section exit, m
$\gamma$	ratio of specific heats
$\tau$	time interval between arrival of incident shock into acceleration gas and arrival of acceleration-gas/test-gas interface, s
$\psi$	time interval between arrival of acceleration-gas/test-gas interface and tail of expansion fan, s
$\Omega$	measured time interval over which test flow is quasi-steady, s

#### Subscripts:

$t$	tube centerline
e	acceleration-section exit
I	interface
max	maximum
s	incident shock
w	tube wall
1	state of quiescent test gas in front of incident shock in intermediate section
2	state of test gas behind incident shock in intermediate section
2r	state of test gas behind totally reflected shock at secondary diaphragm
4	driver-gas conditions at time of primary-diaphragm rupture
5	state of test-gas flow at free-stream conditions
5,t	stagnation conditions behind bow shock of model positioned at test section

- 10 state of quiescent acceleration gas in front of incident shock in acceleration section
- 20 state of acceleration gas behind incident shock in acceleration section

#### FACILITY

The Langley expansion tube is basically a cylindrical tube divided by two diaphragms (primary and secondary) into three sections. The upstream section is the driver, or high-pressure, section. This section is pressurized at ambient temperature with a gas having a high speed of sound. (Greater operation efficiency is realized as driver-gas speed of sound increases.) The intermediate section is sometimes referred to as the driven section. This section is evacuated and filled with the desired test gas at ambient temperature. The driver and intermediate sections are separated by double diaphragms. The downstream section is referred to as the acceleration, or expansion section. A weak, low-pressure diaphragm (secondary diaphragm) separates the driven and acceleration sections. Test models are positioned at the exit of the acceleration section. Flow through this section exhausts into a dump tank; hence, models are tested in an open jet. A detailed description of the basic components and auxiliary equipment of the Langley expansion tube is presented in reference 11.

For the present tests, the driver section was 2.44 m long and was 16.51 cm in diameter. Double-diaphragm mode of operation was employed to reduce randomness in pressure ratio across the primary diaphragm at time of rupture. Stainless steel primary diaphragms were 2.54 mm thick from the driver-section side to the bottom of cross-pattern grooves on the driven-section side. The volume of the section between the double diaphragms was small compared with that of the driver section, with the ratio of double-diaphragm-section volume to driver-section volume being 0.07. Intermediate-section length was 7.49 m and acceleration-section length was 14.13 m. The inside diameter of these two sections was 15.24 cm. The secondary diaphragm was Mylar,<sup>1</sup> ranging in thickness from 3.175 to 25.4  $\mu$ m.

Briefly, the operating sequence for the expansion tube, which is shown schematically in figure 1, begins with rupture of the high-pressure primary diaphragm. In the double-diaphragm mode of operation, this is achieved by pressurizing the driver section and double-diaphragm section with the driver gas to a pressure somewhat less than the rupture pressure for a single diaphragm. The double-diaphragm section is then isolated from the driver section and high-pressure supply field and the driver section is pressurized to the desired pressure. The double-diaphragm section is then vented to atmospheric pressure, resulting in the rupture of the upstream diaphragm. Upon rupture of this diaphragm, the downstream diaphragm is subjected to a pressure essentially that of the driver section. This pressure ruptures the downstream diaphragm,

---

<sup>1</sup>Mylar: Registered trademark of E. I. du Pont de Nemours & Co., Inc.

and an incident shock wave is propagated into the test gas. The shock wave then encounters and ruptures the low-pressure secondary diaphragm. A secondary incident shock wave propagates into the low-pressure acceleration gas, while an upstream expansion wave moves into the test gas. In passing through this upstream expansion wave, which is being washed downstream since the shock-heated test gas is supersonic, the test gas undergoes an isentropic unsteady expansion resulting in an increase in the flow velocity and Mach number.

## INSTRUMENTATION

### Survey Rake

Horizontal pitot-pressure profiles at the test section were measured with the 11-probe survey rake shown in figure 2(a). This rake had a probe spacing of 1.78 cm and the outside diameter of each probe at the sensing surface was 0.79 cm (fig. 2(b)). The centerline of the center probe was coincident with the expansion-tube centerline. As shown in figure 2(b), a perforated disk arrangement was used to protect the pressure instrumentation from particle contamination in the flow. (Sources of particle contamination were steel slivers from along the rupture line of the primary diaphragm and Mylar fragments from the secondary diaphragm. Tests with the secondary diaphragm removed have demonstrated that this diaphragm is the principal source of particle contamination. These particles are believed to arrive at the test section after the quasi-steady test period.) For results presented herein, the sensing surfaces of the survey-rake probes were positioned from 0.76 to 21.05 cm downstream of the tube (acceleration-section) exit.

### Incident Shock Velocity

A conventional means of determining incident shock velocity is to position high-frequency-response transducers along the length of the tube at known intervals. This procedure allows a distance-time history to be generated; hence, the average incident shock velocity is determined between successive instrumented stations. This is known as time-of-arrival (TOA) measurement. The time interval for incident shock arrival between stations in the intermediate section was determined from the response of piezoelectric (quartz) pressure transducers mounted along the tube flush with the tube wall. Pressure transducers and thin-film resistance heat-transfer gages were used along the acceleration section. Station locations of pressure transducers and thin-film heat-transfer gages in terms of axial distance downstream from the most downstream primary diaphragm are presented in table I. Outputs from these instruments started and stopped counter-timers and were recorded from an oscilloscope with the aid of a camera. The times for the shock to travel between stations were obtained from manual reading of the oscilloscope films and from counter-timer readings.

To enable fast time sweeps of the oscilloscopes monitoring the transducer outputs along the entire tube, output signals from certain transducers were used as trigger signals. These signals triggered downstream oscilloscopes directly or through a digital time delay generator. The counter-timers were all started by the output of a pressure transducer located 3.5 m downstream of

the primary diaphragm in the intermediate section, and each counter-timer was stopped upon shock arrival by the signal output from the pressure transducer at a given axial station.

#### Pitot-Pressure and Wall-Pressure Measurement

Pitot pressures and tube-wall pressures were measured with commercially available miniature quartz piezoelectric transducers. These transducers were acceleration-compensated and had rise times of approximately 1 to 3  $\mu$ s. Each transducer was used in conjunction with a charge amplifier, and the output signal was recorded from an oscilloscope with the aid of a camera. A low-pass filter with an upper cutoff of 100 kHz was used with each tube-wall pressure transducer; similarly, low-pass filter with a cutoff of 50 kHz was used with each pitot-probe transducer.

Each pressure transducer used in the survey rake was calibrated statically after assembly and positioning in the expansion tube; thus, the transducer, charge amplifier, connecting cables, and oscilloscope were calibrated as a single channel of output. Pitot-pressure transducers were calibrated periodically during the test series. Tube wall-pressure transducers and associated charge amplifiers were calibrated statically before and after the test series.

Because the piezoelectric type of transducer is sensitive to temperature, thermal protection in the form of a circular piece of electrical tape was placed over the sensing surface of each transducer. Prior to installation in the pitot-probe tip or tube wall, vacuum grease was applied over the electrical tape on the sensing surface and compressed to fill any voids around the cylindrical part of the transducer containing the sensing surface and the mount for the transducer. The vacuum grease was partially removed, leaving a thin layer over the tape. This simple method for thermal protection proved to be relatively efficient for the present tests. However, occasional breakdown of such protection was detected between runs when a "saddle" appeared in wall-pressure time history. In such cases, a repeat run was made after replacement of the thermal insulator.

#### Quiescent Pressure and Temperature Measurements

Driver-section and double-diaphragm-section pressures were measured with strain-gage transducers statically calibrated to 68.95 MN/m<sup>2</sup>. Quiescent test-gas and acceleration-gas pressures were measured with variable-capacitance diaphragm-type transducers. Driver-section temperature was measured with a bare-wire chromel-alumel thermocouple inserted approximately 6 cm through the upstream end plate of the driver section. The thermocouple junction was exposed directly to the driver gas to provide the fast response required to obtain temperature histories during pressurization of the driver section. This thermocouple output was read from a compensated digital readout and recorded on a strip chart. Quiescent test-gas temperature was measured with a chromel-alumel thermocouple encased in a stainless steel shroud and inserted into the dump tank.



## DATA REDUCTION AND UNCERTAINTY

### Incident Shock Velocity

An average shock velocity between stations was determined by knowing the distance between stations and the time for the shock wave to travel this distance. These times were obtained from the response of transducers along the walls of the intermediate and acceleration sections. The output of these transducers was recorded on oscilloscope films and the times displayed on counter-timers. Uncertainties in transducer response, oscilloscope time scale, and reading of oscilloscope film are believed to result in a corresponding uncertainty in time interval between arrival of the shock wave at successive stations of less than  $\pm 5 \mu\text{s}$ . Uncertainty in oscilloscope time scale was reduced by using a timing mark generator to supply a known time increment to the oscilloscope. If necessary, a correction was applied to film readings. The principal sources of error for times obtained from the counter-timers are response of the transducers and associated equipment and counter-timer sensitivity to this response. For both the oscilloscope films and the counter-timer readings, uncertainties in shock velocity depend on the distance between successive stations, being larger for stations closer together. Since the smallest distance between successive stations used in this study was 1.88 m, the average velocity between stations is believed to be accurate to within 2.5 percent.

As discussed subsequently, values of the incident shock velocity  $U_{s,1}$  immediately prior to shock arrival at the secondary diaphragm and of the incident shock velocity  $U_{s,10}$  at the exit of the acceleration section are required to predict expansion-tube flow conditions. These values of shock velocity were obtained by plotting the shock velocity as a function of axial station and performing an extrapolation to the secondary-diaphragm location or the tube exit.

### Pitot Pressure and Wall Pressure

A sketch of the ideal pitot pressure at the acceleration-section exit, corresponding to the expansion-tube flow sequence shown in figure 1, is shown in figure 3 as a function of time. Upon arrival of the incident shock, a sharp increase in pressure occurs. Because of the low value of quiescent acceleration-gas pressure  $p_{10}$ , the magnitude of this pressure increase is relatively small. Following a period of constant pressure, a second sharp increase in pressure occurs. This second increase, which is much larger in magnitude than the first, corresponds to the arrival of the acceleration-gas/test-gas interface. Following the interface arrival, the test-gas pitot pressure is constant over the time interval  $\psi$ . This period of constant pressure represents the useful test time and is terminated by the arrival of the tail of the expansion fan.

Oscilloscope films of pitot-pressure and tube-wall-pressure traces were read manually. Uncertainties in such pressure measurements are dependent on many factors, such as calibration technique (static or dynamic), change in calibration factor during course of tests, transducer linearity, oscilloscope accuracy, quality of oscilloscope traces with respect to the signal-to-noise ratio, and oscilloscope film reading procedure. Hence, specifying precise

uncertainties for these pressure measurements is not possible. On the basis of this and previous experience, the maximum uncertainties in pressure measurements are believed to be less than  $\pm 20$  percent for acceleration-section wall pressure and less than  $\pm 10$  percent for pitot pressure.

Pitot-pressure time histories were also used to determine the time interval between arrival of the incident shock into the acceleration gas and arrival of the acceleration-gas/test-gas interface  $\tau$ . (See fig. 3.) The significance of this measurement in inferring the interface velocity  $U_i$  from the measured incident shock velocity  $U_{s,10}$  is discussed subsequently. Although the value of pitot pressure immediately behind the shock  $P_{t,20}$  could not be obtained fully before the arrival of the interface because of the long time constant associated with the pitot-probe configuration shown in figure 2(b), values of  $\tau$  were obtained accurately from pitot-pressure time histories.

## PREDICTION METHODS

### Isentropic Unsteady Expansion

The expansion-tube test-flow conditions can be predicted by performing an isentropic, unsteady expansion from the conditions of the test gas immediately prior to rupture of the secondary diaphragm to the test-region velocity (refs. 2, 4, and 5). The program of reference 5 was used for the present study. The assumed cases for the conditions of the test gas prior to the expansion were no shock reflection, a totally reflected shock, and a standing shock at the secondary diaphragm. (The predicted results for the present helium tests are essentially the same for the assumed case of a standing shock as for the case of no reflected shock and thus only results of no shock reflection and a totally reflected shock are presented herein.)

The importance of measurement accuracy of the incident shock velocity in the intermediate section  $U_{s,1}$  was emphasized in reference 12. In figure 4, an example is given to illustrate that a small uncertainty in  $U_{s,1}$  results in a rather large uncertainty in the predicted free-stream quantities for helium test gas. The free-stream static pressure  $p_5$  and pitot pressure  $P_{t,5}$  are shown as functions of free-stream velocity  $U_5$ . The shaded region in figure 4 denotes the uncertainty in  $p_5$  and  $P_{t,5}$  due to an assumed uncertainty of  $\pm 3$  percent in  $U_{s,1}$ . At a velocity of 7.0 km/s, typical of the present tests, the uncertainty in  $p_5$  is approximately  $\pm 45$  percent, and in  $P_{t,5}$ ,  $\pm 20$  percent. Thus, to minimize uncertainties in predicted expansion-tube test-section flow quantities, the incident shock  $U_{s,1}$  must be measured as accurately as possible.

In reference 4, it was shown that the acceleration-gas/test-gas interface velocity, as well as shock velocity, attenuates as the shock travels the length of the acceleration section, and a method for determining the effect of flow

attenuation on thermodynamic quantities in region (5) was discussed. This method, used in this study, is based on the concept that the flow attenuation

is due to a downstream-facing expansion wave generated by the growing boundary layer upstream.

#### "Data Reduction Procedure" for Determining Free-Stream Conditions

Significant differences between measured test-section flow quantities and predicted (ref. 5) test-section flow quantities based on upstream flow conditions were observed in the Langley pilot model expansion tube (refs. 4, 7, and 8) and in the Langley expansion tube (refs. 9 and 11). In order to provide a means for obtaining accurate test-section conditions, computational schemes for real-gas mixtures (ref. 10) based on flow properties measured in the immediate vicinity of the test section were derived. These schemes eliminate an explicit dependence upon measured or calculated upstream flow properties and thereby result in a substantial reduction in the uncertainty in predicted test-section flow conditions. They are based on combinations of three flow parameters measured at the test section. The three measured expansion-tube flow parameters serving as input to these schemes for the present study are pitot pressure  $P_{5,t}$ , free-stream static pressure  $p_5$ , and free-stream velocity  $U_5$ . The free-stream static pressure is assumed to be equal to the expansion-tube-wall pressure measured just upstream of the test section. This assumption is subject to question for a test flow whose free-stream Mach number exceeds approximately 8 with a turbulent boundary layer along the tube wall (refs. 13 and 14). However, the boundary layer is laminar through the useful test region for the present tests, so this assumption is believed to be valid. The free-stream velocity is assumed to be equal to the acceleration-gas/test-gas interface velocity  $U_I$ , which is inferred from the measured incident shock velocity  $U_{s,10}$ . The method of inferring  $U_I$  from  $U_{s,10}$  is presented in the next section.

#### Test-Gas Velocity

The free-stream velocity  $U_5$ , a basic quantity of interest, is the flow velocity immediately behind the acceleration-gas/test-gas interface. The interface velocity is assumed to be a good representation of the flow immediately behind the interface; that is,  $U_I \sim U_5$ . Although the incident shock velocity in the acceleration section was measured for each test, the interface velocity was not measured. To determine free-stream velocity and to compare measured and predicted expansion-tube flow properties, it is necessary to determine interface velocity accurately.

Interface velocity must be deduced from the measured incident shock velocity. Ideal shock-tube theory shows that the separation distance between the shock and interface increases linearly with distance from the diaphragm station (refs. 15, 16, and 17). However, tube-wall boundary-layer growth behind the incident shock introduces departures from ideal shock-tube flow. The presence of this boundary layer causes the incident shock to decelerate, the interface to accelerate, and the flow between the incident shock and interface to be non-uniform. The deviation of separation distance between the incident shock and interface from idealized (inviscid) shock-tube flow for the case of a tube-wall boundary layer was studied analytically by Mirels for a laminar boundary layer

(ref. 15) and a turbulent boundary layer (ref. 16). However, no extensive experimental verification of these analytical methods has been performed for the rather unique (that is, helium test gas) conditions of this study. Thus, a number of tests were performed with the secondary diaphragm removed, so the facility was operated as a shock tube with helium test gas; results are presented in the appendix.

When the wall boundary-layer thickness is large in comparison with the tube diameter, the separation distance between the incident shock and the interface  $\bar{l}$  and the corresponding time interval  $\tau$  approach limiting maximum values. The maximum separation distance  $\bar{l}_{\max}$  estimated by Mirels using the local similarity approximation is given by equations (2) and (17) of reference 15 for a laminar boundary layer and by equations (2) and (17) of reference 16 for a turbulent boundary layer. With the calculated value of  $\bar{l}_{\max}$ , the separation distance  $\bar{l}$  and the corresponding time interval  $\tau$  can be found as functions of the distance measured downstream from the diaphragm  $x_d$  through equations (20) and (22) of reference 15 for a laminar boundary layer and equations (22b) and (23) of reference 16 for a turbulent boundary layer. The corresponding interface velocity  $U_I$  is then obtained by dividing  $\bar{l}$  by  $\tau$ .

A method for estimating flow nonuniformity (axial variation of flow quantities) between the incident shock and the interface after maximum separation distance is reached was presented in references 15, 18, and 19. In these references, the concept of an equivalent inviscid channel was employed. The continuity equation, isentropic relation, and momentum equation are used to solve for the density, pressure, and flow velocity at a given distance from the incident shock with known values of the density, pressure, and flow velocity immediately behind the incident shock.

Measured flow quantities between the incident shock and the interface both in an expansion tube and a shock tube (see appendix) are compared with values predicted from the equations from references 15 and 16. This comparison provides a basis for accurately determining the interface velocity from the measured incident shock velocity into the quiescent acceleration gas. The flow velocity between the interface and expansion fan (fig. 3) is assumed to be constant. However, it should be noted that such an assumption is subject to question (ref. 20). Uncertainties in calculated free-stream and post-normal-shock flow conditions due to uncertainties in the experimental input  $U_5$ , as well as inputs  $p_5$  and  $p_{t,5}$ , have been examined for helium test gas in reference 9. The result of reference 9 reveals that an uncertainty of  $\pm 2.5$  percent in  $U_5$  causes an uncertainty of  $\pm 5$  percent at most for all the free-stream and post-normal-shock flow quantities.

#### Conventional Shock-Tube Theory

A simple method for predicting the free-stream pressure  $p_5$  is to calculate the static pressure immediately behind the incident shock at the test section and correct it to the value at the test-gas/acceleration-gas interface using the results given in reference 19. This corrected value is then the predicted free-stream pressure  $p_5$ , when  $p_5$  is assumed to be equal to  $p_{20}$  at the interface. To find the static pressure immediately behind the incident



shock in the acceleration gas, conventional shock-tube theory was applied. That is, the shock-tube phase of the program of reference 5 was used with the following inputs: (1) incident shock velocity in the acceleration gas, (2) quiescent acceleration-gas pressure, and (3) quiescent acceleration-gas temperature. This method of predicting free-stream pressure  $p_5$  is completely different from that of the unsteady expansion process because of its independence of the upstream flow history.

## TESTS

For the present tests, the helium driver gas was drawn from a high-pressure supply (10:1) at ambient temperature, and no external heat was applied. Approximate driver pressure at the time of diaphragm rupture  $p_4$  was 33 MN/m<sup>2</sup>. High-purity (99.998 percent pure) helium was employed as the test gas and acceleration gas. The intermediate section was evacuated to less than 0.1 N/m<sup>2</sup> before filling it with the test gas, and the acceleration section and dump tank were evacuated to less than 0.01 N/m<sup>2</sup> before filling them with the acceleration gas. Quiescent test-gas pressure  $p_1$  was varied from 0.7 to 50 kN/m<sup>2</sup> and quiescent acceleration-gas pressure was varied from 2.5 to 53 N/m<sup>2</sup>. Secondary diaphragm thicknesses of 3.18, 6.35, 12.70, and 25.40  $\mu$ m were tested. As a supplement, a number of tests were performed without a secondary diaphragm for helium test gas and the quiescent test-gas pressure was varied from 0.035 to 6.87 kN/m<sup>2</sup>, as described in the appendix.

Driver-gas pressure  $p_4$  and temperature  $T_4$  at the time of primary-diaphragm rupture, quiescent test-gas pressure  $p_1$ , quiescent acceleration-gas pressure  $p_{10}$ , secondary-diaphragm thickness  $W$ , and survey-rake station  $z_e$  are presented in table II for the present tests. Also presented in this table are measured values of the incident shock velocity in the intermediate section  $U_{s,1}$  immediately upstream of the secondary diaphragm, incident shock velocity at the exit of the acceleration section  $U_{s,10,e}$ , acceleration-section wall pressure near the exit, assumed to be free-stream static pressure  $p_5$ , and an average value of the pitot pressure across the test core  $P_{5,t}$ .

## RESULTS AND DISCUSSION

### Effect of Quiescent Acceleration-Gas Pressure

Incident shock velocity.— In expansion-tube operation, the expansion fan which passes through the shocked test gas raises the gas to a higher velocity while expanding it to a lower temperature and pressure. The final state after expansion depends on a number of factors, one of the more important being the density of the quiescent acceleration gas. Figure 5(a) illustrates the effect of quiescent acceleration-gas pressure  $p_{10}$  on the incident shock velocity measured at the tube exit  $U_{s,10,e}$ , and figure 5(b) illustrates the variation of incident shock velocity along the acceleration section  $U_{s,10}$  for several values of quiescent acceleration-gas pressure. Values of  $U_{s,10}$  and  $U_{s,10,e}$  were obtained with time-of-arrival (TOA) measurements. The quiescent test-gas pressure was 3.45 kN/m<sup>2</sup> and the secondary diaphragm was 6.35- $\mu$ m-thick Mylar. The incident shock velocity at the exit decreases with increasing quiescent



acceleration-gas pressure (fig. 5(a)), and the attenuation of incident shock velocity along the driven section (fig. 5(b)) increases with increasing quiescent acceleration-gas pressure. Although there is no TOA measurement within 2 m downstream of the secondary diaphragm, as shown in figure 5(b), velocity trends in this region were obtained by microwave interferometer measurement (ref. 4). Apparently, the ionization level in the shock front was sufficient for microwave reflection because of contamination in the helium acceleration gas. The microwave results indicate that the incident shock velocity begins to increase sharply at the secondary-diaphragm station and peaks 1 to 2 m downstream. Therefore, the TOA measurement at  $z_d = 2.25$  m in figure 5(b) is a good representation of the maximum incident shock velocity along the acceleration section. Figure 5(c) shows the effect of quiescent acceleration-gas pressure on total attenuation of the incident shock velocity (i.e., the decrease of the incident shock velocity from its maximum value along the acceleration section to the value at the tube exit). The total shock attenuation is observed to increase linearly with  $p_{10}$ . The present  $\Delta U_{s,10}$  for  $p_{10} = 22 \text{ N/m}^2$  is larger than that observed in reference 9.

Inferred interface velocity.— As mentioned in the section, "Test-Gas Velocity," the free-stream velocity  $U_5$  is assumed to be equal to the acceleration-gas/test-gas interface velocity  $U_I$ . Since  $U_I$  is not measured, it must be inferred from the measured incident shock velocity in the quiescent acceleration gas  $U_{s,10}$ . This inference of interface velocity may be performed by considering the theoretical results of reference 15. As discussed in the appendix, the boundary layer between the incident shock and the interface is laminar for the present range of  $p_{10}$ . For a laminar boundary layer, the predictions of reference 15 reveal that at the tube exit the interface velocity  $U_I$  is essentially equal to the incident shock velocity  $U_{s,10}$  for the present length of the acceleration section and for quiescent acceleration-gas pressure  $p_{10}$  less than  $50 \text{ N/m}^2$ . Predicted values of  $U_{s,10}/U_I$  as a function of  $p_{10}$  are shown in figure 6 at a distance of 2.25 m downstream of the secondary diaphragm. These results demonstrate that  $U_I$  is within 6 percent of  $U_{s,10}$  at this upstream station for the range of  $p_{10}$  examined, and is within 1 percent for  $p_{10} < 20 \text{ N/m}^2$ . A comparison of predicted (ref. 15) and measured time intervals between arrival of the incident shock and arrival of the acceleration-gas/test-gas interface  $\tau$  is shown in figure 7 as a function of quiescent acceleration-gas pressure. The measured time interval  $\tau$  was obtained from pitot-pressure time histories measured 5.64 cm downstream of the tube exit. In general, predicted time intervals for a laminar boundary layer are observed to be in good agreement with measured time intervals; hence, the assumption that  $U_I$  is equal to  $U_{s,10}$  at the tube exit is verified.

Centerline pitot-pressure time history.— The effect of quiescent acceleration-gas pressure on centerline pitot-pressure time history measured 5.64 cm downstream of the tube exit is shown in figure 8. The quiescent test-gas pressure is  $3.45 \text{ kN/m}^2$  and the secondary diaphragm is 6.35- $\mu\text{m}$ -thick Mylar. At the lower values of  $p_{10}$ , the pitot pressure increases nearly linearly with time and tends to become more constant with time as  $p_{10}$  increases. For values of  $p_{10}$  greater than approximately  $10 \text{ N/m}^2$ , the period of quasi-steady test flow  $\Omega$  diminishes with increasing  $p_{10}$  as a "dip" in pitot-pressure time history appears. This dip was also observed in the Langley pilot model expansion tube (ref. 4) with air test gas, and although the subject of much

concern, the cause of this dip was never clearly determined. The present results eliminate flow chemistry as a contributor. The spikes appearing in figure 8 are believed to be characteristic of the flow and not the arrangement used to protect the pressure transducer from solid flow contaminants in the post-test period. This belief is based on the absence of spikes for tests run without a secondary diaphragm (shock-tube mode of operation), for which the flow about the pitot probes was supersonic and the pressure magnitude similar to that presented in figure 8. The value of  $p_{10}$  which generates the best flow conditions, from the viewpoint of a compromise between constant pitot pressure with time and duration of quasi-steady flow, is believed to be around  $16 \text{ N/m}^2$ .

Lateral variation of pitot-pressure time history.— Pitot-pressure time histories measured with the 11-probe survey rake  $5.64 \text{ cm}$  downstream of the tube exit are shown in figure 9 for several values of  $p_{10}$ . Time histories for pitot probes positioned the same distance on both sides of the center probe are shown on the same plot. For all values of  $p_{10}$ , the results of figure 9 imply the absence of asymmetric flow since the time histories for corresponding pitot probes are quite similar. As expected, the outermost probes, which were outside the bore of the tube, registered very little pressure. The probes adjacent to these outermost probes experienced a lower level of pitot pressure than the seven innermost probes.

At the lowest value of  $p_{10}$  (fig. 9(a)), a quasi-steady flow period, in terms of pitot pressure, is not achieved. For  $p_{10}$  equal to  $26.45$  and  $52.60 \text{ N/m}^2$  (figs. 9(b) and 9(c)), the time characteristics of pitot pressure for the center five probes are similar. Although the pitot pressure during the quasi-steady flow period of the probes adjacent to the center five probes is similar to that of these five probes, the decrease in pressure following this quasi-steady period appears to arrive earlier; that is, the dip condition for the center five probes arrives around  $230 \mu\text{s}$  after incident shock arrival, whereas for the adjacent probes it arrives around  $160 \mu\text{s}$ . This phenomenon of earlier dip arrival for the probes closer to the tube wall has also been reported in reference 21. Coinciding with the dip in pitot pressure are larger oscillations in pitot pressure. At the highest value of  $p_{10}$  (fig. 9(c)), there is some indication that the center five probes detect interface arrival somewhat earlier than adjacent probes; this implies that the interface is not one-dimensional.

Transition phenomenon and pitot-pressure dip.— In reference 4, it was hypothesized that the dip in pitot pressure is the result of transition of the tube-wall boundary layer. Representative time histories of acceleration-section wall heat-transfer rate are shown in figure 10 for several values of  $p_{10}$ . These measurements were made  $1.88 \text{ m}$  upstream of the tube exit. The heat-transfer rate increases markedly upon arrival of the incident shock, decays monotonically to an essentially constant value with time, and then experiences a second pronounced increase. The time interval between the incident shock and the second increase in heat-transfer rate diminishes with increasing  $p_{10}$ , being approximately  $650 \mu\text{s}$  for the lowest value of  $p_{10}$  and  $250 \mu\text{s}$  for the highest value. If this increase in heat-transfer rate is inferred as the start of transition, then the location of transition becomes closer to the incident shock with increasing  $p_{10}$  just as the location of the pitot-pressure dip does in

figure 8. In figure 11, time histories of heat-transfer rate are shown for several stations downstream of the secondary diaphragm for the highest value of  $p_{10}$  examined. The time interval between shock-wave arrival and the second increase in heat-transfer rate, in general, decreases with increasing distance from the diaphragm. This phenomenon, being in agreement with the observation reported in reference 21, indicates that the dip is the result of transition of the tube-wall boundary layer.

Wall-pressure time history near test section.— Time histories of the acceleration-section wall pressure measured 2.54 cm upstream of the tube exit are shown in figure 12 for various values of  $p_{10}$ . Also shown are predicted values of static pressure behind the incident shock into the acceleration gas. These predictions were obtained from conventional shock-tube theory corrected to the value at the interface using the method of reference 19. In general, the measured tube-wall pressure is characterized by a sharp increase upon incident shock arrival followed by a slight decrease to a relatively constant pressure and then a gradual increase due to the arrival of the expansion fan. At the lowest value of  $p_{10}$ , the tube-wall pressure increases linearly with time. The initial spike occurring upon shock arrival becomes more pronounced with increasing  $p_{10}$ . A second sharp increase in pressure, which is explained in a subsequent section as the result of interaction between the reflected shock and the contact surface near the secondary diaphragm, is observable within the given time frame for a number of values of  $p_{10}$ . These measured tube-wall pressures are, in general, in fairly good agreement with the predicted values but are slightly higher than predicted for low values of  $p_{10}$ . For  $p_{10} = 10.61 \text{ N/m}^2$ , agreement is poorest. Outgassing from the acceleration-section and the dump-tank walls is believed to be the main cause for higher measured values. The minimal rate of outgassing was measured to be  $600 (\mu\text{N/m}^2)/\text{s}$ . A nominal time of roughly 300 s elapsed between initiation of filling the acceleration section with helium and the rupture of the primary diaphragm to begin the flow sequence. Hence, contamination by water as high as 8 percent may have existed for the lowest value of  $p_{10}$ . A computation based on 2-percent water contamination in helium was performed for  $p_{10} = 10.61 \text{ N/m}^2$ , and the result indicated a 14-percent increase in  $p_{20}$  over the prediction for pure helium.

Wall-pressure time history at various stations.— Time histories of acceleration-section wall pressure at various stations downstream of the secondary diaphragm are shown in figure 13 for a quiescent acceleration-gas pressure equal to  $16.00 \text{ N/m}^2$ . At a distance only 0.07 m downstream of the secondary diaphragm, the tube-wall pressure is of the same order of magnitude as the tube-wall pressure in the intermediate section. By the time the flow has traveled 3.43 m downstream of the secondary diaphragm, it has expanded, so that the tube-wall pressure is approximately 0.03 times that in the intermediate section. The acceleration-section wall pressure increases rapidly upon incident shock arrival, remains nearly constant, then increases. The rate of the second increase in pressure with time, which is often due to the arrival of the expansion fan, decreases with distance downstream and the period of nearly constant pressure increases. The value of constant pressure decreases with distance downstream of the secondary diaphragm by about 30 percent for the present conditions.

To account for such decrease in wall pressure with distance downstream of the secondary diaphragm, comparison is made in figure 14 between measurements



and predictions (ref. 5) which include the correction for flow attenuation suggested in reference 4. The data shown correspond to the measured tube-wall pressure and interface velocity (which is assumed equal to the flow velocity in region (5),  $U_5$ ) inferred from the measured incident shock velocity at each axial station. The solid lines are the predicted static pressure in region (5)

$p_5$  as a function of  $U_5$  for the cases of reflected shock and no shock reflection from the secondary diaphragm. The maximum value of inferred interface velocity (or maximum value of  $U_5$ ) along the acceleration section was found to be 7180 m/s. The dashed lines, which are obtained by a reflection of solid lines at maximum value of  $U_5$  to account for a downstream-facing expansion wave which produces the decay in interface velocity, represent the prediction corrected for flow attenuation. Such reflection is equivalent to shifting from point  $(p_5, U_{5,\max} + \Delta U_5)$  to point  $(p_5, U_{5,\max} - \Delta U_5)$ . The predictions were generated using the method of reference 5 where the basic input was  $U_{s,1}$ . Although the data are in very good agreement with the prediction for reflected shock, it is important to note that a systematic error of 3.5 percent in  $U_{s,1}$  would cause the overlap between predictions for reflected shock and for no shock (see the example in fig. 4).

Test-core diameter. - A major consideration in expansion-tube flow characteristics is the existence of a uniform test core. Horizontal pitot-pressure profiles are shown in figure 15 for various values of  $p_{10}$ . These profiles were measured 150  $\mu$ s after incident shock arrival at the pitot-pressure probes. The results of figure 15 demonstrate the existence of a region of constant pitot pressure about the tube centerline for all values of  $p_{10}$ . The test-core diameter was defined as the diameter of the region about the tube centerline for which the pitot pressure is within 10 percent of the average of the center three pitot-pressure probes. Because of the relatively large probe spacing and nature of the pitot-pressure distributions, the boundaries of the test core cannot be determined accurately. The core diameter increased from 3.6 cm at the lowest value of  $p_{10}$  to 8.9 cm at the highest value. Except for the lowest value of  $p_{10}$ , the test-core diameter was approximately half the tube diameter. For the present tests, the free-stream Reynolds number based on pitot-probe sensing-surface diameter is greater than  $2 \times 10^3$ . Thus, the present pitot-pressure measurements within the test core should be essentially free from rarefied flow effects (ref. 22).

Free-stream parameters. - The free-stream Mach number and unit free-stream Reynolds number for the range of  $p_{10}$  are shown in figure 16. These free-stream parameters were determined using the method of reference 10 with the following measured inputs: (1) average pitot pressure across the test core, (2) acceleration-section wall pressure near the tube exit, and (3) incident shock velocity in the acceleration gas at the tube exit. (The last two input quantities have been deduced to be the free-stream pressure and velocity. As shown in the figure, free-stream Mach number decreases with increasing  $p_{10}$ , while the unit Reynolds number stays rather constant except for the lowest value of  $p_{10}$ .)

## Effect of Quiescent Test-Gas Pressure

Incident shock velocity.— Flow properties behind the incident shock into the test gas were varied by varying the quiescent test-gas pressure  $p_1$  and maintaining a nearly constant helium driver pressure  $p_4$  of about 33 MN/m<sup>2</sup>. The range of incident shock velocity in the intermediate section  $U_{s,1}$  generated by varying the pressure ratio across the primary diaphragm is shown in figure 17. For tests designed to examine the effect of quiescent test-gas pressure (range of  $p_1$  tested is from 0.7 to 50 kN/m<sup>2</sup>) the quiescent acceleration-gas pressure  $p_{10}$  was 16.00 N/m<sup>2</sup> and the secondary-diaphragm thickness was 6.35  $\mu$ m for  $p_1$  less than 20 kN/m<sup>2</sup> and 12.70  $\mu$ m or 25.4  $\mu$ m for  $p_1$  greater than 20 kN/m<sup>2</sup>. As discussed in reference 12 and the appendix, the measured shock velocity accelerates initially and then decelerates with distance downstream from the primary diaphragm. Also, the maximum value of shock velocity occurs closer to the primary diaphragm as  $p_1$  increases. The measured maximum shock velocity may be determined to within 3 percent from the expression

$$M_{s,1} = 0.223 \log_e \frac{p_4}{p_1} + 1.975 \quad (1)$$

which was obtained from a curve fit. These maximum values of  $U_{s,1}$  are observed (fig. 17) to exceed predictions from conventional shock-tube theory (ref. 5); possible causes of this discrepancy are discussed in reference 12. One possible cause is that the driver-gas temperature  $T_4$  is greater than ambient temperature. Although the helium driver is unheated, the temperature of the driver gas exceeds ambient temperature at the time of diaphragm rupture as recorded routinely by a thermocouple gage in the driver section. In reference 12, the heating of the helium driver gas upon pressurization of the driver section was attributed in part to the Joule-Thomson coefficient being negative for helium and partly to compression heating. As shown in figure 18, tests made with thermocouple gages located at both ends of the driver section revealed the existence of a pronounced axial temperature gradient which implies that the heating is due primarily to compression. The increase in driver-gas temperature near the filling port, which is located in the upstream end of the driver section, is less than that experienced at the diaphragm end of the driver section. Figure 18 demonstrates that the initial quantity of driver gas leaving the driver section may be at a temperature as high as 350 to 390 K, instead of 330 K as in reference 12. However, comparison of measured values of  $U_{s,1}$  with predicted values based on  $T_4$  equal to 390 K shows that the elevated driver temperature cannot fully account for the discrepancy (fig. 17).

Measured incident shock velocity into the acceleration gas  $U_{s,10}$  at a distance of 2.25 m downstream of the secondary diaphragm and at the tube exit is shown in figure 19 as a function of  $p_1$ . As observed in reference 23, the incident shock velocity into the acceleration gas  $U_{s,10}$  decreases monotonically with increasing  $p_1$ . For the present tests, a monotonic decrease in  $U_{s,10}$  was observed for  $p_1$  greater than 3 kN/m<sup>2</sup>. For  $p_1$  less than 3 kN/m<sup>2</sup>, although the attenuation of the shock velocity along the intermediate section is small (see the appendix and ref. 12),  $U_{s,10}$  decreased with decreasing  $p_1$ .



The variation of  $U_{s,10}$  with  $p_1$  may be predicted by the expression,

$$\frac{p_1}{p_{10}} = \left( 1 + \sqrt{\frac{\gamma-1}{2\gamma}} - \sqrt{\frac{\gamma-1}{2\gamma}} \frac{a_{10}}{a_1} \frac{M_{s,10}}{M_{s,1}} \right)^{-2\gamma/(\gamma-1)} \left( \frac{M_{s,10}}{M_{s,1}} \right)^2 \quad (2)$$

which was derived using conventional, ideal-gas shock-tube relations (ref. 19) for a strong incident shock and assuming no shock reflection at the secondary diaphragm. A plot of equation (2) reveals that the amplification of shock Mach number across the secondary diaphragm  $M_{s,10}/M_{s,1}$  is unity when  $p_1/p_{10} = 1.0$  and increases monotonically with  $\log_e (p_1/p_{10})$ , approaching

$$\frac{a_1}{a_{10}} \left( 1 + \sqrt{\frac{2\gamma}{\gamma-1}} \right)$$

as  $p_1/p_{10}$  approaches infinity. This functional behavior is similar to that of the conventional, ideal-gas shock-tube relation across the primary diaphragm as  $M_{s,1}$  is plotted against  $\log_e (p_4/p_1)$ . At the lower test values of  $p_1$ , the decrease of  $p_1$  results in more reduction in  $M_{s,10}/M_{s,1}$  than the gain in  $M_{s,1}$  (as can be seen from a plot of  $M_{s,10}/M_{s,1}$  against  $\log_e (p_1/p_{10})$  and a plot of  $M_{s,1}$  against  $\log_e (p_4/p_1)$ ). Therefore,  $M_{s,10}$  which has the overall effect from  $M_{s,10}/M_{s,1}$  and  $M_{s,1}$  decreases with decreasing  $p_1$ . Figure 19 also shows that the decrease in  $U_{s,10}$  as the shock travels from 2.25 m downstream of secondary diaphragm to the tube exit is rather independent of  $p_1$ . The inferred interface velocity  $U_I$  (ref. 15) is also plotted in figure 19 as a function of  $p_1$ . At the tube exit, the incident shock velocity  $U_{s,10}$  is equal to  $U_I$ , while at a distance of 2.25 m downstream of secondary diaphragm, the ratio of  $U_{s,10}$  to  $U_I$  is within  $1.0082 \pm 0.0007$  for all the values of  $p_1$ .

Reflected shock from secondary diaphragm.— The existence of a reflected shock from the secondary diaphragm is illustrated in figure 20, where the measured intermediate-section wall pressure 11.04 cm upstream of the secondary diaphragm is plotted as a function of time for values of quiescent test-gas pressure  $p_1$  from 0.69 to 10.34 kN/m<sup>2</sup>. Also shown are the static pressures behind the incident shock and behind a totally reflected shock predicted by assuming that the reflected shock velocity is not affected by the expansion wave following the secondary-diaphragm rupture. The secondary-diaphragm opening time, defined as the time interval between the incident shock reflection and the completion of the secondary-diaphragm rupture, is inversely proportional to the square root of the applied pressure (ref. 24); thus longer opening times are expected for the lower values of  $p_1$ . The longer it takes for the diaphragm to be ruptured and thus for the expansion to take place, the less weakened the reflected shock is by the expansion wave as it travels upstream. Therefore, for the lower values of  $p_1$ , the measured pressure behind the reflected shock agrees better with the prediction.

### Interaction of reflected shock and driver-gas/test-gas contact surface.-

In figure 21, time histories of tube-wall pressure in the acceleration section are shown at various axial stations downstream of the secondary diaphragm for several values of quiescent test-gas pressure  $p_1$ . At the lowest value of  $p_1$ , a second, pronounced increase in wall pressure occurs at the two stations closest to the secondary diaphragm. These time histories for  $p_1 = 0.69 \text{ kN/m}^2$  indicate the existence of a disturbance which probably originated in the vicinity of the secondary diaphragm and which travels at a speed in excess of that of the incident shock into the acceleration gas and overtakes the incident shock between stations 5.63 and 7.75 m downstream of the secondary diaphragm. This disturbance is also observed for  $p_1 = 1.74 \text{ kN/m}^2$ . In this case, the disturbance propagates further behind the incident shock than that observed for  $p_1 = 0.69 \text{ kN/m}^2$ , and it overtakes the incident shock very near the tube exit. Increasing  $p_1$  to  $2.41 \text{ kN/m}^2$  moves the disturbance even further back from the incident shock, and the shock is not overtaken prior to its arrival at the tube exit.

For lower values of  $p_1$ , it was concluded from figure 20 that the reflected shock from the secondary diaphragm is less affected by the expansion wave as it travels upstream. In figure 21, the disturbance in tube-wall pressure in the acceleration section was observed closer behind the incident shock for lower values of  $p_1$ . The origin of this disturbance can be found by considering characteristic wave interaction in the vicinity of the secondary diaphragm for a low value of  $p_1$ . In figure 22, the distance-time diagram is plotted for

$p_1 = 0.69 \text{ kN/m}^2$ . The trajectories of the incident shock into the test gas  $\vec{S}_1$ , the reflected shock from the secondary diaphragm  $\vec{R}_1$ , the partially reflected wave from the contact surface  $\vec{R}_1'$ , and the incident shock into the acceleration gas  $\vec{S}_{10}$  are from direct measurement while that of the contact surface  $\vec{C}_1$  is inferred from shock-tube measurement. Region (2) denotes the test gas behind the incident shock in the intermediate section and region (3) denotes the expanded driver gas. The reflected wave  $\vec{R}_1'$  from the interaction of  $\vec{C}_1$  and  $\vec{R}_1$  can be a shock wave or an expansion wave depending on whether the acoustic impedance in region (2)  $I_2$  is smaller or greater than that in region (3)  $I_3$  (refs. 25 and 26), where

$$I_i = \frac{1}{a_i} \left\{ \gamma_i \left[ (\gamma_i + 1) + (\gamma_i - 1) \frac{P_2}{P_{2r}} \right] \right\}^{1/2} \quad (i = 2, 3)$$

Since  $\gamma_2 = \gamma_3$  and  $a_2 > a_3$ , it follows that  $I_2 < I_3$ . Therefore,  $\vec{R}_1'$  is a shock wave which causes a rise in wall pressure upon its arrival. The trajectory of  $\vec{R}_1'$  in figure 22 reveals that  $\vec{R}_1'$  is accelerated by the expansion fan.

Wall-pressure time history near test section.- Tube-wall-pressure time histories measured just 2.54 cm upstream of the tube exit are shown in figure 23 for the range of quiescent test-gas pressure  $p_1$ . Also shown with the dashed line are the static pressures behind the incident shock predicted by conventional shock-tube theory corrected to the value at the interface by the method of reference 19. From figure 21, it is known that the disturbance has overtaken the incident shock quite a distance upstream of the tube exit for the lowest value of  $p_1$  shown in figure 23; the wall pressure near the tube exit therefore represents the pressure rise due to the resultant shock wave. The wall pressure for  $p_1 = 1.74 \text{ kN/m}^2$  is greater than expected; such increase implies that the disturbance has overtaken the incident shock about the time the flow exits the tube. At  $p_1 = 2.41$  and  $3.45 \text{ kN/m}^2$ , the second, pronounced increase in wall pressure appears further behind the incident shock but disappears within the time frame of test flow for higher values of  $p_1$ . As  $p_1$  increases further, the pressure is constant behind the incident shock and then increases. This increase is believed to correspond to the arrival of the expansion fan. The time interval between arrival of the incident shock and arrival of the expansion fan appears to decrease with increasing  $p_1$ .

Centerline pitot-pressure time history.- Measured centerline pitot-pressure time histories are shown in figure 24 for the range of quiescent test-gas pressure  $p_1$ . The results of figure 21 show that the disturbance has overtaken the incident shock quite a distance upstream of the tube exit for the lowest  $p_1$ , had overtaken the incident shock near the tube exit for the next higher value of  $p_1$ , and was roughly  $200 \mu\text{s}$  behind the incident shock at the tube exit for  $p_1 = 2.41 \text{ kN/m}^2$ . The pitot-pressure time history for  $p_1 = 2.41 \text{ kN/m}^2$  shows the arrival of a family of pressure spikes approximately  $200 \mu\text{s}$  after shock arrival. This family of spikes is attributed to arrival of the disturbance. The arrival of pressure spikes is delayed approximately  $100 \mu\text{s}$  by increasing the quiescent test-gas pressure to  $3.45 \text{ kN/m}^2$ . Further increase in quiescent test-gas pressure proves detrimental to flow quality, as determined from the pitot-pressure time histories. Thus, from figures 21 and 24, optimum quality flow may be obtained for  $p_1 = 3.45 \text{ kN/m}^2$  for a test time of approximately  $300 \mu\text{s}$ .

Test-core diameter.- Horizontal pitot-pressure profiles measured at a test time of  $150 \mu\text{s}$  are shown in figure 25 for the range of quiescent test-gas pressure  $p_1$ . The pitot-pressure profiles for all values of  $p_1$  greater than  $2.4 \text{ kN/m}^2$  are similar and the pitot pressure within the test core increases with increasing  $p_1$ . For  $p_1 = 0.69$  and  $1.74 \text{ kN/m}^2$ , the pitot-pressure profiles, measured after the disturbance has overtaken the shock, are different from those for  $p_1$  greater than  $2.4 \text{ kN/m}^2$ .

Free-stream parameters.- The free-stream Mach number and unit free-stream Reynolds number are shown in figure 26 as a function of quiescent test-gas pressure  $p_1$ . These free-stream parameters were determined using the method

of reference 10 as described in a previous section. Although the results of figure 19 show that the flow velocity decreases slightly with increasing  $p_1$  for  $p_1$  greater than  $3 \text{ kN/m}^2$ , the free-stream Mach number increases with increasing  $p_1$ . This implies that the speed of sound and therefore the temperature of the flow decreases with increasing  $p_1$ , as expected.

#### Effect of Secondary-Diaphragm Thickness

Reflected shock from secondary diaphragm.- In a previous section, the disturbance in the acceleration section flow (fig. 21) was attributed to the finite secondary-diaphragm opening time. Since the diaphragm opening time is proportional to the square root of the diaphragm thickness, its effect on the strength of the reflected shock (and therefore, on the closeness of the disturbance to the incident shock into the acceleration gas) can be varied, theoretically, by varying only the diaphragm thickness (that is, maintaining constant driver pressure, quiescent test-gas pressure, and quiescent acceleration-gas pressure). Figure 27 shows the wall-pressure time histories measured 11.04 cm upstream of the secondary diaphragm with thicknesses ranging from 3.18 to 25.40  $\mu\text{m}$  and a quiescent test-gas pressure equal to  $2.07 \text{ kN/m}^2$ . With increasing secondary-diaphragm thickness, the measured, second wall-pressure rise behind the arrival of reflected shock increases. This implies that the thicker the secondary diaphragm, the longer the diaphragm opening time and, thus, the less weakened the reflected shock by the expansion wave following diaphragm rupture.

Interaction of reflected shock and driver-gas/test-gas contact surface.- As these reflected shocks of different strengths travel upstream and interact with the contact surface, they are partially reflected from the contact surface with different strengths and time lags behind the incident shock into the acceleration gas. The subsequent disturbances from this reflection can be seen accelerating through the expansion fan in figures 28, 29, and 30. In figure 28, time histories of tube-wall pressure in the acceleration section are shown at various axial stations downstream of the secondary diaphragm and for diaphragm thicknesses of 3.18 and 25.40  $\mu\text{m}$ . For the thinnest diaphragm, the disturbance travels much further behind the incident shock than for the thickest diaphragm and is about 200  $\mu\text{s}$  behind the incident shock at the station nearest to the tube exit. For the diaphragm thickness equal to 25.40  $\mu\text{m}$ , the disturbance has overtaken the incident shock between 9.95 m and 12.24 m downstream of the secondary diaphragm. In figure 29, the time histories of tube-wall pressure measured just 2.54 cm upstream of the tube exit are shown for the various secondary-diaphragm thicknesses. For the two thickest diaphragms, the disturbance has overtaken the incident shock, so that the measured wall pressure is higher than expected. For the diaphragm thickness of 6.35  $\mu\text{m}$ , the disturbance is approximately 100  $\mu\text{s}$  behind the incident shock. In figure 30, the measured time histories of centerline pitot pressure are shown for the same values of diaphragm thickness. The increase in pitot pressure due to the disturbance corresponds to that in wall pressure shown in figure 29, except for the occurrence of a family of spikes associated with the disturbance and of the pitot dip. As the dip occurrence is found to be related to transition of the tube-wall boundary layer, it is interesting to note that the dip follows closely behind the disturbance for various diaphragm thickness.



Test-flow quality.— To determine the effect of secondary-diaphragm thickness on the test flow without the interference of the disturbance, tests were made with moderately higher quiescent test-gas pressures for a reasonable range of diaphragm thickness. In figure 31, measured time histories of wall pressure just 2.54 cm upstream of the tube exit and time histories of centerline pitot pressure are shown for diaphragm thicknesses of 6.35, 12.70, and 25.40  $\mu\text{m}$ . The quiescent acceleration-gas pressure was  $16.00 \text{ N/m}^2$ ; the quiescent test-gas pressure  $p_1$  was  $3.45 \text{ kN/m}^2$  (fig. 31(a)) and  $10.34 \text{ kN/m}^2$  (fig. 31(b)). For the lower value of  $p_1$ , the disturbance can be seen at least  $150 \mu\text{s}$  behind the incident shock for all values of diaphragm thickness, while for  $p_1 = 10.34 \text{ kN/m}^2$ , the disturbance cannot be detected within the time frame of observation. For both values of  $p_1$ , the incident shock velocity at the tube exit and the measured wall pressure behind the incident shock stay rather constant for all the values of diaphragm thickness (see table II)). However, the measured pitot pressure is lowest just behind the interface and gradually increases for the thickest diaphragm. The large deficit in measured pitot pressure near the interface for heavier secondary diaphragms is probably attributable to the large momentum loss associated with rupture of the diaphragm.

#### Axial Variation of Pitot Pressure

To determine the extent of flow variation in the test section of the expansion tube, the survey rake was positioned at various locations downstream of the tube exit and the results are presented in figure 32. The lateral (horizontal) pitot-pressure profiles for a given axial station represent the average of two tests. The quiescent test-gas pressure was  $3.45 \text{ kN/m}^2$  and the quiescent acceleration-gas pressure was  $16.00 \text{ N/m}^2$ . Run-to-run repeatability was good, with the incident shock velocity at the tube exit being within 0.8 percent of  $6962 \text{ m/s}$  for all tests; hence, no correction due to run-to-run variation in flow velocity is applied to the data. For all but the most downstream axial station, the profiles illustrate the existence of a uniform test core having a diameter approximately half the tube diameter. The essentially constant pitot pressure of the center three probes over the range of axial location examined implies the absence of significant expansion of the flow after exiting the tube; however, a decrease in test-core diameter occurs for the most downstream station. Thus, a laterally and axially uniform test core exists for the present expansion-tube tests with helium test gas for distances up to 16 cm downstream of the tube exit.

#### CONCLUDING REMARKS

For the experimental investigation of flow characteristics in the Langley expansion tube, the complex, real-gas problem was eliminated by using helium test gas. The effect of tube-wall boundary-layer growth and finite diaphragm opening time were examined through the variation of quiescent test-gas pressure, quiescent acceleration-gas pressure, and secondary-diaphragm thickness. Optimum operating conditions for helium test gas were also sought. The driver gas was unheated helium at a nominal pressure of  $33 \text{ MN/m}^2$ , and the acceleration gas was also helium. The following conclusions for the contributing factors



responsible for departure from idealized performance predictions in the absence of flow chemistry have been reached:

1. A dip in pitot-pressure time history appears to be the result of tube-wall boundary-layer transition. Nonequilibrium chemistry is clearly not the cause for the dip and for the large pressure oscillation associated with the dip, which were previously observed in other test gas. The time interval between shock-wave arrival and the start of boundary-layer transition decreases with increasing distance from the secondary diaphragm and with increasing quiescent acceleration-gas pressure.

2. The total attenuation of the incident shock along the acceleration section due to viscous effects is significant for helium and increases with increasing quiescent acceleration-gas pressure. The attenuation of the interface (or flow) was inferred by using the theory of Mirels. This inference is believed to be reliable because of the good agreement of the measured time interval between arrival of the incident shock and arrival of the interface with the prediction.

3. The reduction in measured wall pressure as the incident shock and the interface velocity attenuate along the acceleration section is due to a downstream-facing expansion wave. The inclusion of this effect in the idealized unsteady expansion theory results in good agreement between predicted and measured wall pressures at various stations. Furthermore, the data seem to support the prediction for the case of a reflected shock at the secondary diaphragm.

4. Inviscid wave interaction near the secondary diaphragm due to both the finite secondary-diaphragm opening time and the closeness of the driver-gas/test-gas interface to the incident shock is one of the major causes for the deviation from the idealized theory. The effect due to this inviscid wave interaction can be important for other nonperfect test gases.

5. The use of a heavier secondary diaphragm not only increases the diaphragm opening time, causing an undesirable effect of inviscid wave interaction near the secondary diaphragm, but also reduces the test flow quality. Although the measured wall pressure and the incident shock velocity stay rather constant with increasing secondary-diaphragm thickness, the measured pitot pressure decreases severely near the interface. This deficit of pitot pressure just behind the interface is probably attributable to the momentum loss associated with rupture of the Mylar secondary diaphragm, but definitely not to flow chemistry.

The optimum operating conditions defined for a test time of approximately 300  $\mu$ s are 3.45 kN/m<sup>2</sup> for quiescent test-gas pressure and 16 N/m<sup>2</sup> for quiescent acceleration-gas pressure with secondary-diaphragm thickness of 6.35  $\mu$ m or less. The limitations of operating beyond the optimum conditions are partly due to the nonideal flow characteristics, as have already been described. The pitot-pressure dip limits the increase of quiescent acceleration-gas pressure and the inviscid wave interaction near the secondary diaphragm limits the decrease of quiescent test-gas pressure. However, a decrease of quiescent acceleration-gas pressure and an increase of quiescent test-gas pressure would

ideally result in shorter test time because of the higher degree of expansion across the secondary diaphragm. The thinnest possible pinhole-free secondary diaphragm is preferred to yield a better flow quality and to reduce diaphragm opening time.

Lateral pitot-pressure profiles measured at various axial stations downstream of the tube exit show the existence of a laterally and axially uniform test core having a diameter approximately half the tube diameter and a length up to 16 cm downstream of the tube exit. The optimum free-stream quantities measured are approximately 6870 m/s for the flow velocity, 1120 N/m<sup>2</sup> for static pressure and 60 kN/m<sup>2</sup> for the pitot pressure. The calculated free-stream Mach number is 6.0 and unit free-stream Reynolds number is  $3.95 \times 10^5 \text{ m}^{-1}$ .

Langley Research Center  
National Aeronautics and Space Administration  
Hampton, VA 23665  
October 17, 1978

## APPENDIX

### SOME FLOW CHARACTERISTICS BEHIND THE INCIDENT SHOCK IN THE ACCELERATION SECTION OF THE LANGLEY EXPANSION TUBE AS DETERMINED BY SHOCK-TUBE MODE OF OPERATION

To compute flow conditions accurately in the expansion-tube test section using the equilibrium program of reference 10, three flow quantities must be known in the vicinity of the test section (tube exit). The pitot pressure is measured directly, whereas the free-stream static pressure and free-stream velocity must be inferred from measurement. To lend credibility to the assumptions used in obtaining free-stream pressure and velocity, a number of tests were performed with the secondary diaphragm removed (expansion tube operated as a shock tube) and helium used as the test (driven) gas. The quiescent test-gas pressure was varied from 0.035 to 6.87 kN/m<sup>2</sup>. Incident shock velocity, pitot pressure, wall pressure, and wall heat transfer were measured using the same instrumentation as described in the text for the expansion tube. These shock-tube tests provide a base for comparison of measured and predicted flow quantities, which in turn should provide information on the character (laminar or turbulent) of the tube-wall boundary layer. Such data are vital in inferring the interface, or free-stream, velocity from the incident shock velocity and in inferring the free-stream static pressure from the measured tube-wall pressure. The results of these shock-tube tests are discussed as follows.

#### Incident Shock Velocity

Variation of incident shock velocity along the driven section is shown in figure 33 for several values of quiescent test-gas pressure. These values of incident shock velocity were obtained from time-of-arrival measurements. Measured shock velocities increase initially and then decrease with distance downstream of the diaphragm. This trend has been observed and discussed in previous shock-tube investigations (see, for example, ref. 12). The data of figure 33 were employed in the theory of references 15 and 16 to predict the separation distance between the incident shock and test-gas/driver-gas interface and the corresponding test time for laminar and turbulent boundary layers.

#### Pitot-Pressure Time History

The measured test time between the incident shock and interface was inferred from pitot-pressure time histories measured 5.64 cm downstream of the tube exit on the tube centerline. Ideally, the pitot pressure should increase rapidly upon arrival of the test-gas/driver-gas interface since static pressure and velocity are assumed constant across the interface and the flow density (and hence, pitot pressure) is higher in the driver gas. For the present tests, the specific heats of the driver and driven gases are essentially equal, and the volume change at the interface as a result of mixing of the driver and test gases should be zero (ref. 27). Thus, a sharp increase in

pitot pressure should occur upon interface arrival. Measured pitot-pressure time histories are presented in figure 34 for various values of quiescent test-gas pressure  $p_1$ . These measured time histories deviate from the idealized time histories in that the pitot pressure is not constant over the test time and a second, sharp increase in pitot pressure does not occur at the two highest values of  $p_1$ . The monotonic increase in pitot pressure between the incident shock and interface for the lower values of  $p_1$  is attributed to viscous effects. The measured pitot-pressure time history for the lowest value of  $p_1$  is compared with prediction in figure 35. The predicted time history was obtained from reference 19 for a laminar boundary layer and using the Rayleigh pitot formula (ref. 28). Measured and predicted pitot pressures are observed to be in good agreement, which implies that the monotonic increase in pitot pressure with time is due to the growth of the tube-wall boundary layer behind the incident shock.

#### Wall Boundary-Layer Characteristics

At the higher values of  $p_1$  in figure 34, the pitot pressure behind the incident shock is initially constant with time. This period of constant pitot pressure is followed by a nearly linear increase and then a period of large fluctuations. In figures 36 and 37, time histories of the tube-wall pressure and temperature (represented by the voltage change of the sensing element of a thin-film resistance gage mounted flush with the wall) are shown at various distances downstream of the diaphragm and for various quiescent test-gas pressures. Also shown by the broken lines, are the static pressures predicted using conventional shock-tube theory and the incident shock velocity data from figure 33. The agreement is good between the measured and the predicted pressures for all values of  $p_1$ . Although the time histories of  $p_w$  and  $V_w$  are similar for the two lowest values of  $p_1$  (see figs. 36(c) and (d) and figs. 37(c) and (d)), the thin-film resistance gages experience a pronounced increase in voltage during the period of essentially constant wall pressure for the two highest values of  $p_1$  (see figs. 36(a) and (b) and figs. 37(a) and (b)). Thin-film resistance gages are commonly used to obtain the wall temperature history from which the region of transition to turbulent flow is inferred (ref. 29). As the shock wave passes across the gage, a step function in wall temperature occurs which persists until the boundary layer becomes transitional, at which time the wall temperature increases with time. Thus, the results of figures 36(a) and (b) and figures 37(a) and (b) indicate that the first portion of quasi-steady flow behind the incident shock experienced by the pitot-pressure probe for the two highest values of  $p_1$  (see fig. 34) corresponds to a laminar tube-wall boundary layer, whereas the following flow corresponds to a turbulent tube-wall boundary layer.

The time interval between incident shock arrival and departure from a quasi-steady state, as inferred from pitot pressure, tube-wall pressure, and tube-wall temperature measurements are shown in figure 38 as a function of distance downstream of the diaphragm for a range of quiescent test-gas pressure. For the three lowest values of  $p_1$ , the time intervals from the tube-wall pressure and temperature measurements are in good agreement and somewhat larger than that from the pitot pressure. The time intervals from the tube-wall pressure and temperature are also in reasonably good agreement within 18 m

## APPENDIX

of the diaphragm for  $p_1$  equal to  $2.07 \text{ kN/m}^2$ . For  $z_d$  greater than  $18 \text{ m}$ , the wall temperature departs from a quasi-steady state prior to the wall pressure or pitot pressure. (Also, the wall-pressure and pitot-pressure time of departure from a quasi-steady state are essentially equal.) From figures 36 to 38, it is concluded that the tube-wall boundary layer corresponding to the time interval between the incident shock and the interface is laminar for  $p_1$  equal to or less than approximately  $1 \text{ kN/m}^2$  and the tube length of  $21.61 \text{ m}$ . At values of  $p_1$  greater than  $1 \text{ kN/m}^2$ , the boundary layer becomes turbulent before the flow exits the tube.

### Test Time

The time interval between the incident shock and the interface as determined from centerline pitot-pressure measurements is shown in figure 39 as a function of quiescent test-gas pressure. Also shown in this figure are predicted time intervals (refs. 15 and 16) for laminar and turbulent boundary layers. For values of  $p_1$  less than approximately  $1 \text{ kN/m}^2$ , the laminar predictions are in good agreement with measurement, whereas for values of  $p_1$  greater than  $1 \text{ kN/m}^2$ , laminar theory overpredicts measurement. At the higher values of  $p_1$ , the measurement agrees more closely with the turbulent prediction. The comparison of figure 39 supports the conclusion that the tube-wall boundary layer remains laminar for values of  $p_1$  less than  $1 \text{ kN/m}^2$  and demonstrates that the prediction method of reference 15 for a laminar tube-wall boundary layer provides reasonably accurate values of time interval.

### Attainment of Maximum Separation Distance

The ratios of separation distance to maximum separation distance  $\ell/\ell_{\max}$  and of incident shock velocity to interface velocity  $U_{s,1}/U_I$ , predicted from references 15 and 16 are shown in figure 40 as a function of quiescent test-gas pressure  $p_1$ . These predicted values of  $\ell/\ell_{\max}$  and  $U_{s,1}/U_I$  for laminar and turbulent boundary-layer flows correspond to the results presented in figure 39. For values of  $p_1$  less than  $50 \text{ N/m}^2$ , the interface velocity is essentially equal to the incident shock velocity at the tube exit for laminar or turbulent flow. Hence, the test-gas/acceleration-gas interface velocity for the present expansion-tube tests is assumed equal to the measured incident shock velocity at the tube exit for values of quiescent acceleration-gas pressure less than  $50 \text{ N/m}^2$ .



## REFERENCES

1. Hertzberg, A.; Smith, W. E.; Glick, H. S.; and Squire, W.: Modifications of the Shock Tube for the Generation of Hypersonic Flow. AEDC-TN-55-15 (AD-789-A-2), U.S. Air Force, Mar. 1955.
2. Trimpi, Robert L.: A Preliminary Theoretical Study of the Expansion Tube, A New Device for Producing High-Enthalpy Short-Duration Hypersonic Gas Flows. NASA TR R-133, 1962.
3. Fourth Hypervelocity Techniques Symposium - Advanced Experimental Techniques for Study of Hypervelocity Flight. Arnold Eng. Dev. Center, Aro, Inc., and Univ. of Denver, Nov. 1965.
4. Jones, Jim J.; and Moore, John A.: Exploratory Study of Performance of the Langley Pilot Model Expansion Tube With a Hydrogen Driver. NASA TN D-3421, 1966.
5. Miller, Charles G., III: A Program for Calculating Expansion-Tube Flow Quantities for Real-Gas Mixtures and Comparison With Experimental Results. NASA TN D-6830, 1972.
6. Miller, Charles G., III; and Wilder, Sue E.: Program and Charts for Determining Shock Tube, Expansion Tube, and Expansion Tunnel Flow Quantities for Real Air. NASA TN D-7752, 1975.
7. Haggard, Kenneth V.: Free-Stream Temperature, Density, and Pressure Measurements in an Expansion Tube Flow. NASA TN D-7273, 1973.
8. Haggard, Kenneth V.; and Goad, William K.: A Comparison of Measured and Predicted Test Flow in an Expansion Tube With Air and Oxygen Test Gases. NASA TN D-8068, 1975.
9. Miller, Charles G., III: Shock Shapes on Blunt Bodies in Hypersonic-Hypervelocity Helium, Air, and CO<sub>2</sub> Flows, and Calibration Results in Langley 6-Inch Expansion Tube. NASA TN D-7800, 1975.
10. Miller, Charles G., III: Computer Program of Data Reduction Procedures for Facilities Using CO<sub>2</sub>-N<sub>2</sub>-O<sub>2</sub>-Ar Equilibrium Real-Gas Mixtures. NASA TM X-2512, 1972.
11. Moore, John A.: Description and Initial Operating Performance of the Langley 6-Inch Expansion Tube Using Heated Helium Driver Gas. NASA TM X-3240, 1975.
12. Miller, Charles G., III; and Jones, Jim J.: Incident Shock-Wave Characteristics in Air, Argon, Carbon Dioxide, and Helium in a Shock Tube With Unheated Helium Driver. NASA TN D-8099, 1975.

13. Fischer, M. C.; Maddalon, D. V.; Weinstein, L. M.; and Wagner, R. D., Jr.: Boundary-Layer Pitot and Hot-Wire Surveys at  $M_\infty \approx 20$ . AIAA J., vol. 9, no. 5, May 1971, pp. 826-834.
14. Kemp, Joseph H., Jr.; and Owen, F. Kevin: Experimental Study of Nozzle Wall Boundary Layers at Mach Numbers 20 to 47. NASA TN D-6965, 1972.
15. Mirels, Harold: Test Time in Low-Pressure Shock Tubes. Phys. Fluids, vol. 6, no. 9, Sept. 1963, pp. 1201-1214.
16. Mirels, Harold: Shock Tube Test Time Limitation Due to Turbulent-Wall Boundary Layer. AIAA J., vol. 2, no. 1, Jan. 1964, pp. 84-93.
17. Gaydon, A. G.; and Hurle, I. R.: The Shock Tube in High-Temperature Chemical Physics. Reinhold Pub. Corp., 1963.
18. Connor, Laurence N., Jr.; and Andersen, Rolf P.: Real Gas Effects on Shock-Tube Flow Nonuniformity. AIAA J., vol. 8, no. 1, Jan. 1970, pp. 175-177.
19. Mirels, H.: Flow Nonuniformity in Shock Tubes Operating at Maximum Test Times. Phys. Fluids, vol. 9, no. 10, Oct. 1966, pp. 1907-1912.
20. Friesen, Wilfred J.: Use of Photoionization in Measuring Velocity Profile of Free-Stream Flow in Langley Pilot Model Expansion Tube. NASA TN D-4936, 1968.
21. Weilmuenster, K. James: An Experimental Investigation of Wall Boundary-Layer Transition Reynolds Numbers in An Expansion Tube. NASA TN D-7541, 1974.
22. Bailey, A. B.; and Boylan, D. E.: Some Experiments on Impact-Pressure Probes in a Low-Density, Hypervelocity Flow. AEDC-TN-61-161, U.S. Air Force, Dec. 1961.
23. Miller, Charles G.: Operational Experience in the Langley Expansion Tube With Various Test Gases. NASA TM-78637, 1977.
24. Simpson, C. J. S. M; Chandler, T. R. D.; and Bridgman, K. B.: Effect on Shock Trajectory of the Opening Time of Diaphragms in a Shock Tube. Phys. Fluids, vol. 10, no. 9, Sept. 1967, pp. 1894-1896.
25. Polachek, H.; and Seeger, R. J.: On Shock-Wave Phenomena; Refraction of Shock Waves at a Gaseous Interface. Phys. Rev., second ser., vol. 84, no. 5, Dec. 1, 1951, pp. 922-929.
26. Matsuo, Kazuyasu; Kage, Kazuyuki; and Kawagoe, Shigetoshi: The Interaction of a Reflected Shock Wave With the Contact Region in a Shock Tube. Bull. JSME, vol. 18, no. 121, July 1975, pp. 681-688.

27. White, Donald R.: Influence of Diaphragm Opening Time on Shock-Tube Flows. J. Fluid Mech., vol. 4, pt. 6, Nov. 1958, pp. 585-599.
28. Ames Research Staff: Equations, Tables, and Charts for Compressible Flow. NACA Rep. 1135, 1953. (Supersedes NACA TN 1428.)
29. Hartunian, R. A.; Russo, A. L.; and Marrone, P. J.: Boundary-Layer Transition and Heat Transfer in Shock Tubes. J. Aerosp. Sci., vol. 27, no. 8, Aug. 1960, pp. 587-594.

TABLE I.- LOCATION OF GAGES USED TO GENERATE TIME-OF-ARRIVAL DATA

Station	Distance downstream from primary diaphragm, m	Type of gage	
		Pressure transducer	Heat-transfer gage
8	3.493	✓	
11	4.405	✓	
13	5.373	✓	
14	6.246	✓	
15	6.924	✓	
18	7.38	✓	
Secondary diaphragm	7.45		
19	7.568	✓	
20	8.637		✓
21	10.921	✓	✓
23	13.126	✓	✓
24	15.246	✓	✓
25	17.447	✓	✓
26	18.735		✓
27	19.732	✓	✓
28	20.090	✓	
29	20.445	✓	
30	20.802	✓	
31	21.286	✓	
32	21.584	✓	
Tube exit	21.610		



TABLE II.- EXPANSION-TUBE TESTS

Run	P <sub>4</sub> , MN/m <sup>2</sup>	T <sub>4</sub> , K	P <sub>1</sub> , kN/m <sup>2</sup>	P <sub>10</sub> , N/m <sup>2</sup>	W, μm	U <sub>s,1</sub> , m/s (a)	U <sub>s,10,e</sub> , m/s	P <sub>5</sub> , N/m <sup>2</sup> (b)	P <sub>5,t</sub> , kN/m <sup>2</sup> (c)	z <sub>e</sub> , cm
19	33.25	334.8	3.43	2.52	6.35	4132	7725	390	35.3	5.64
17	33.25	337.6	3.44	5.26	6.35	4180	7325	586	47.9	5.64
18	33.65	332.6	3.45	7.91	6.35	4202	7185	700	53.2	5.64
16	33.25	328.7	3.45	10.61	6.35	4183	6900	989	57.5	5.64
14	33.25	-----	3.45	16.00	6.35	4154	6870	1120	60.1	5.64
43	33.52	339.8	3.43	15.94	12.70	4216	6875	1024	44.6	5.64
44	33.65	335.4	3.44	16.06	25.40	4185	6945	1024	36.1	5.64
11	32.17	322.0	3.48	21.34	6.35	4268	6760	1431	65.1	5.64
20	33.39	338.2	3.45	26.45	6.35	4198	6540	1524	66.6	5.64
21	33.12	333.7	3.44	31.33	6.35	4183	6510	1669	67.3	5.64
22	32.98	-----	3.45	42.13	6.35	4208	6310	2130	67.1	5.64
23	33.52	338.7	3.44	52.60	6.35	4106	6100	2613	74.7	5.64
25	33.65	336.5	.69	16.03	6.35	4343	<sup>d</sup> 7200	814	26.5	5.64
24	33.12	330.4	1.74	16.32	6.35	4203	6840	<sup>d</sup> 1358	<sup>d</sup> 45.6	5.64
39	33.65	335.9	2.05	15.91	3.18	4200	6830	772	47.0	5.64
38	33.65	334.3	2.05	15.89	6.35	4205	6890	876	44.5	5.64
36	33.52	337.6	2.06	15.86	12.70	4222	6890	<sup>d</sup> 1296	<sup>d</sup> 63.5	5.64
37	33.52	335.9	2.08	15.84	25.40	4171	<sup>d</sup> 8150	<sup>d</sup> 1296	<sup>d</sup> 57.1	5.64
26	33.39	337.0	2.41	15.98	6.35	4178	6890	938	46.9	5.64
29	32.71	332.6	4.82	16.16	6.35	4097	6925	958	74.9	5.64
30	33.52	343.7	10.34	15.89	6.35	3748	6775	989	103.6	5.64
223	32.43	324.8	10.48	16.50	6.35	3743	6745	1076	97.9	8.17
224	32.30	322.6	10.48	16.33	12.70	3713	6745	1086	92.6	8.17
225	32.44	320.9	10.45	16.08	25.40	3713	6821	1086	85.1	8.17
31	32.57	335.9	20.62	15.95	6.35	3375	6625	1010	122.9	5.64
32	33.52	334.3	30.89	15.88	12.70	3181	6325	886	131.2	5.64
33	33.52	339.8	49.85	15.93	25.40	2993	6315	1162	132.2	5.64
142	32.30	327.6	3.43	15.96	6.35	4139	6943	1024	58.0	.76
134	31.90	327.0	3.48	15.99	6.35	4049	6905	1003	57.4	5.64
136	33.52	335.9	3.44	16.24	6.35	4124	6930	932	57.4	10.92
138	32.71	325.9	3.45	16.04	6.35	4109	6905	932	60.4	16.00
140	32.17	328.7	3.48	16.00	6.35	4094	6930	982	59.3	21.08

<sup>a</sup>Measured at secondary-diaphragm station.<sup>b</sup>Measured acceleration-section wall pressure near tube exit.<sup>c</sup>Average value of pitot pressure across test core.<sup>d</sup>Anomalous value due to inviscid wave interaction.

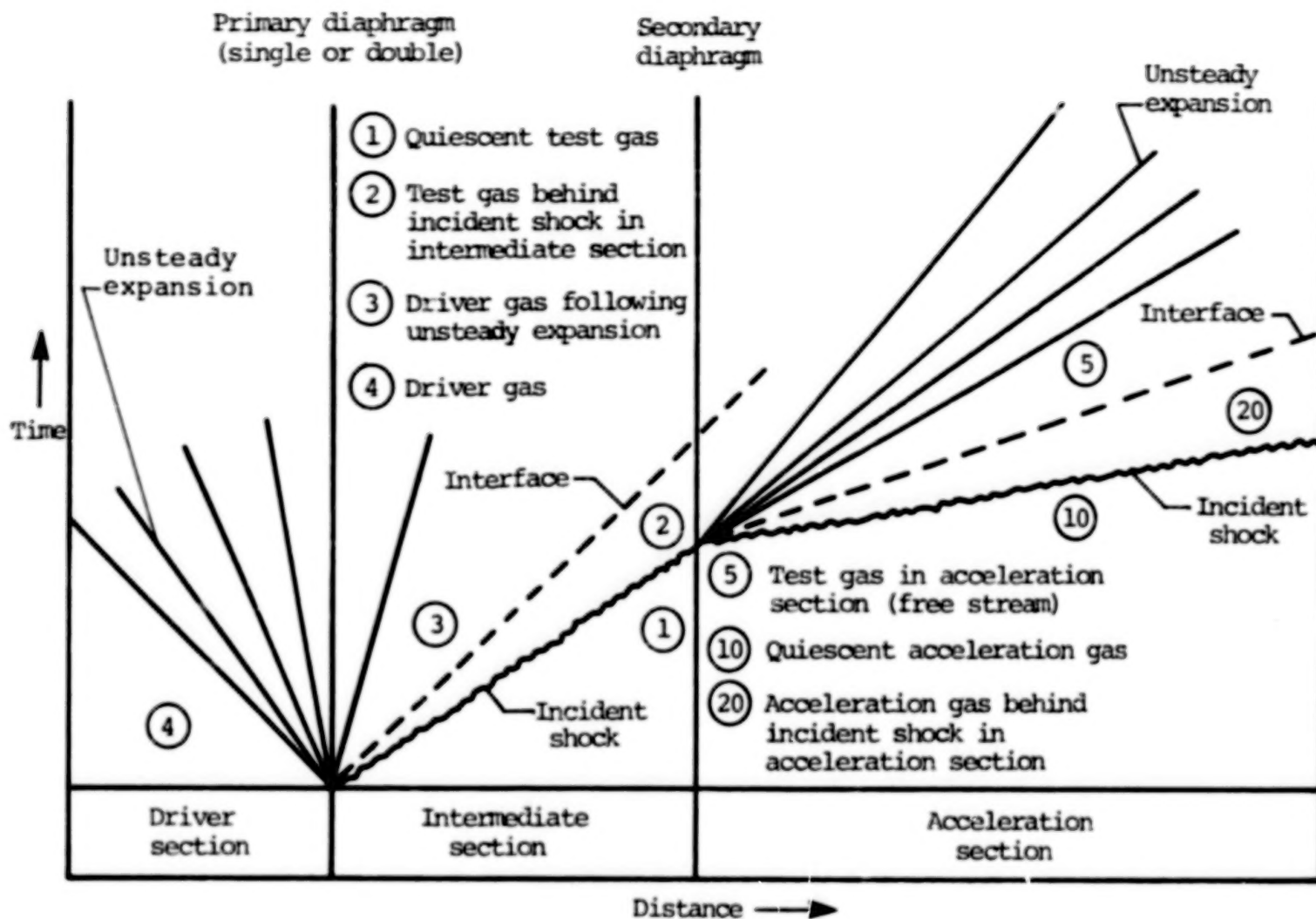
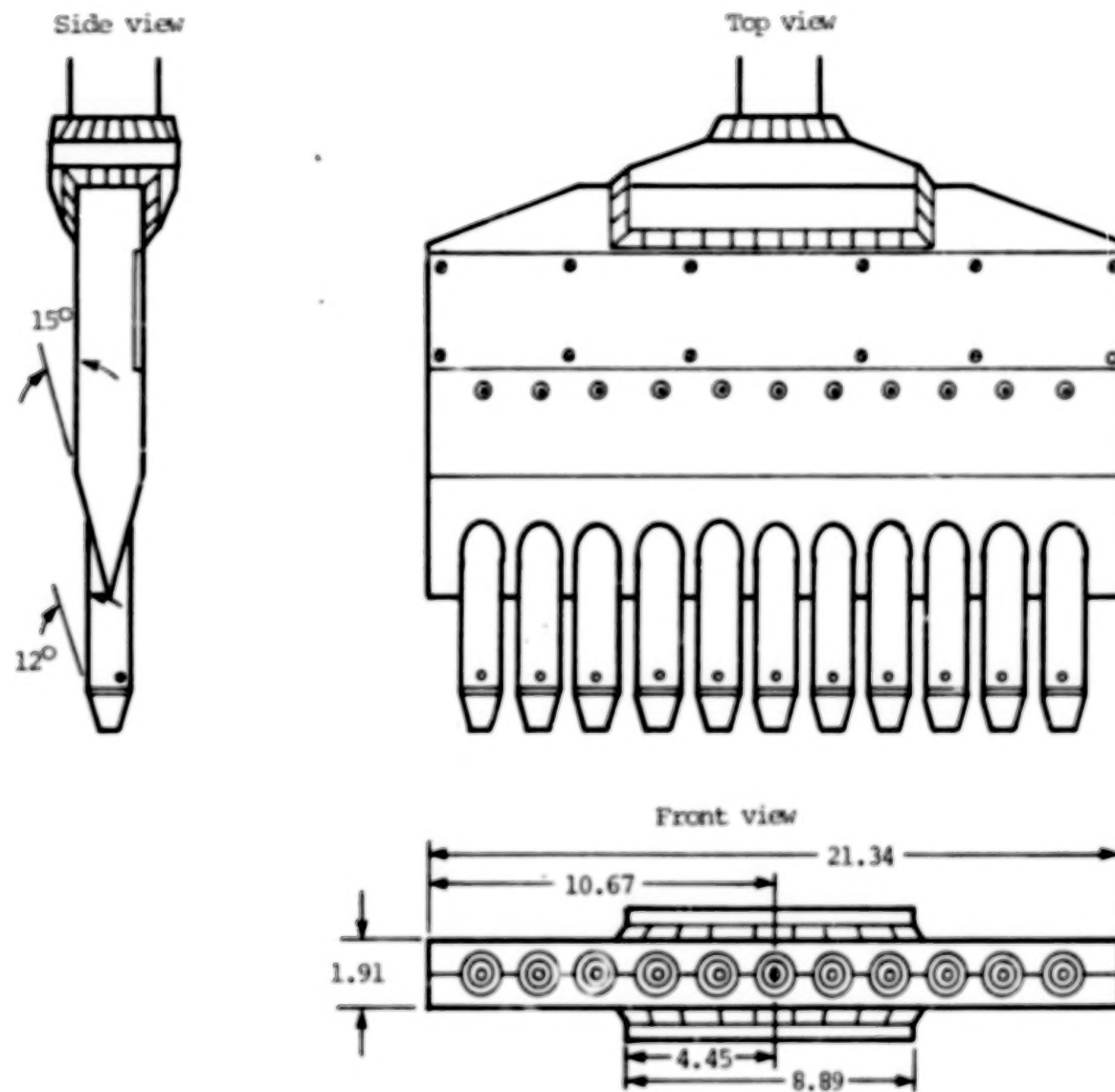


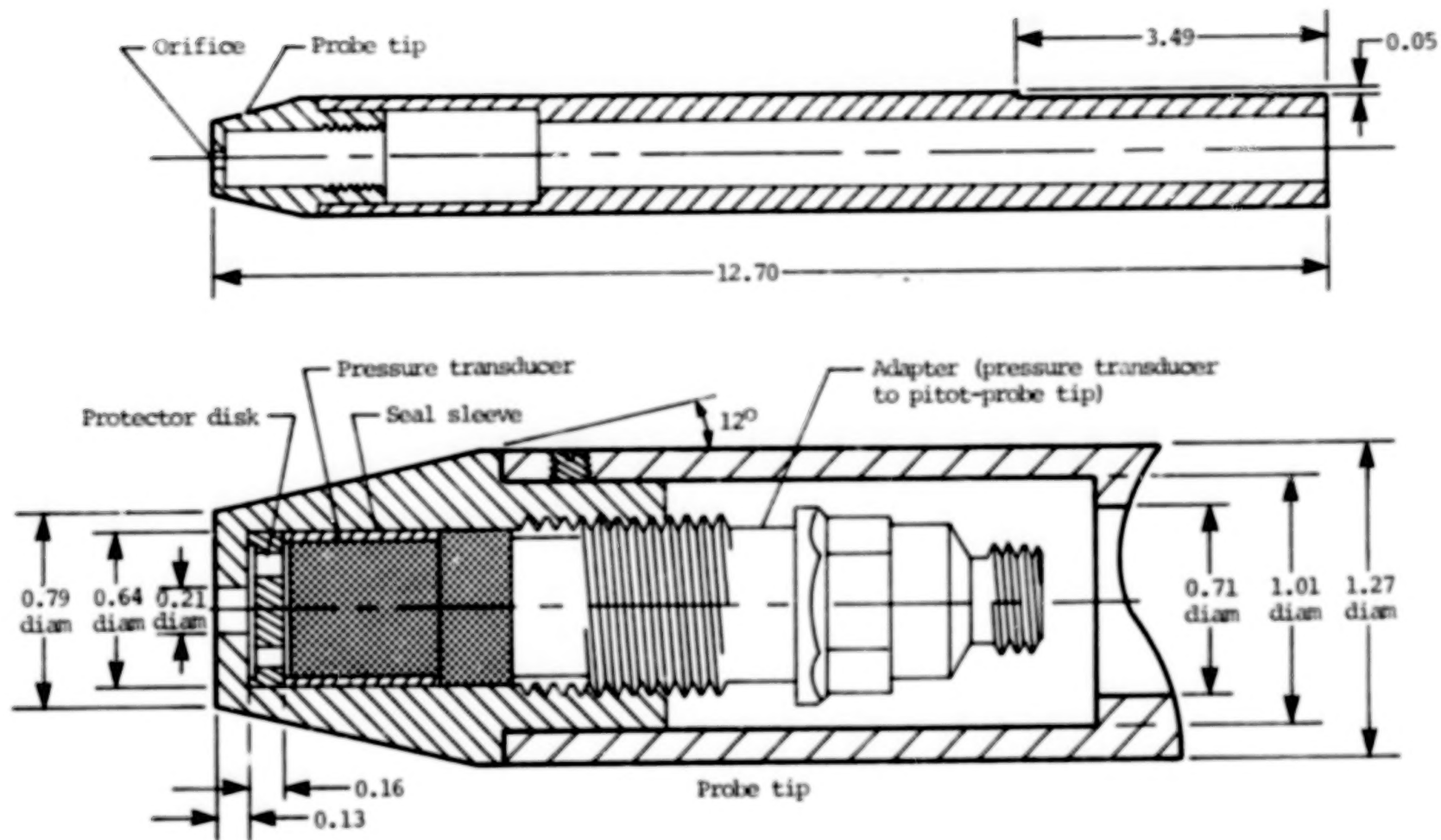
Figure 1.- Schematic diagram of expansion-tube flow sequence.



(a) Pitot-pressure survey rake.

Figure 2.- Pitot-pressure survey rake and probe. All dimensions are in centimeters.

Side view



(b) Pitot-pressure probe.

Figure 2.- Concluded.



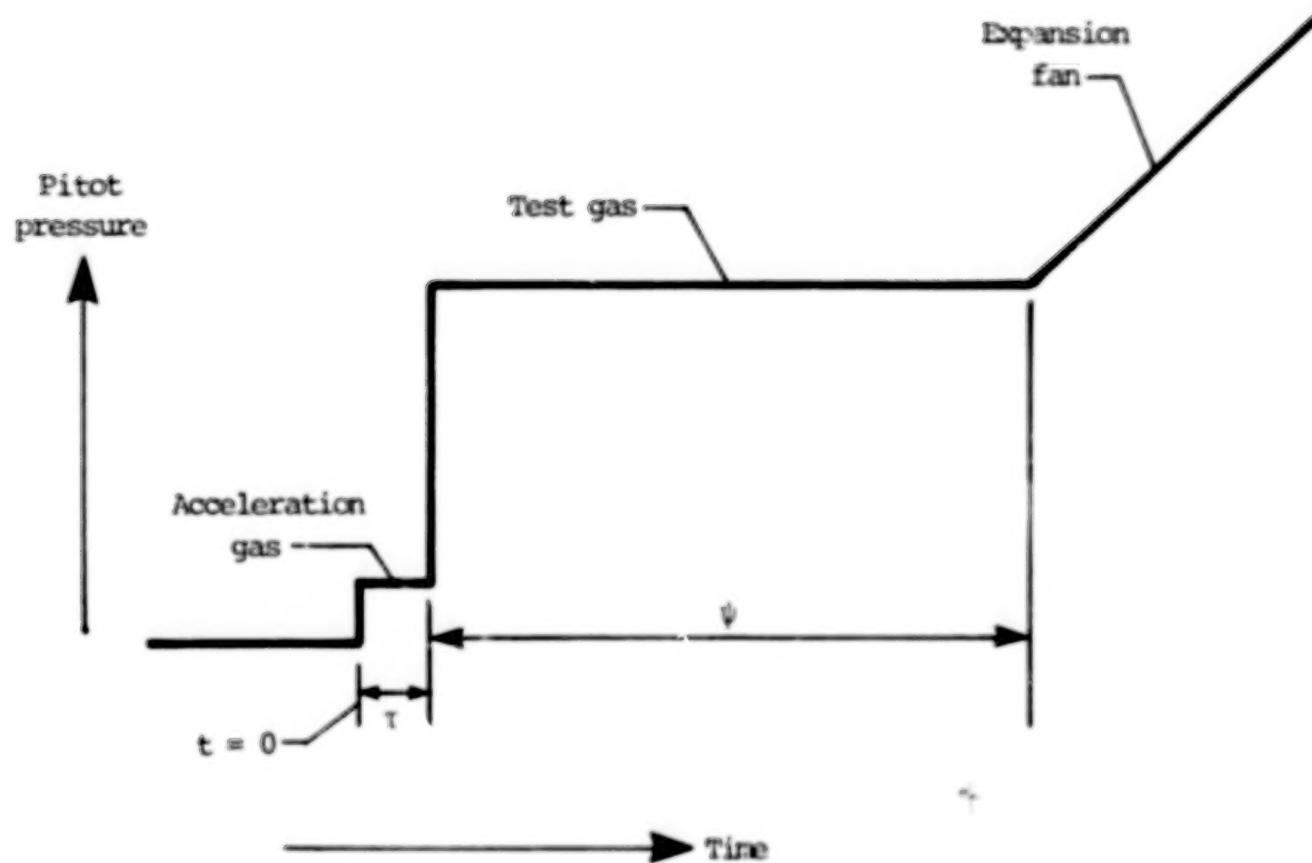
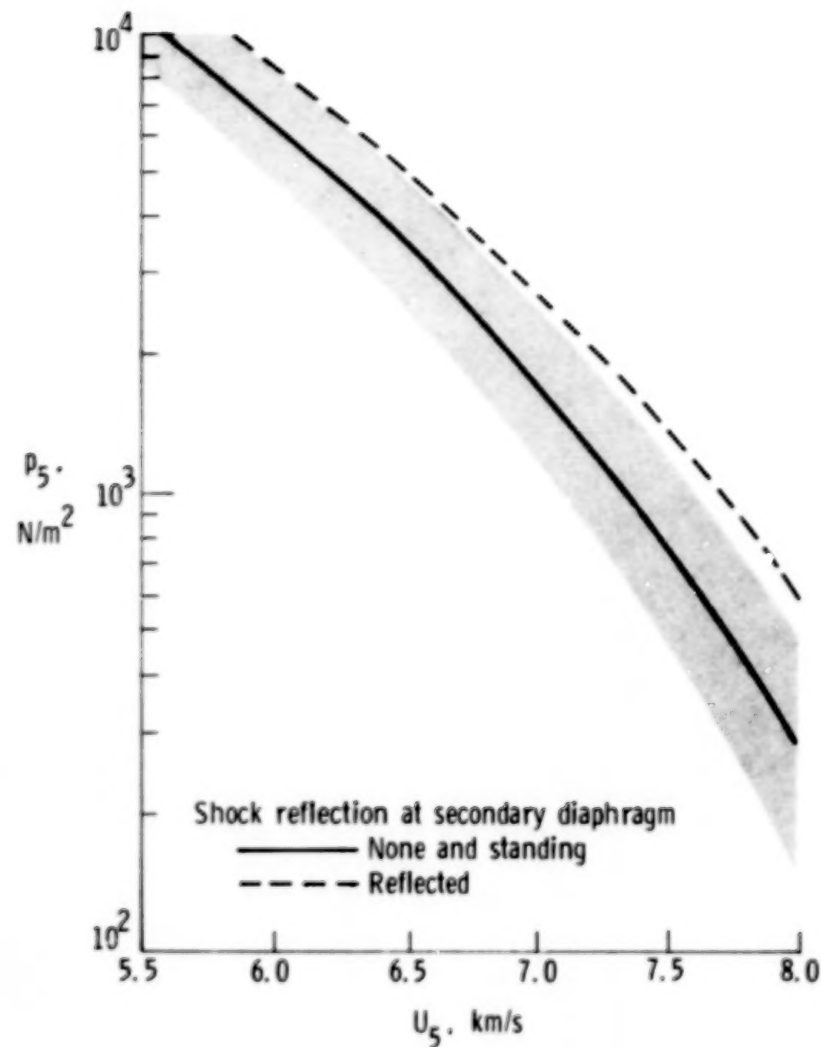
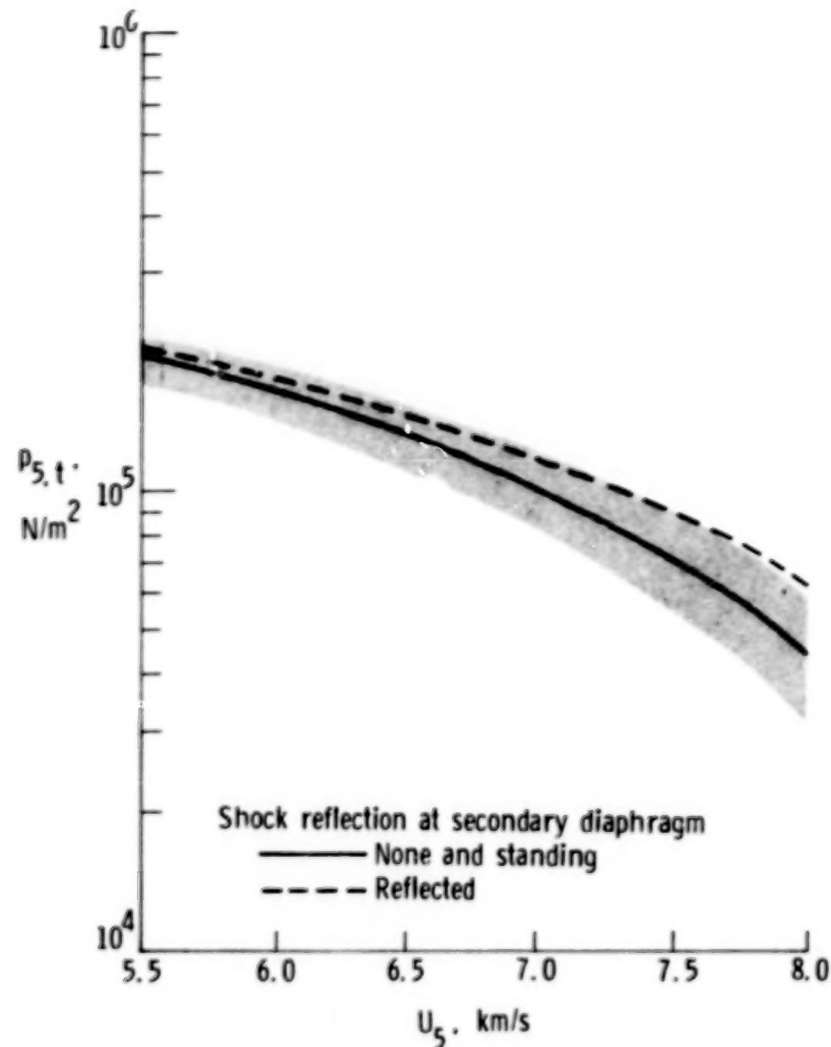


Figure 3.- Sketch of idealized pitot-pressure time history at tube exit.

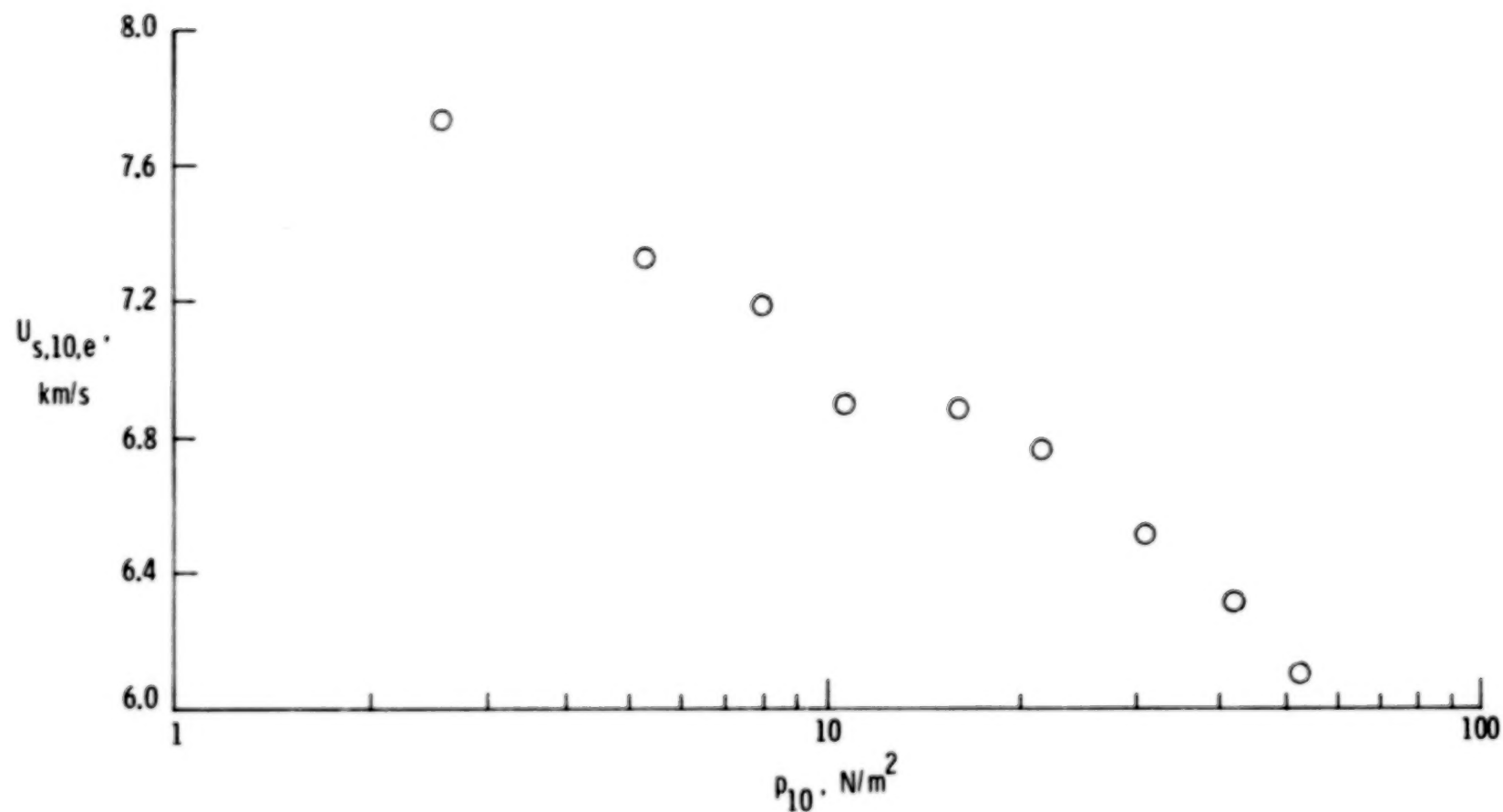


(a) Free-stream static pressure.



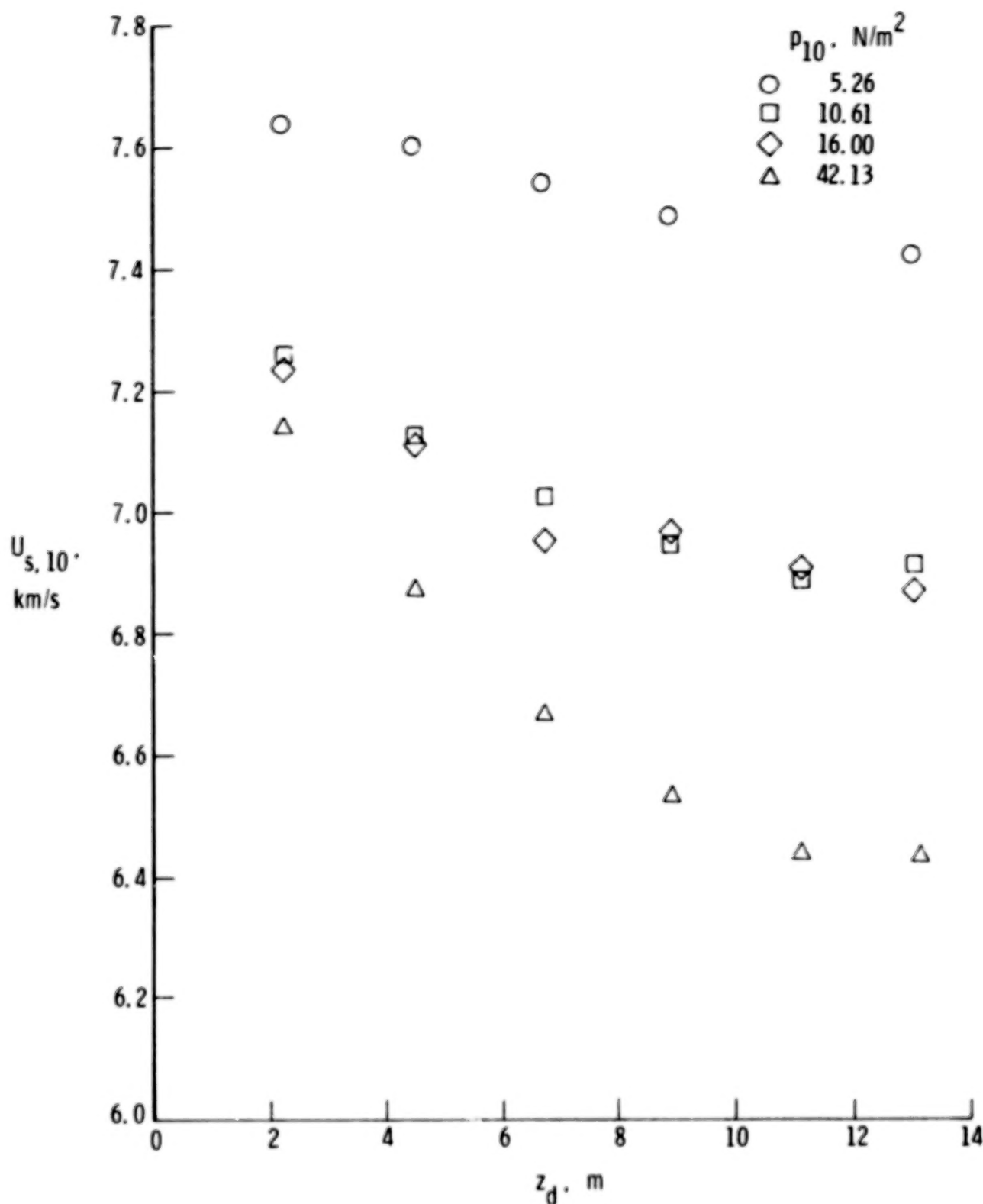
(b) Pitot pressure.

Figure 4.- Prediction (ref. 5) of pitot pressure and free-stream static pressure as a function of free-stream velocity.  $p_1 = 4.82 \text{ kN/m}^2$ ;  $p_{10} = 16.20 \text{ N/m}^2$ . Shaded region denotes uncertainty corresponding to  $\pm 3\%$  uncertainty in  $U_{S,1}$  for no shock reflection at secondary diaphragm.



(a) Incident shock velocity at tube exit.

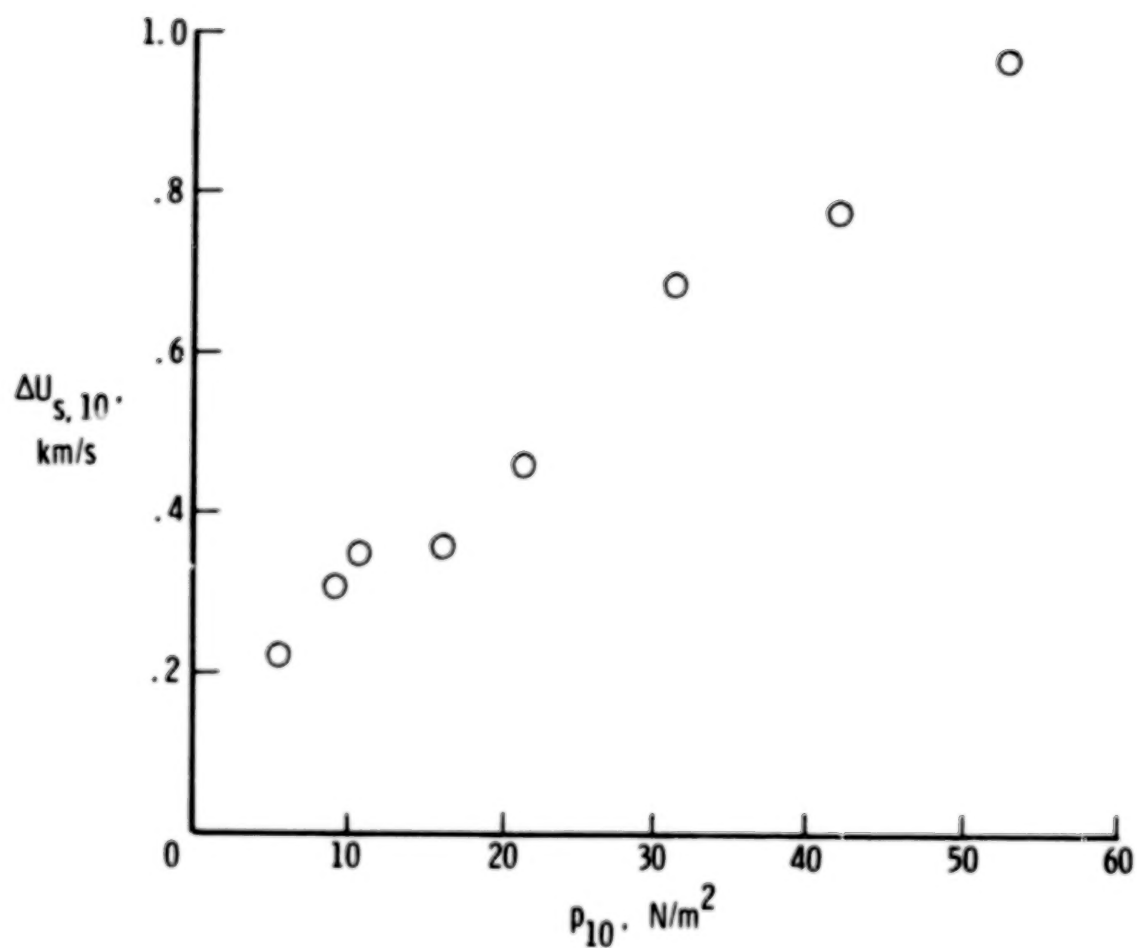
Figure 5.- Effect of quiescent acceleration-gas pressure on incident shock velocity.  $p_1 \approx 3.45 \text{ kN/m}^2$ .



(b) Incident shock velocity as a function of distance downstream of secondary diaphragm.

Figure 5.- Continued.





(c) Total attenuation of incident shock velocity along acceleration section.

$$\Delta U_{s,10} = U_{s,10,max} - U_{s,10,e}$$

Figure 5.- Concluded.

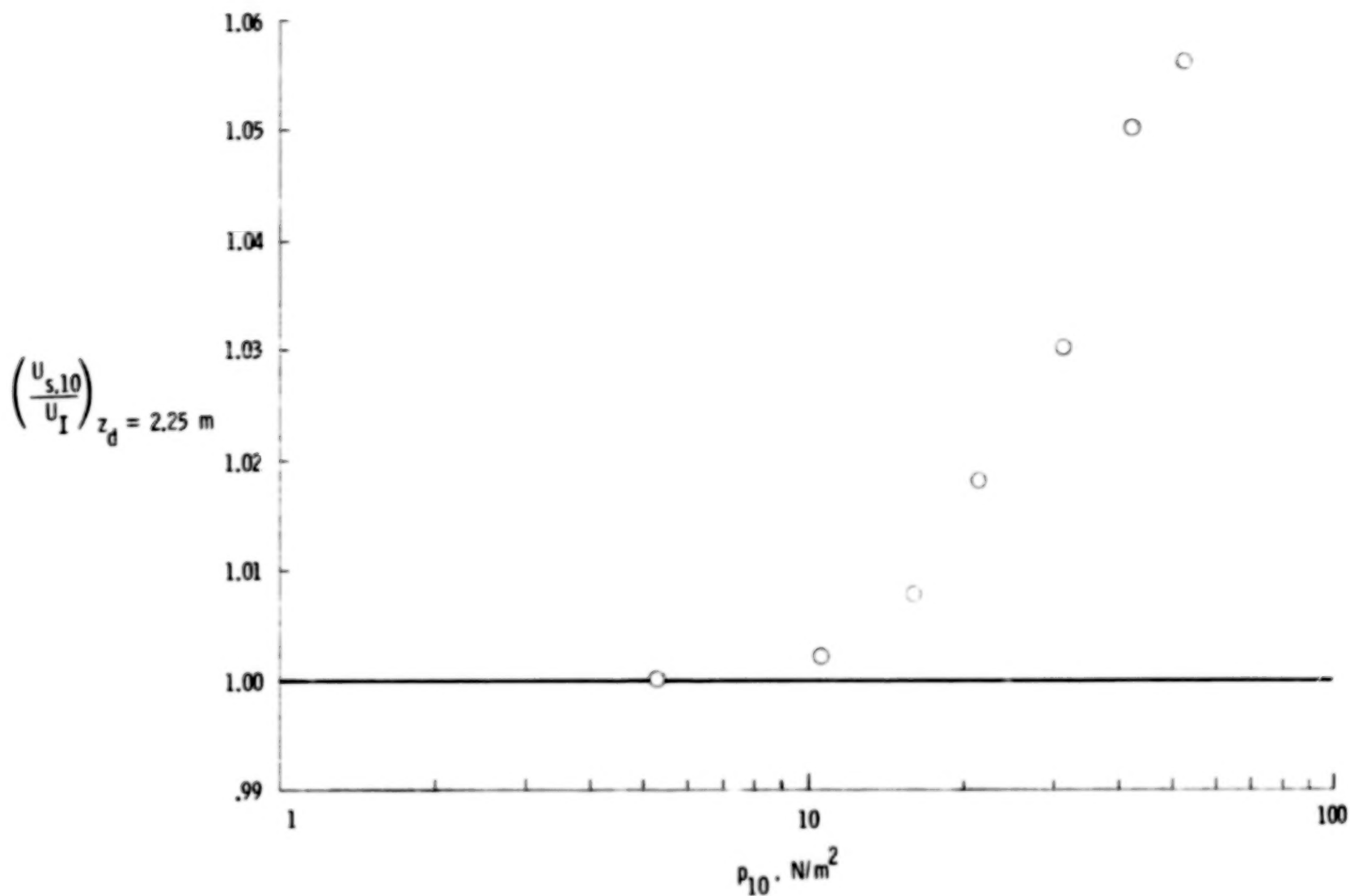


Figure 6.- Predicted (ref. 15) ratio of incident shock velocity to interface velocity at 2.25 m downstream of secondary diaphragm.  $p_1 \sim 3.45 \text{ kN/m}^2$ .

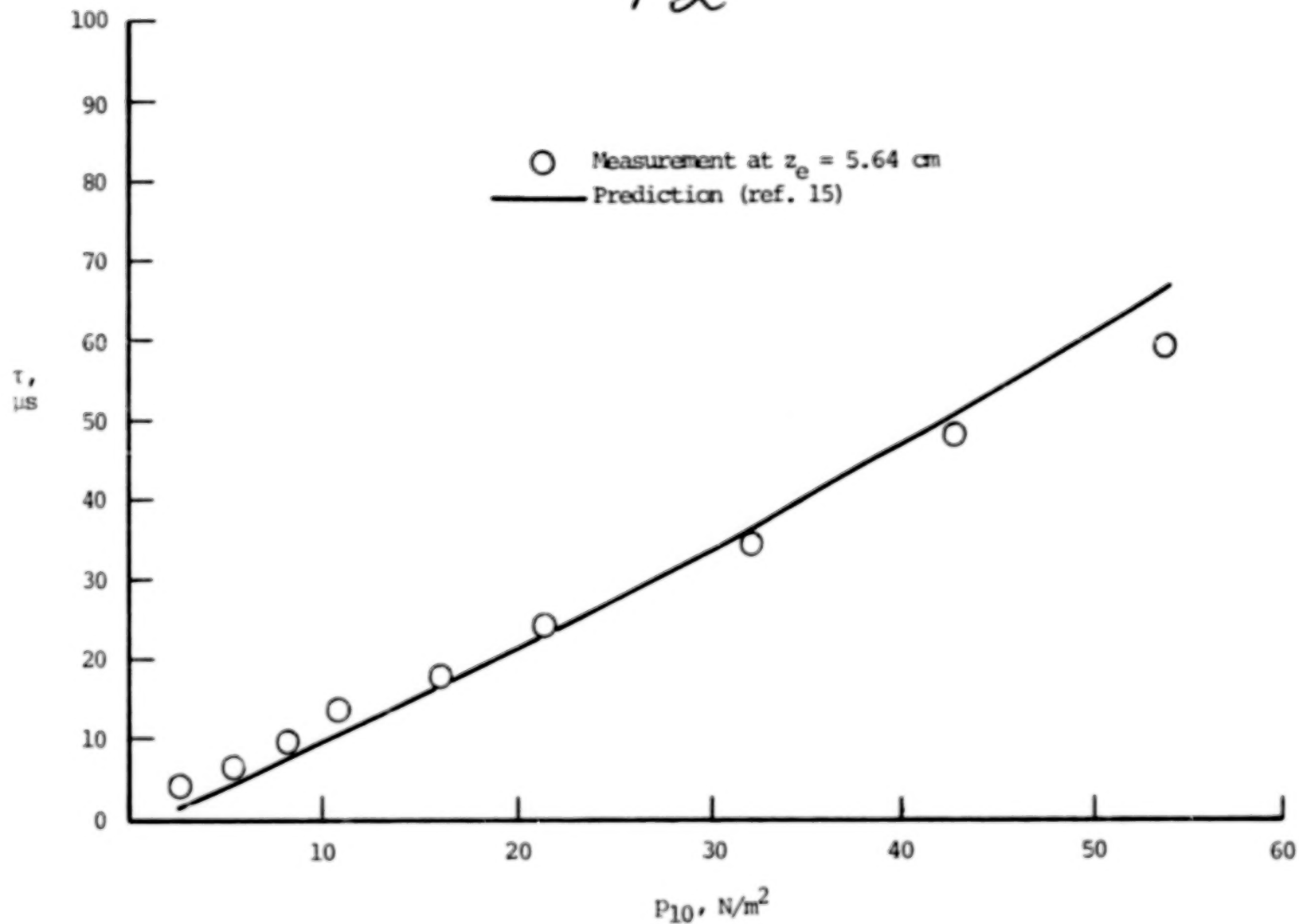


Figure 7.- Time interval between incident shock and acceleration-gas/test-gas interface as a function of quiescent acceleration-gas pressure.  $p_1 = 3.45 \text{ kN/m}^2$ .

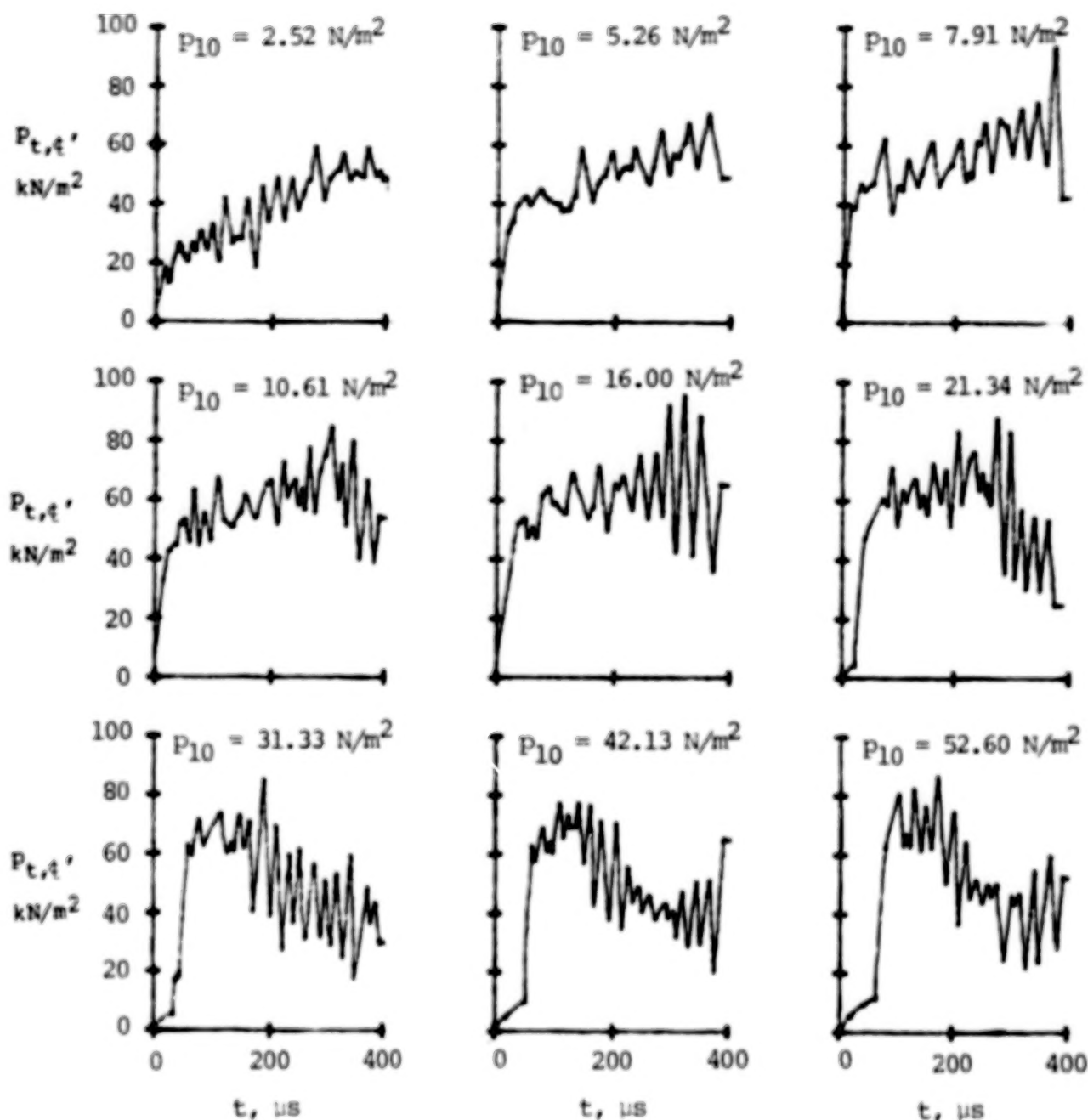
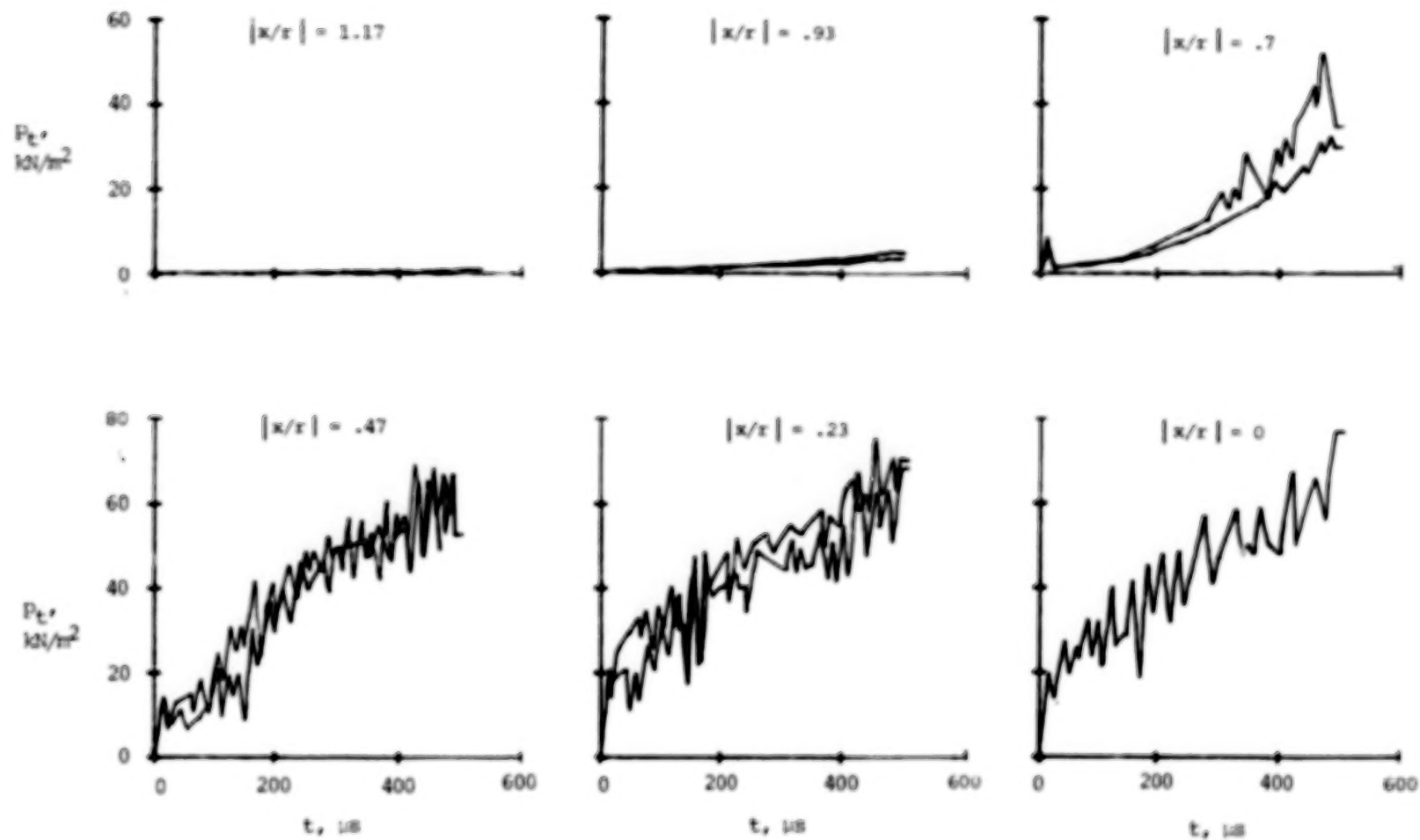


Figure 8.- Effect of quiescent acceleration-gas pressure on centerline pitot-pressure time history.  $z_e = 5.64 \text{ cm}$ ;  $p_1 = 3.45 \text{ kN/m}^2$ .

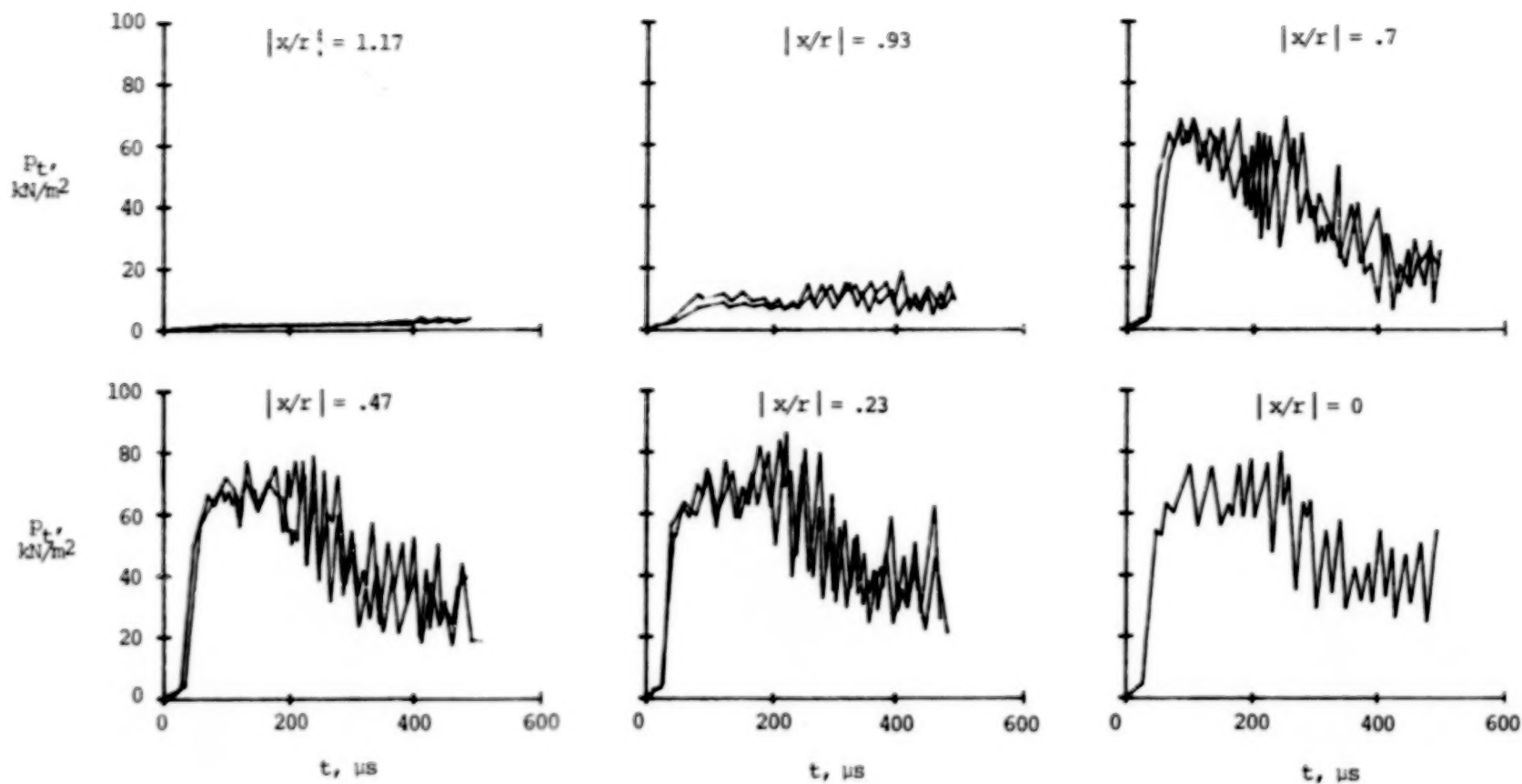


44.



(a)  $P_{10} = 2.52 \text{ N/m}^2$ .

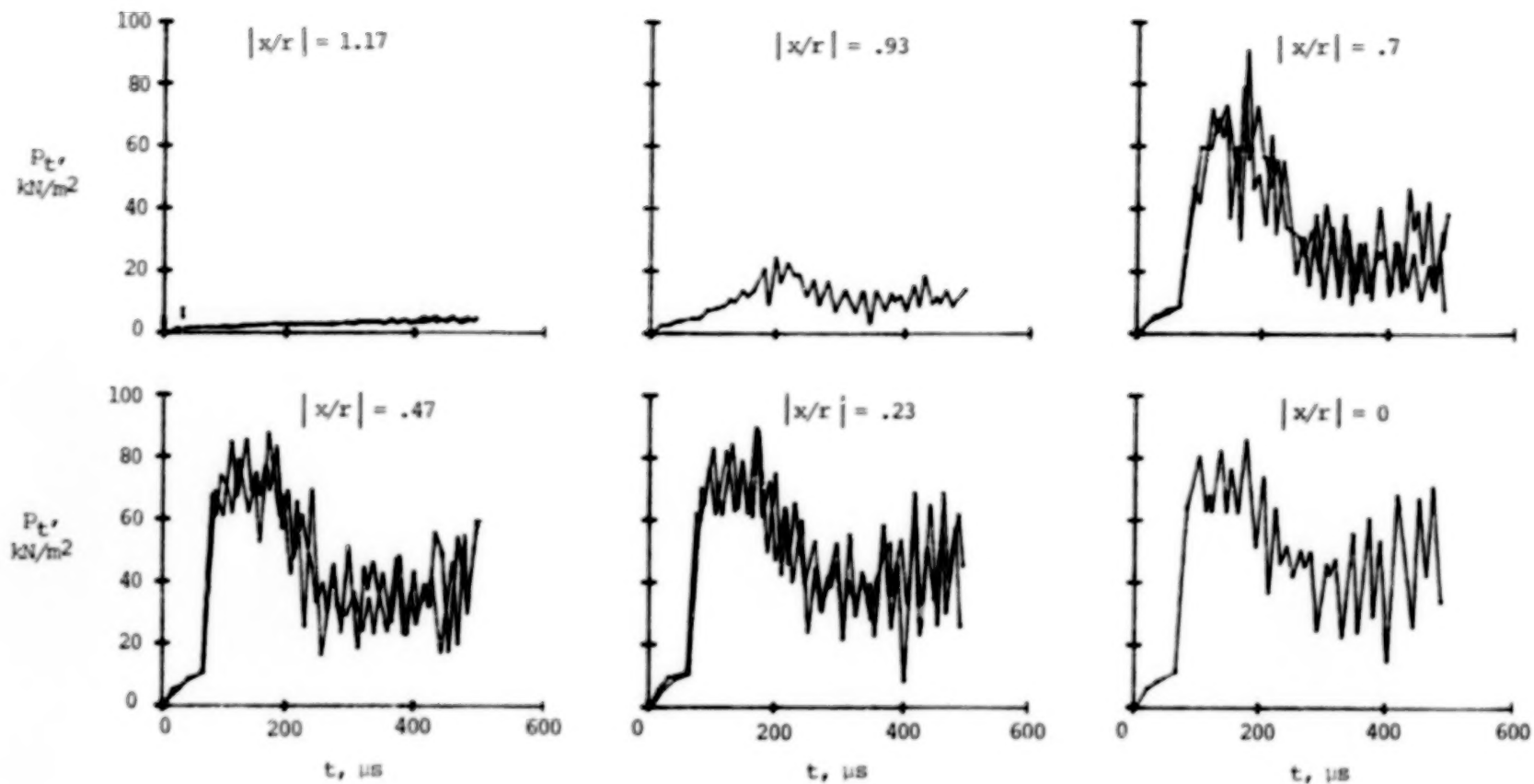
Figure 9.- Effect of distance from tube centerline on pitot-pressure time history.  
 $z_e = 5.64 \text{ cm}$ ;  $p_1 = 3.45 \text{ kN/m}^2$ .



(b)  $p_{10} = 26.45 \text{ N/m}^2$ .

Figure 9.- Continued.

46



(c)  $P_{10} = 52.60 \text{ N/m}^2$ .

Figure 9.- Concluded.

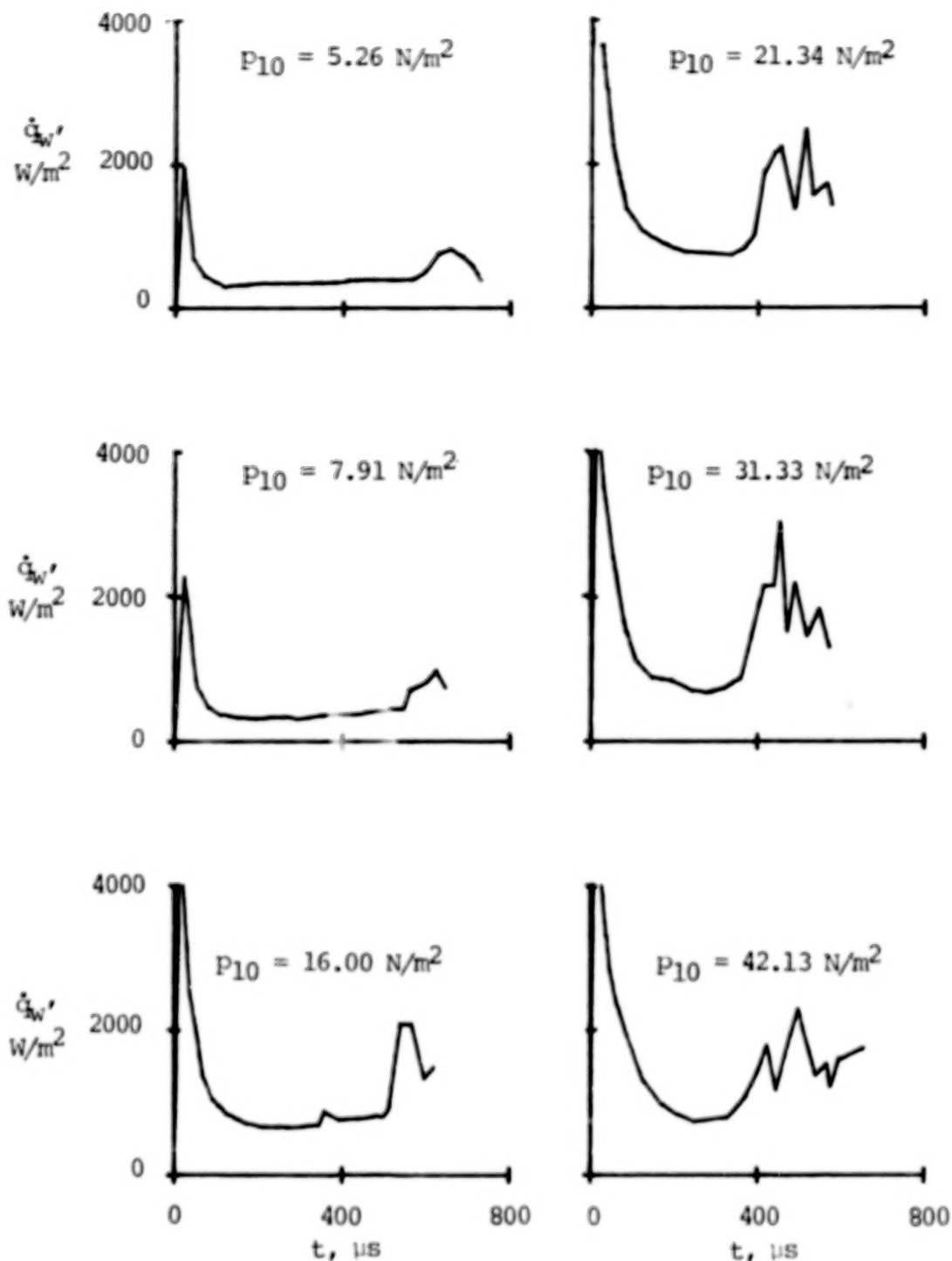


Figure 10.- Effect of quiescent acceleration-gas pressure on time history of tube-wall heat transfer: 12.23 m downstream of secondary diaphragm.  $p_1 = 3.45 \text{ kN/m}^2$ . ( $\dot{q}_w$  was obtained to illustrate trends only and should not be used quantitatively.)

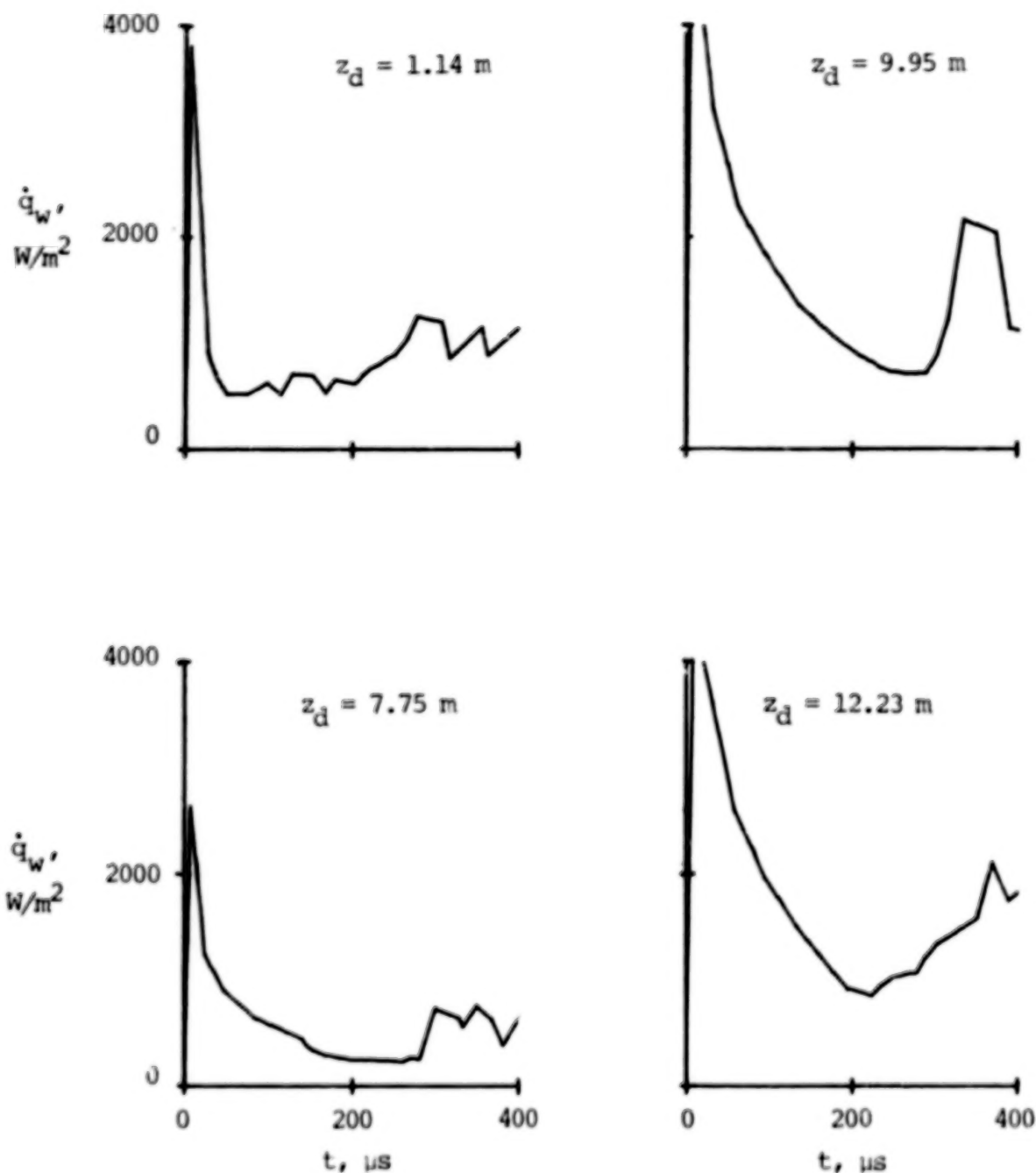


Figure 11.- Time history of tube-wall heat transfer at various distances downstream of secondary diaphragm.  $p_1 \approx 3.45 \text{ kN/m}^2$ ;  $p_{10} = 52.60 \text{ N/m}^2$ . ( $\dot{q}_w$  was obtained to illustrate trends only and should not be used quantitatively.)



-----  $P_{20}$  predicted from conventional shock-tube theory  
corrected to the value at the interface (ref. 19)

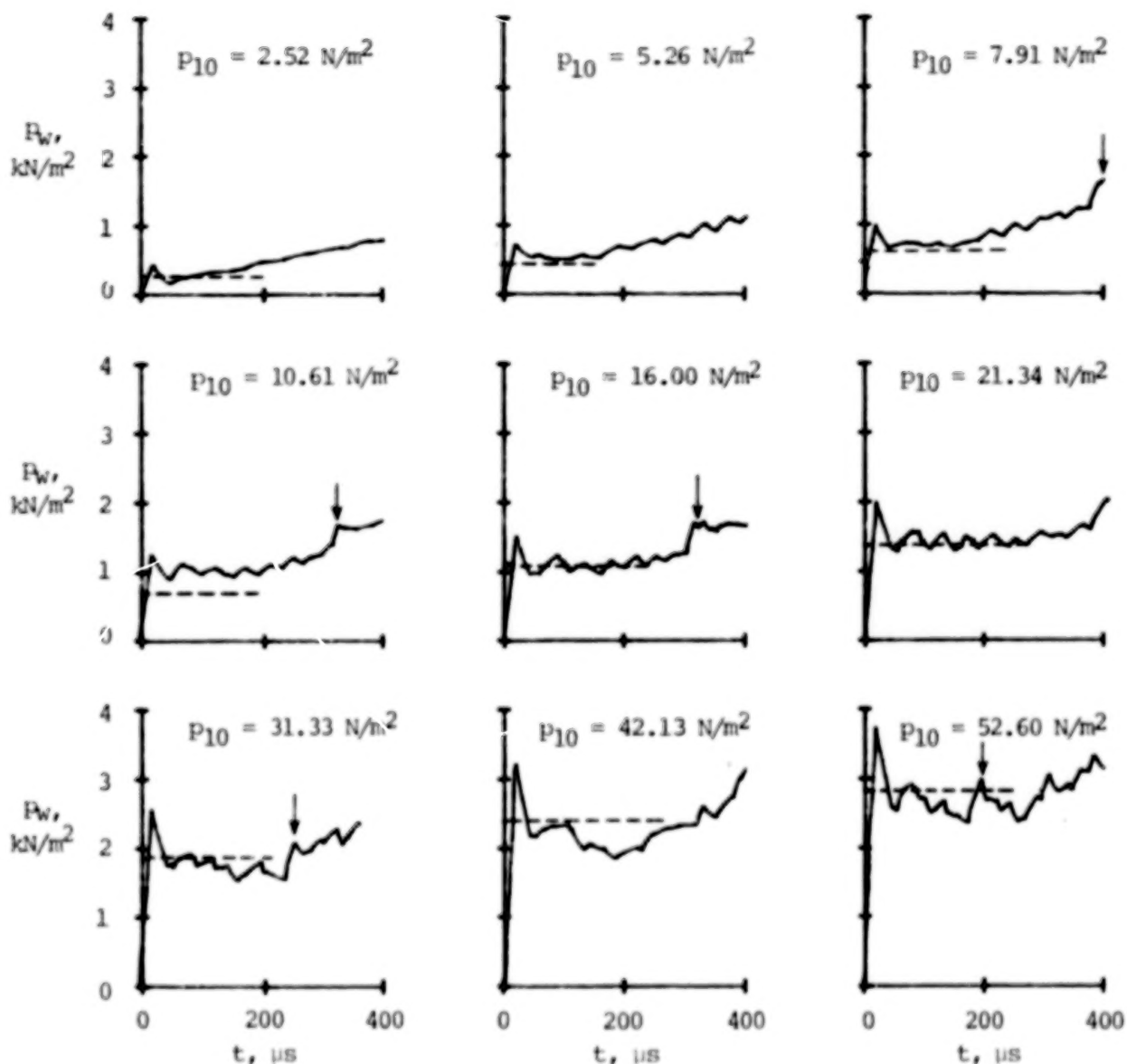


Figure 12.- Effect of quiescent acceleration-gas pressure on tube-wall-pressure time history 2.54 cm upstream of tube exit.  $p_1 \approx 3.45 \text{ kN/m}^2$ . Arrows denote the apparent second sharp pressure increase.

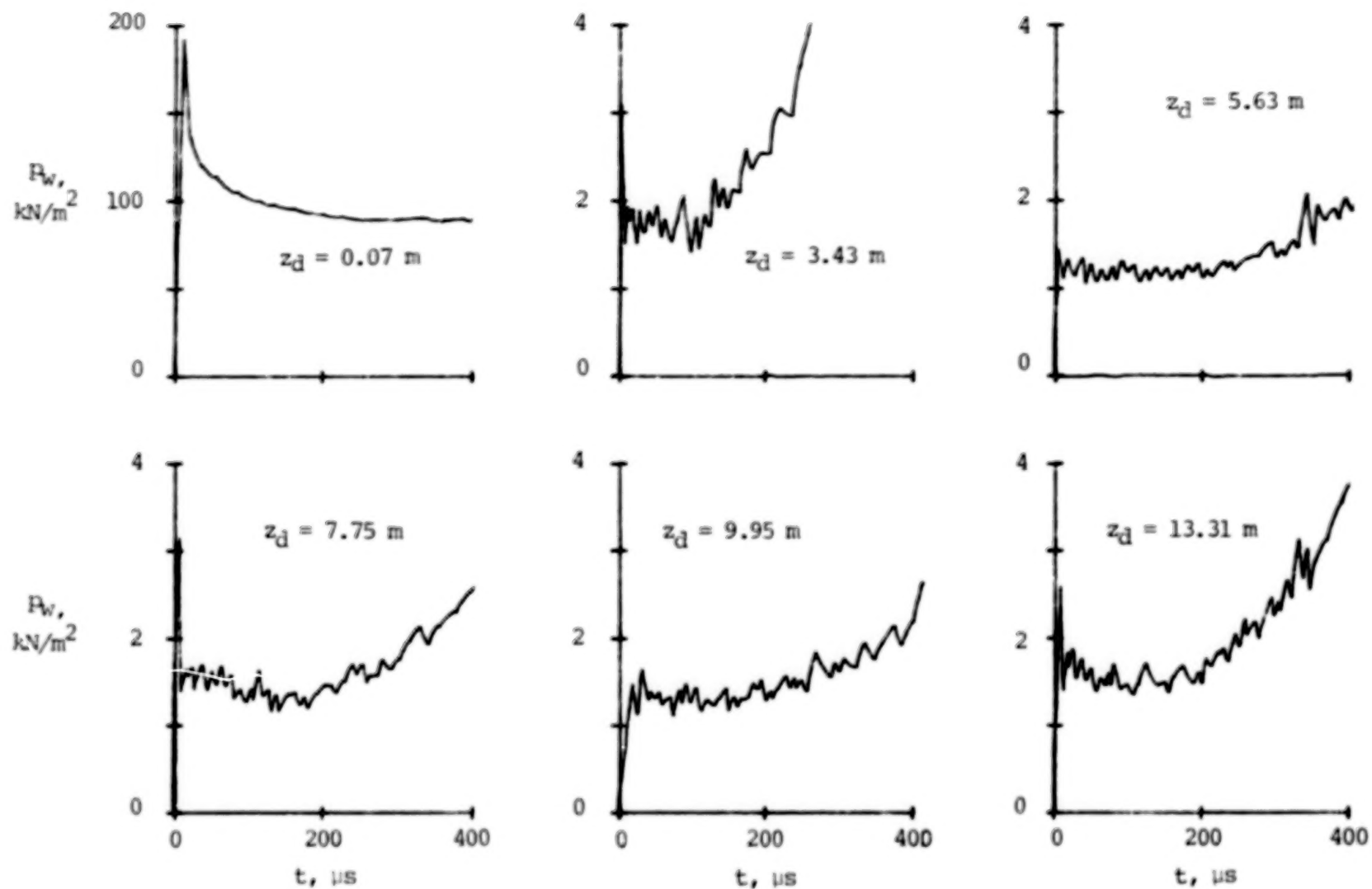


Figure 13.- Measured tube-wall-pressure time history at various distances downstream of secondary diaphragm.  $p_1 \approx 3.45 \text{ kN/m}^2$ ;  $p_{10} = 16.00 \text{ N/m}^2$ . Note scale changes.

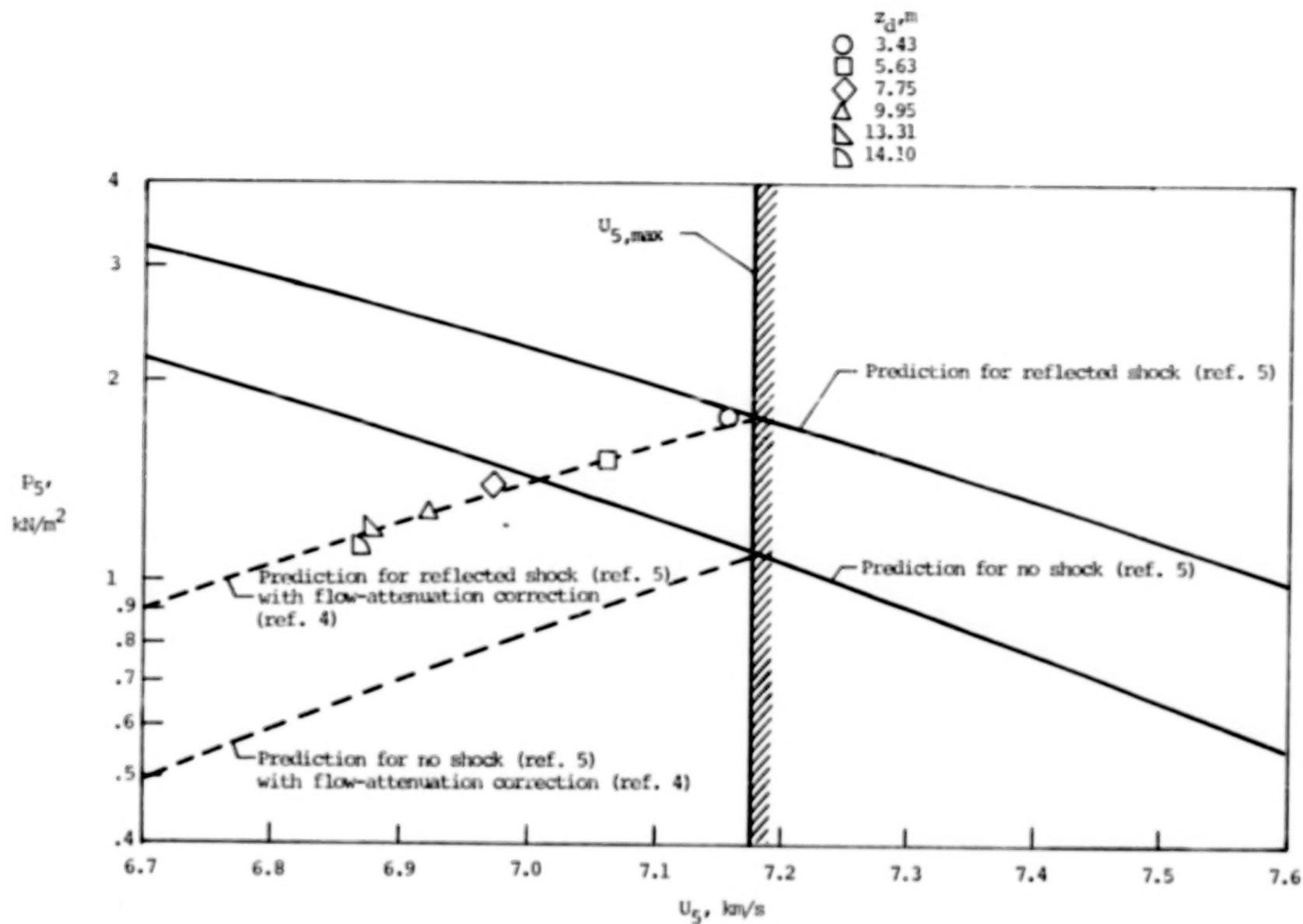


Figure 14.- Comparison of measured tube-wall pressure at various distances downstream of secondary diaphragm with predictions.  $p_1 = 3.45 \text{ kN/m}^2$ ;  $p_{10} = 16.00 \text{ N/m}^2$ .

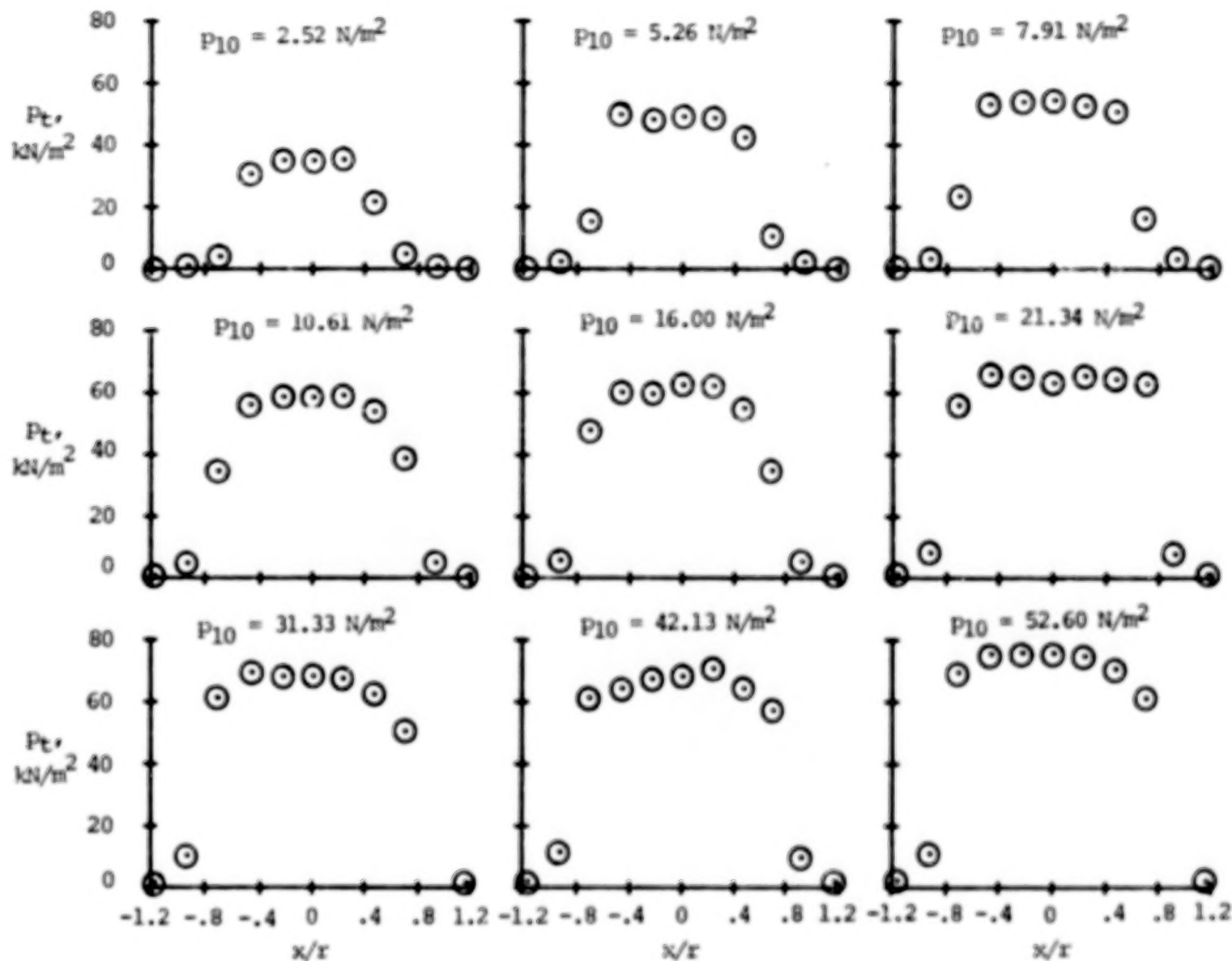
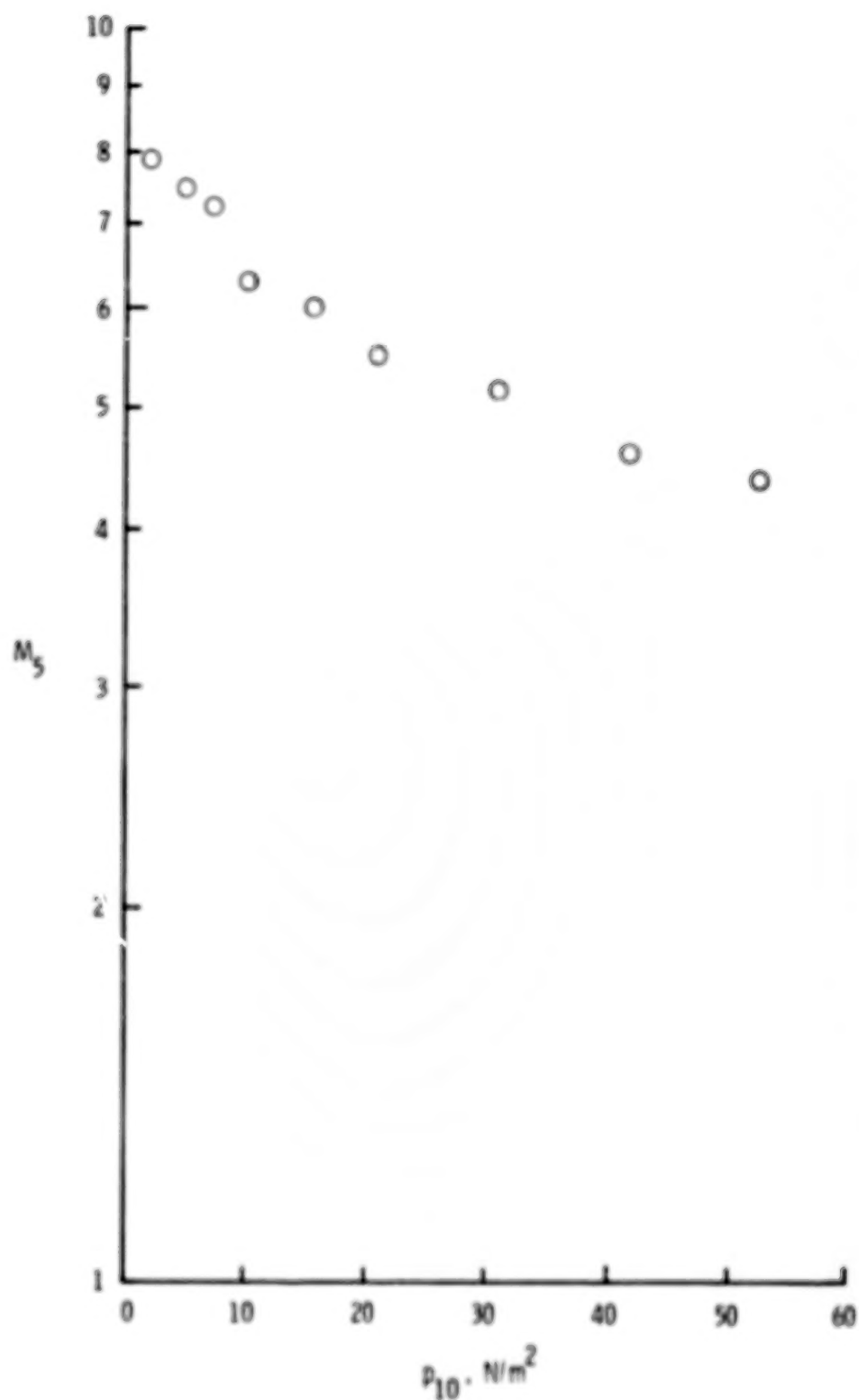


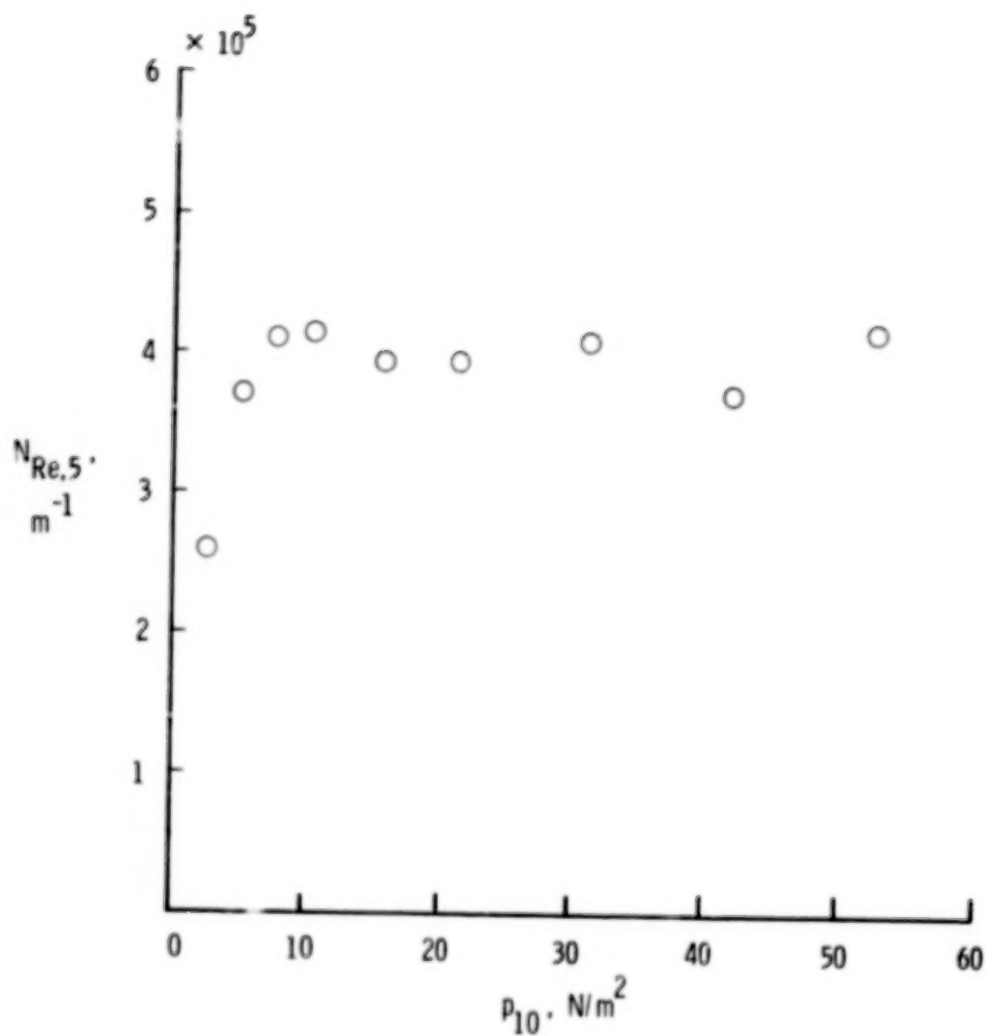
Figure 15.- Effect of quiescent acceleration-gas pressure on pitot-pressure profile.  
 $z_e = 5.64 \text{ cm}$ ;  $t = 150 \text{ } \mu\text{s}$ ;  $p_1 = 3.45 \text{ kN/m}^2$ .



(a) Free-stream Mach number.

Figure 16.- Effect of quiescent acceleration-gas pressure on free-stream Mach number and Reynolds number.





(b) Unit free-stream Reynolds number.

Figure 16.- Concluded.

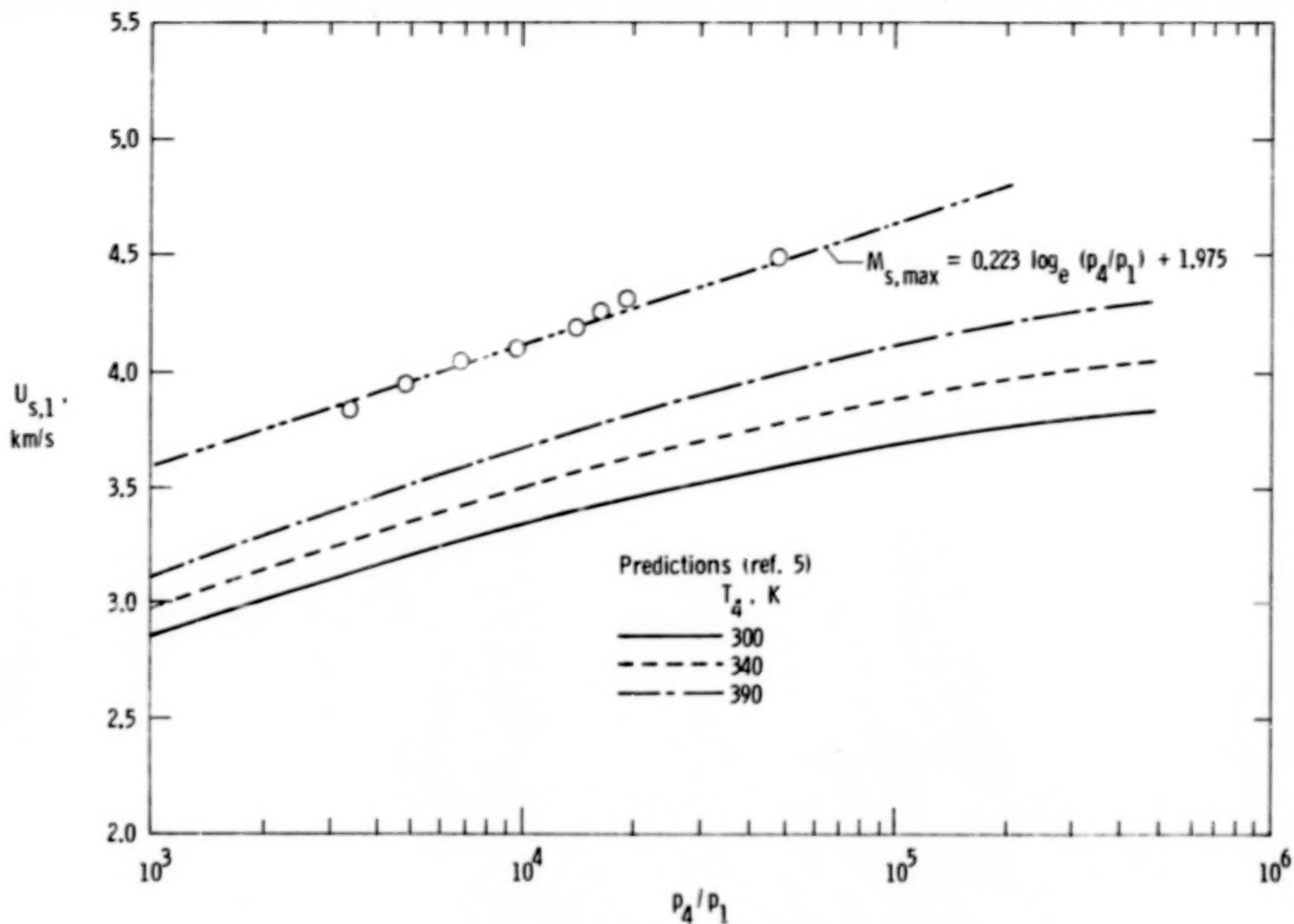


Figure 17.- Measured maximum incident shock velocity into test gas and prediction from conventional shock-tube theory.

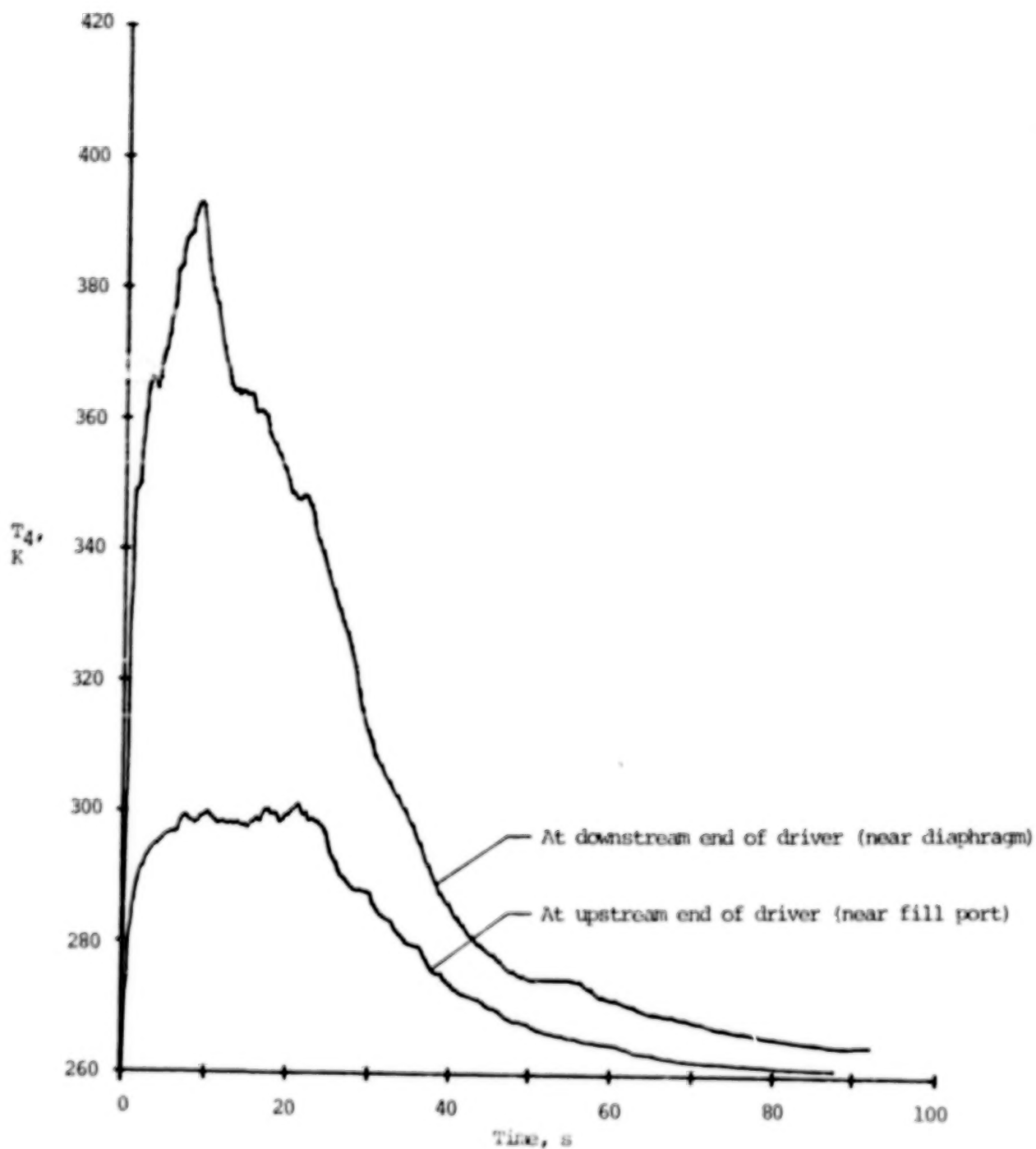


Figure 18.- Time histories of helium driver temperature during pressurization.

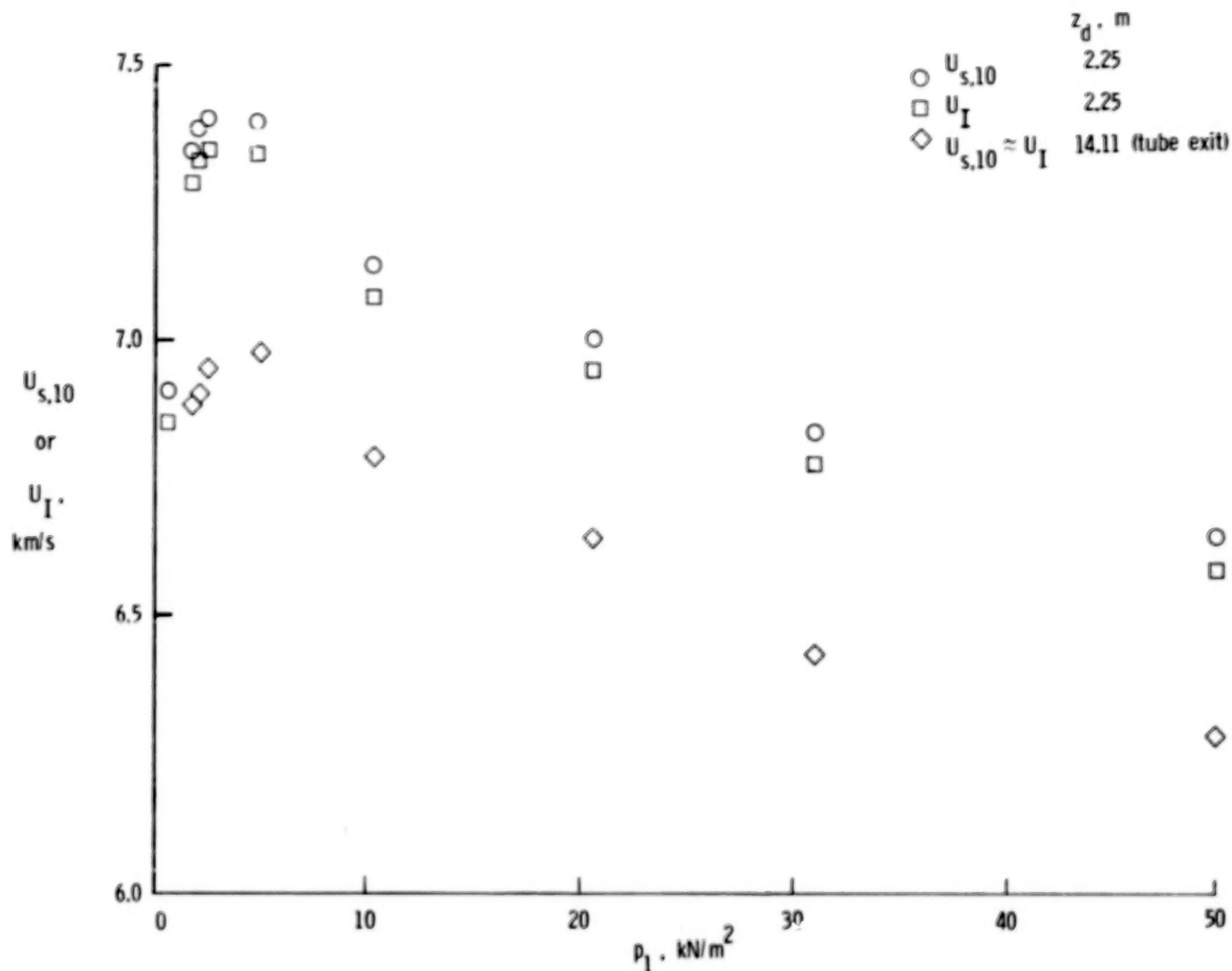


Figure 19.- Effect of quiescent test-gas pressure on measured incident shock velocity and inferred acceleration-gas/test-gas interface velocity at two distances downstream of secondary diaphragm.  $p_{10} \approx 16.00$  N/m<sup>2</sup>.

Prediction (conventional  
shock-tube theory)

-----  $P_2$

-----  $P_{2r}$  (assuming totally  
reflected shock)

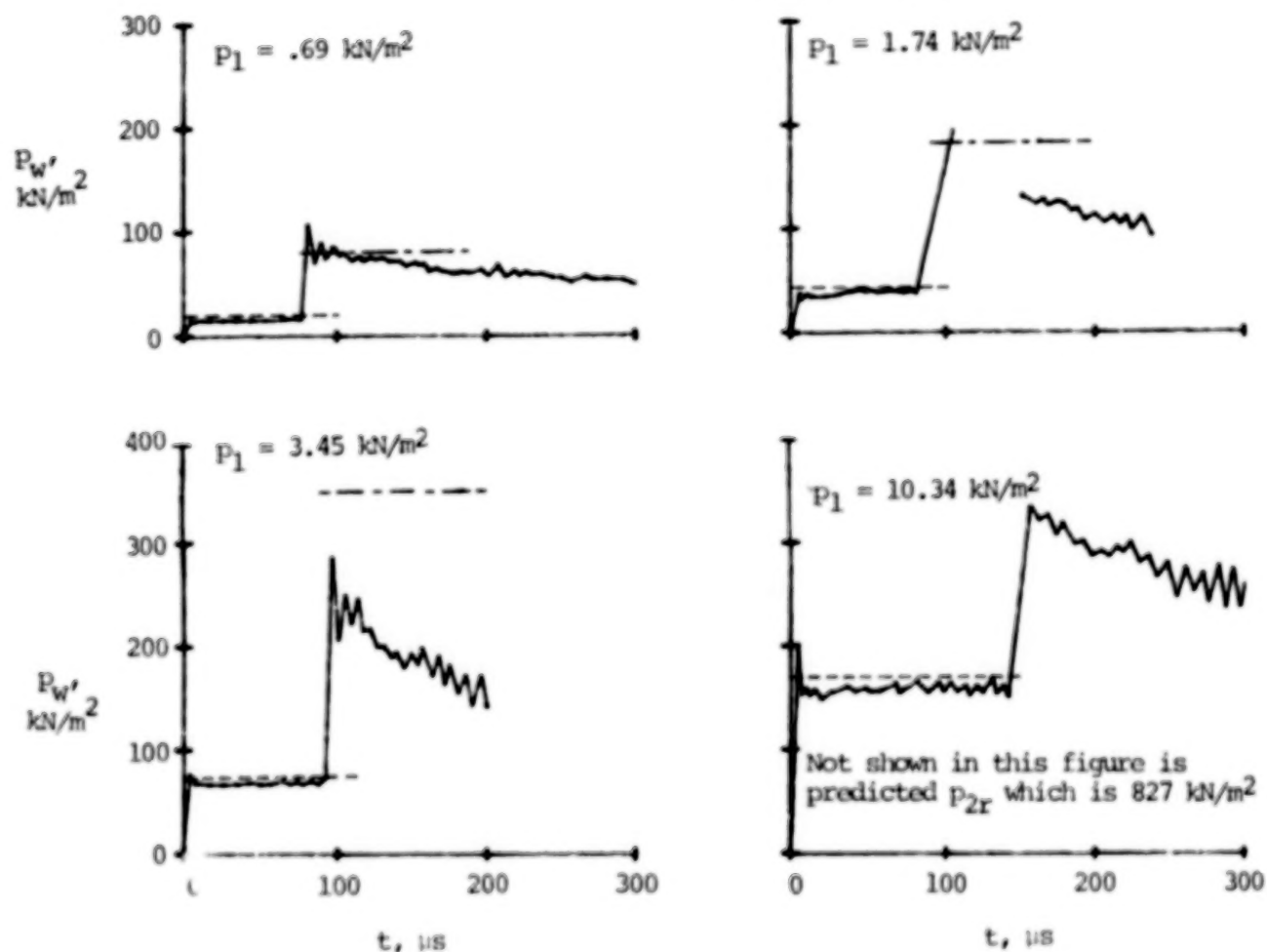
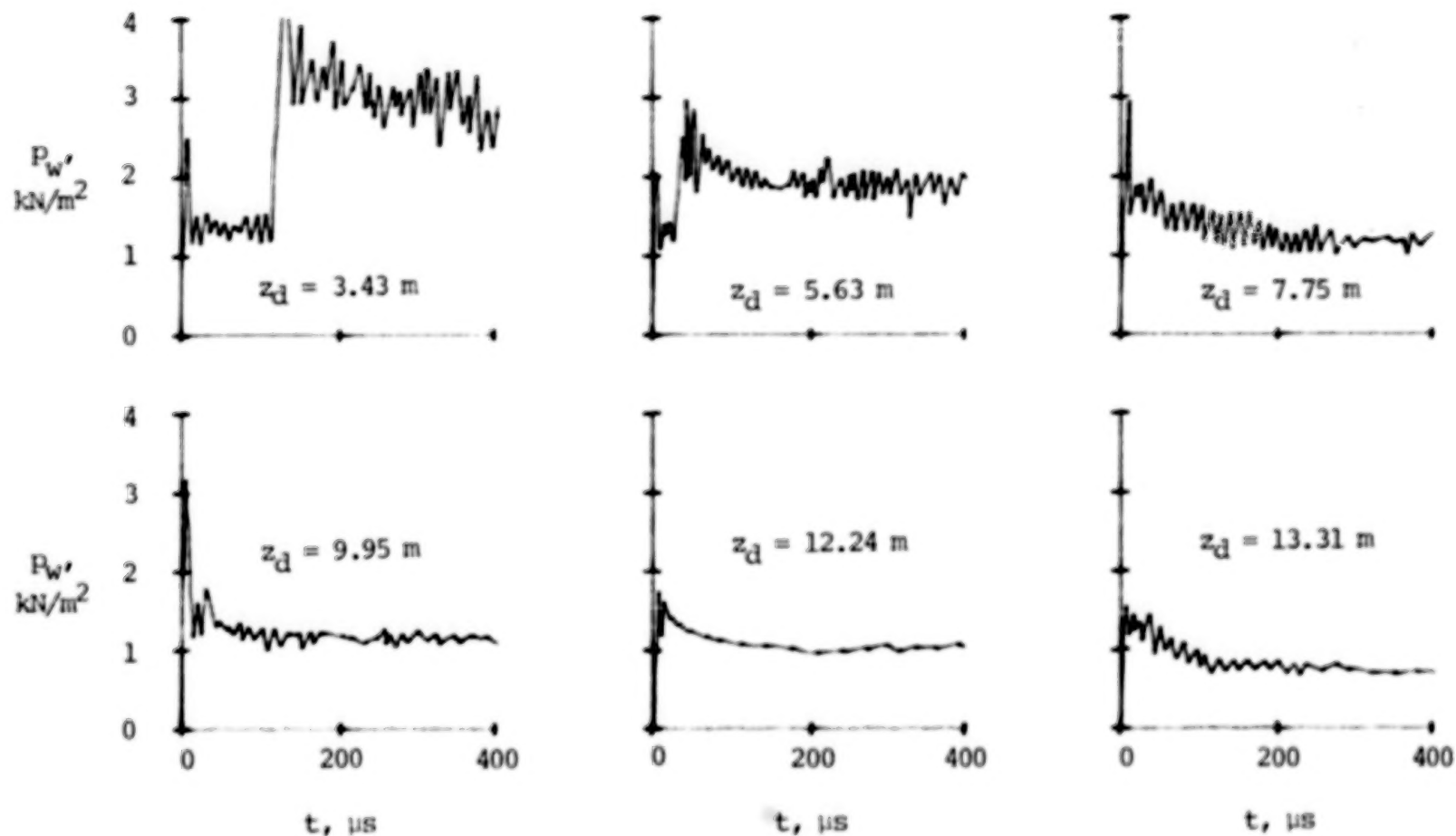


Figure 20.- Effect of quiescent test-gas pressure on tube-wall-pressure time history measured 11.04 cm upstream of secondary diaphragm.  $P_{10} \approx 16.00 \text{ N/m}^2$ ;  $W = 6.35 \mu\text{m}$ .

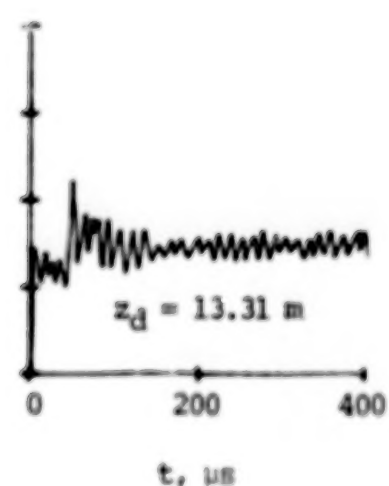
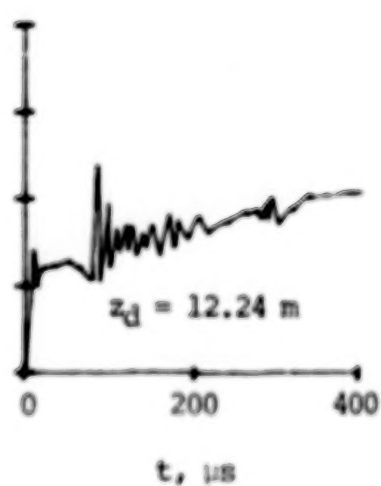
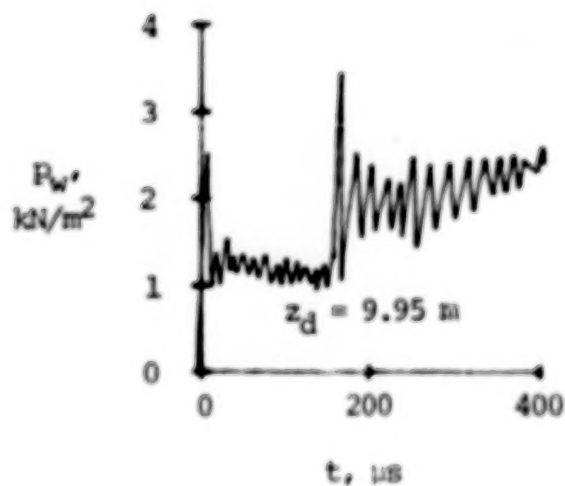
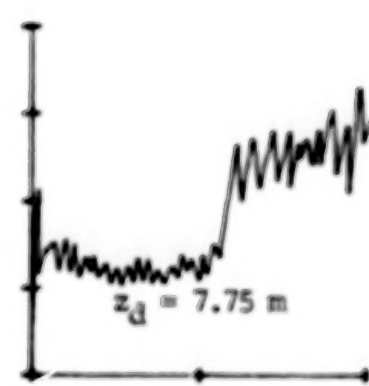
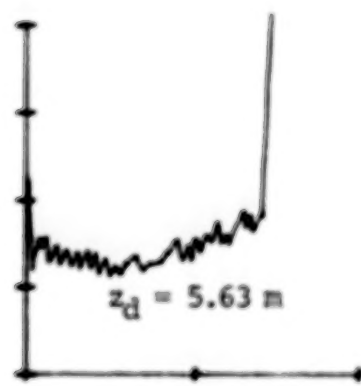
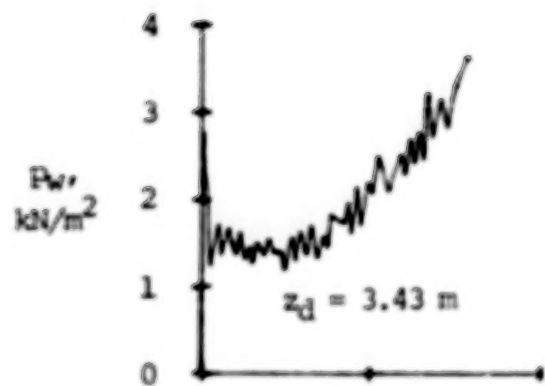




(a)  $p_1 = 0.69 \text{ kN/m}^2$ .

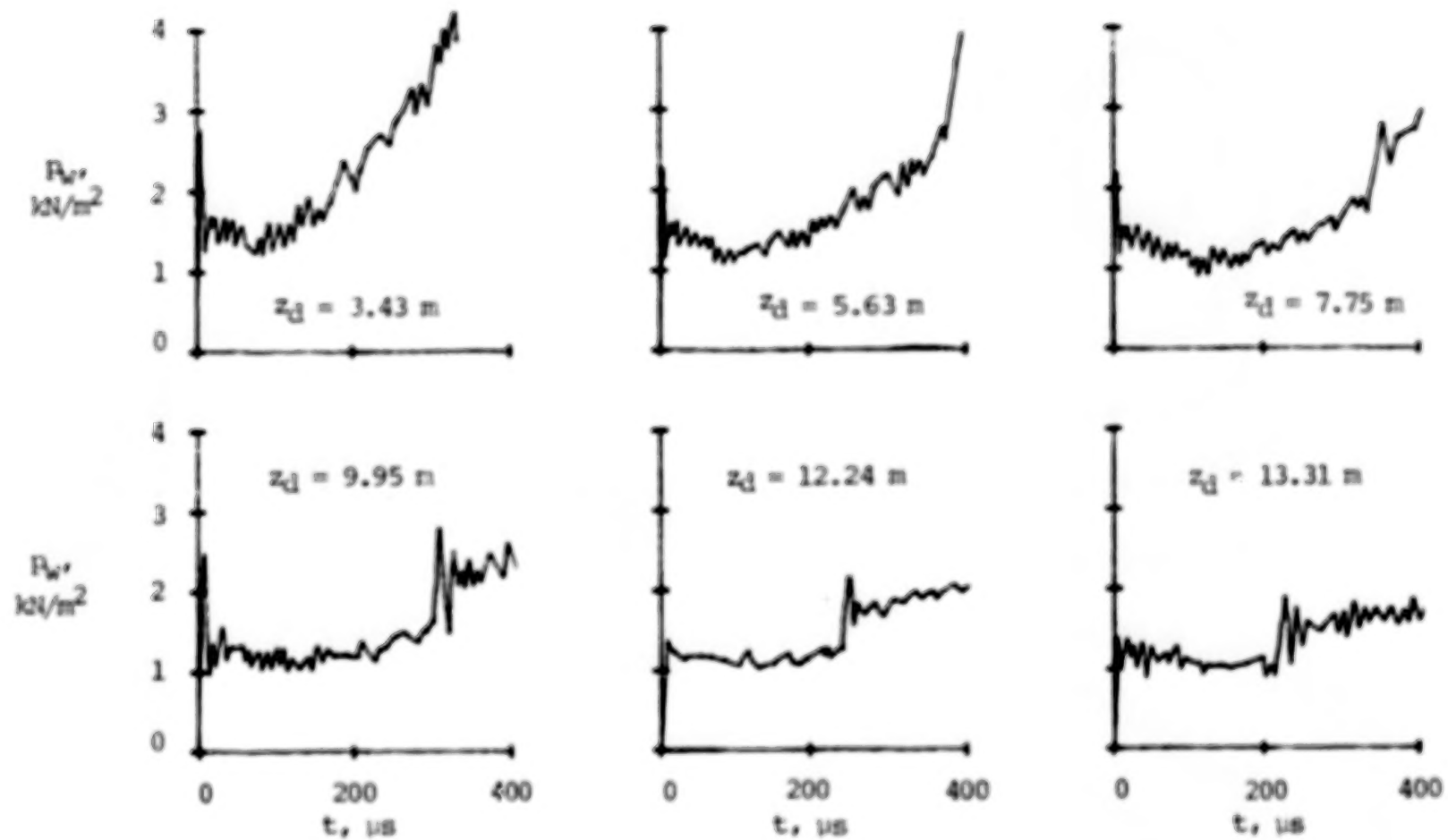
Figure 21.- Measured tube-wall-pressure time history at various distances downstream of secondary diaphragm for various quiescent test-gas pressures.  $p_{10} = 16.00 \text{ N/m}^2$ ;  $W = 6.35 \mu\text{m}$ .

60



(b)  $p_1 = 1.74$  kN/m<sup>2</sup>.

Figure 21.- Continued.



(c)  $p_1 = 2.41 \text{ kN/m}^2$ .

Figure 21.- Concluded.

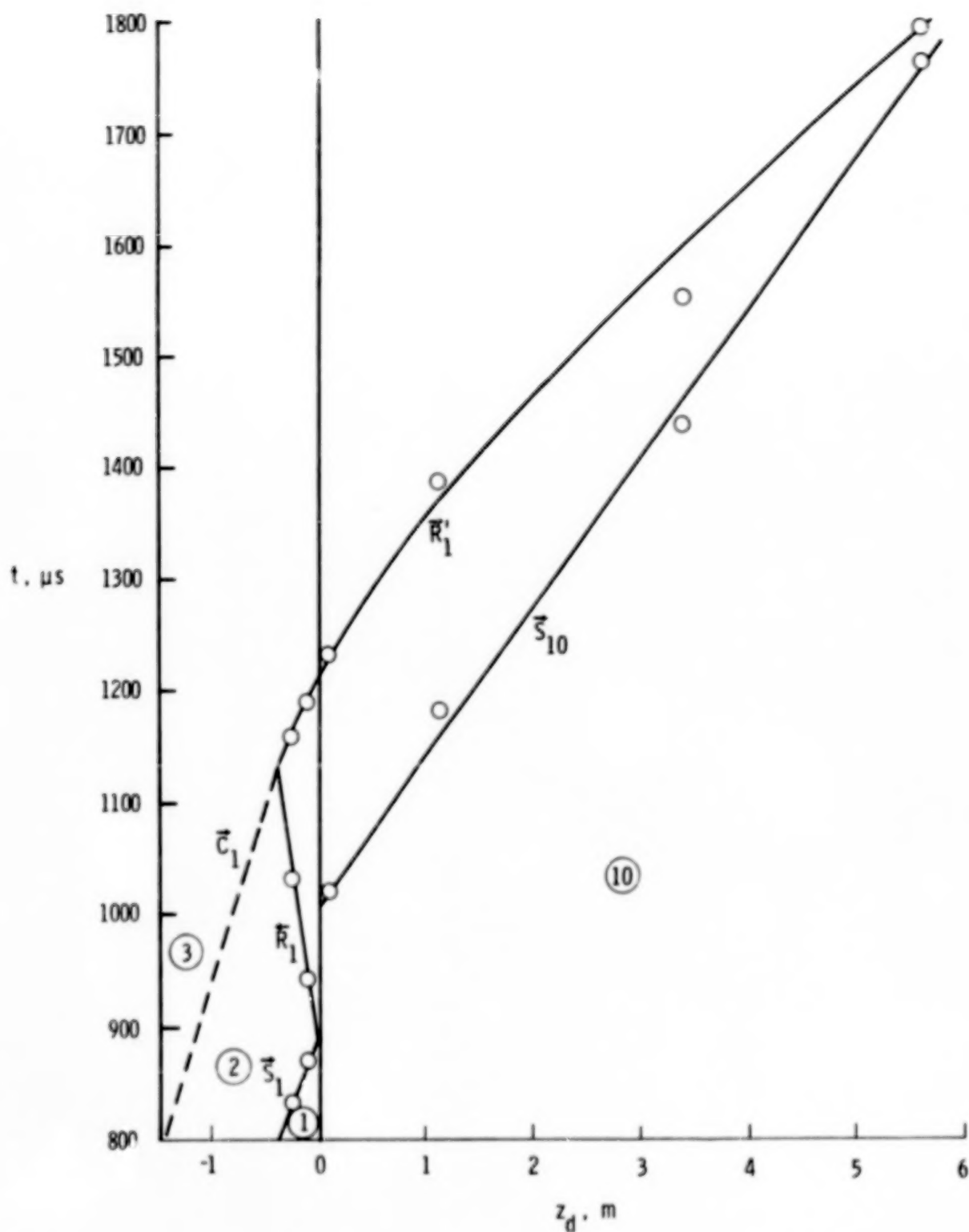


Figure 22.- Distance-time diagram showing refraction phenomenon of reflected shock in vicinity of secondary diaphragm.  $p_{10} \approx 16.00 \text{ N/m}^2$ ;  $p_1 = 0.69 \text{ kN/m}^2$ .

-----  $p_{20}$  predicted from conventional shock-tube theory  
corrected to value at interface (ref. 19)

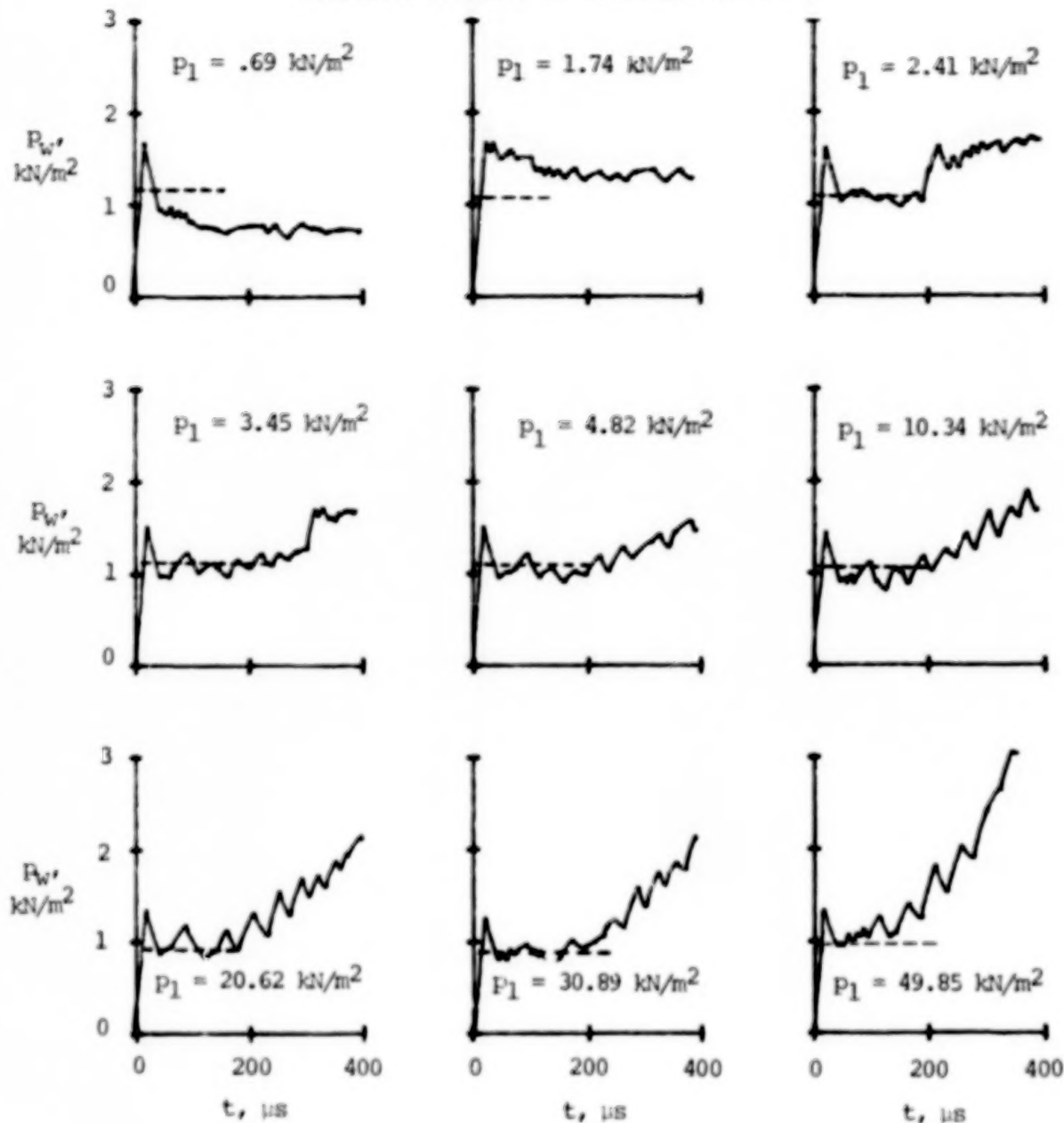


Figure 23.- Effect of quiescent test-gas pressure on time history of tube-wall pressure 2.54 cm upstream of tube exit.  $p_{10} \approx 16.00$  N/m<sup>2</sup>.



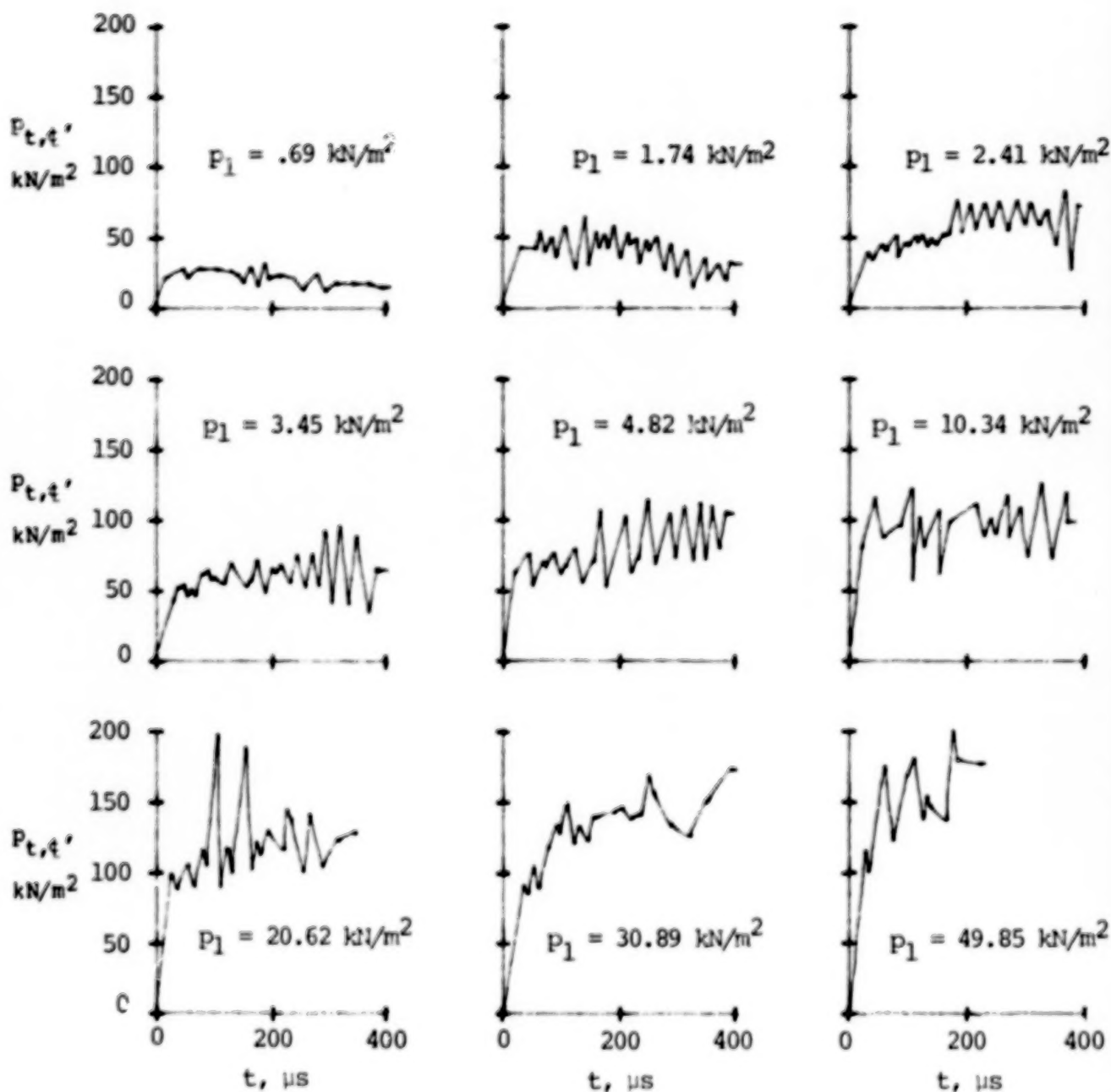


Figure 24.- Effect of quiescent test-gas pressure on centerline pitot-pressure time history.  $z_e = 5.64 \text{ cm}$ ;  $p_{10} = 16.00 \text{ N/m}^2$ .

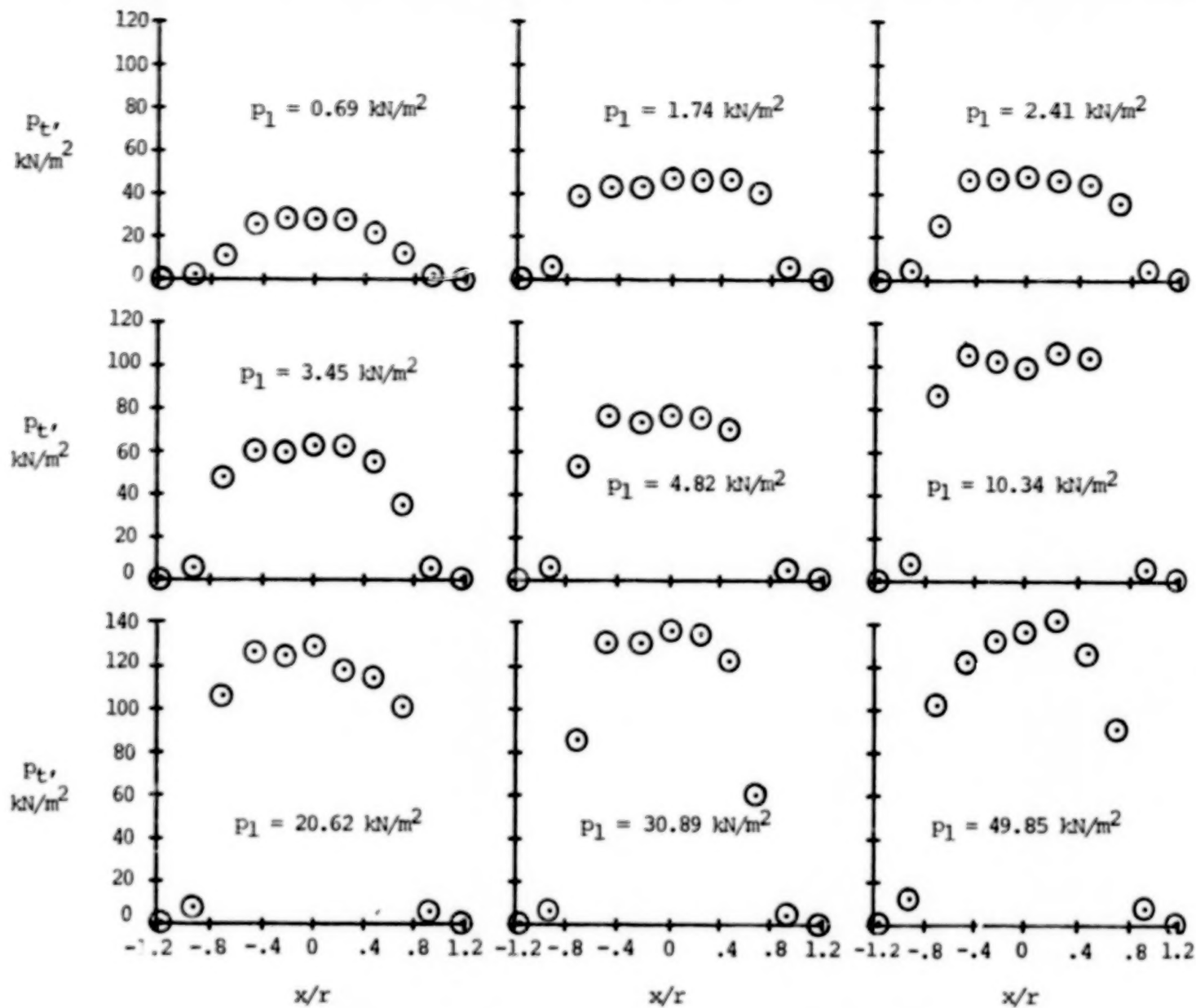
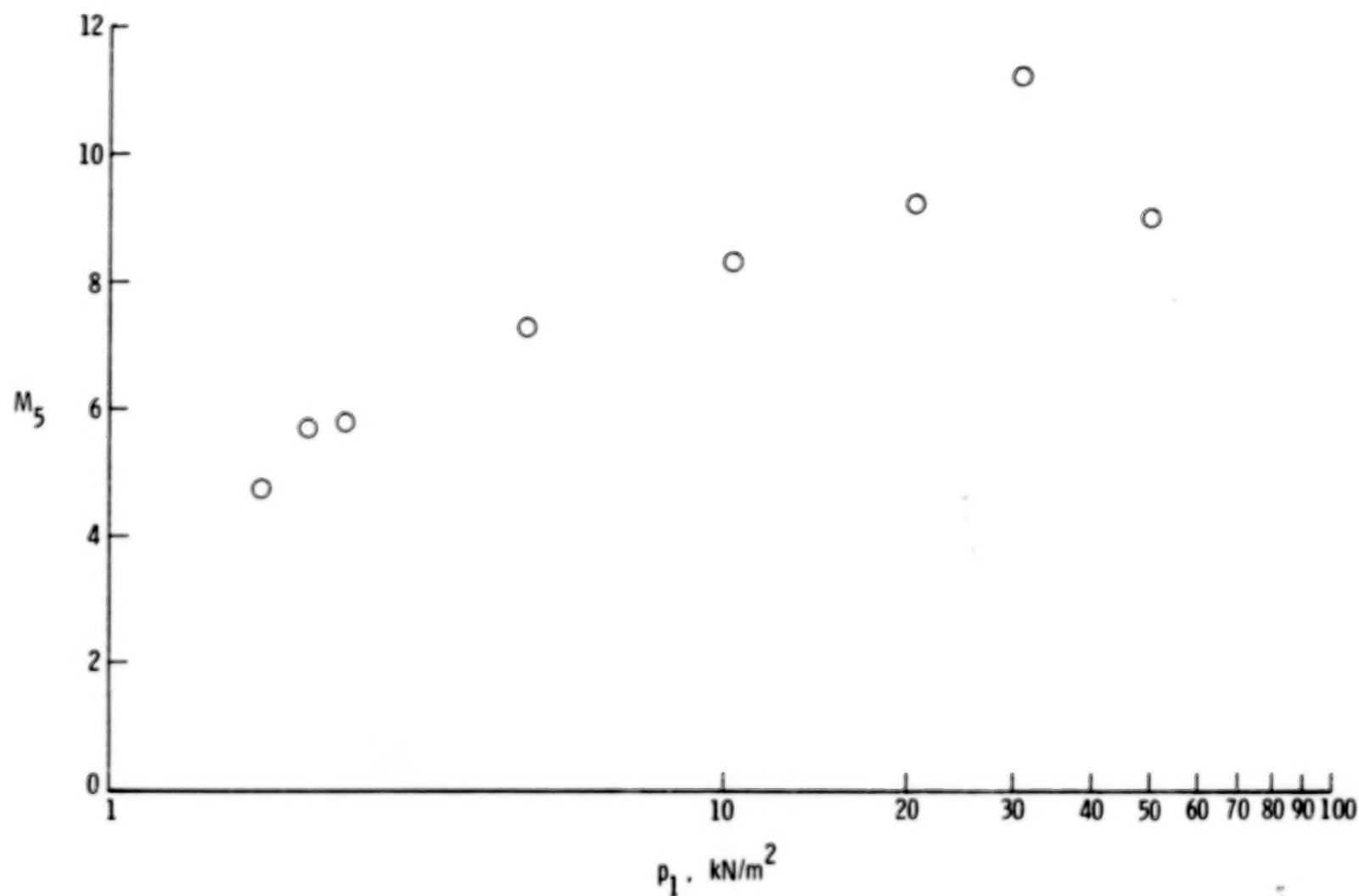


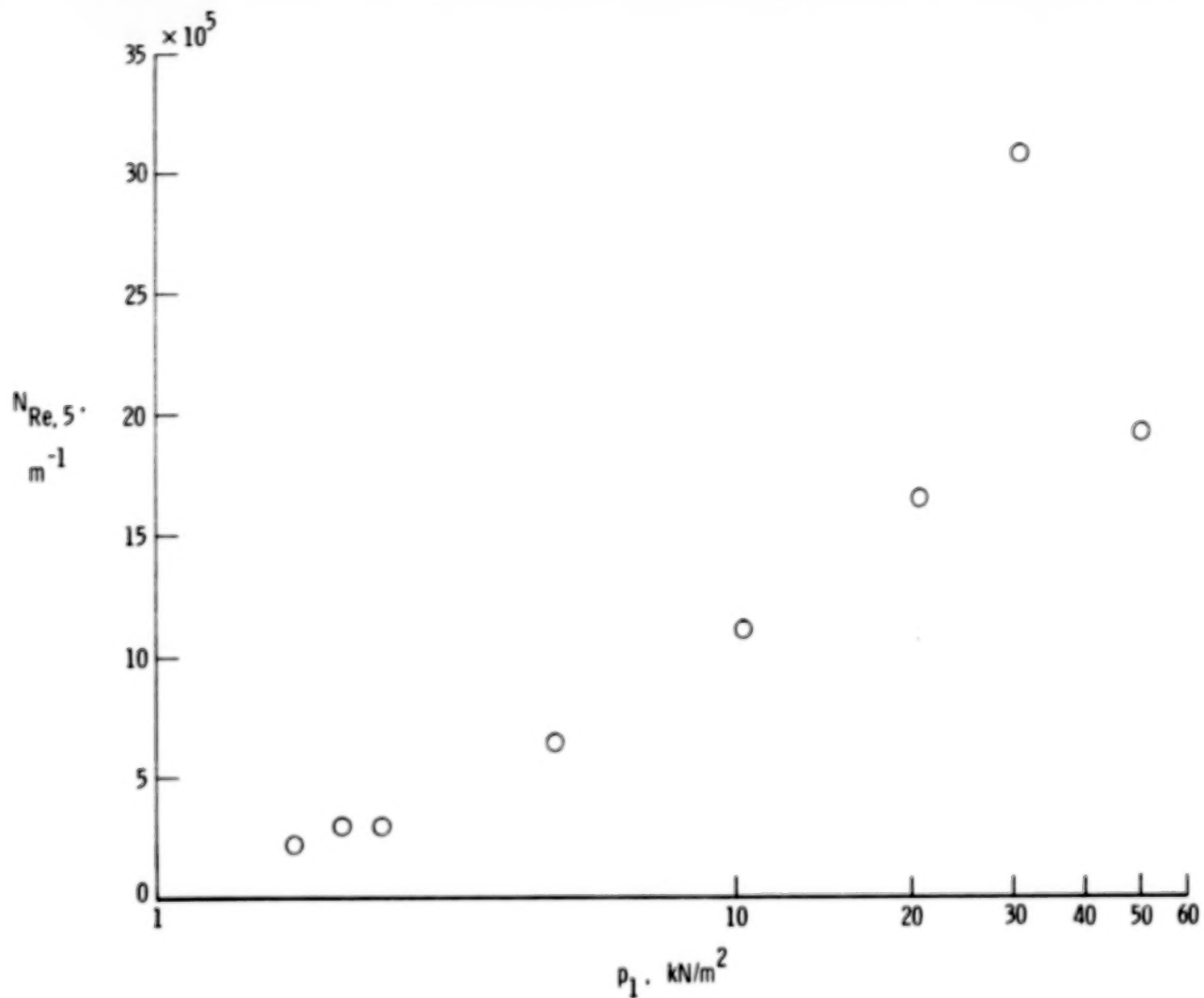
Figure 25.- Effect of quiescent test-gas pressure on pitot-pressure profile.  
 $z_e = 5.64 \text{ cm}$ ;  $t = 150 \text{ } \mu\text{s}$ ;  $p_{10} \approx 16.00 \text{ N/m}^2$ .

66



(a) Free-stream Mach number.

Figure 26.- Effect of quiescent test-gas pressure on free-stream Mach number and Reynolds number.  $p_{10} = 16.00 \text{ N/m}^2$ .



(b) Unit free-stream Reynolds number.

Figure 26.- Concluded.

67

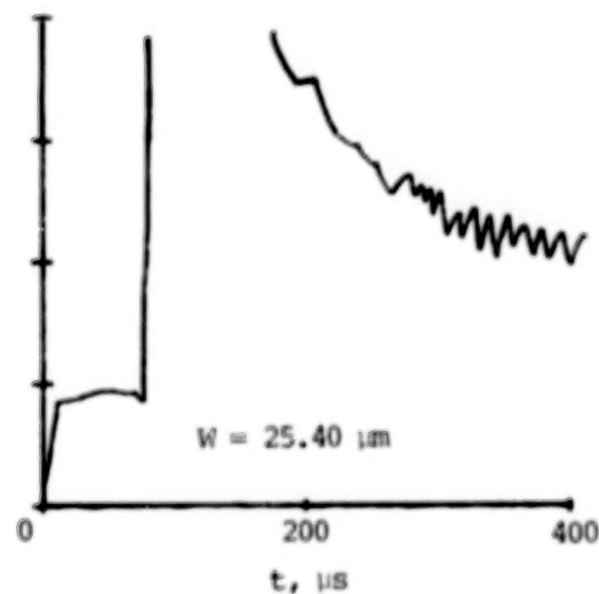
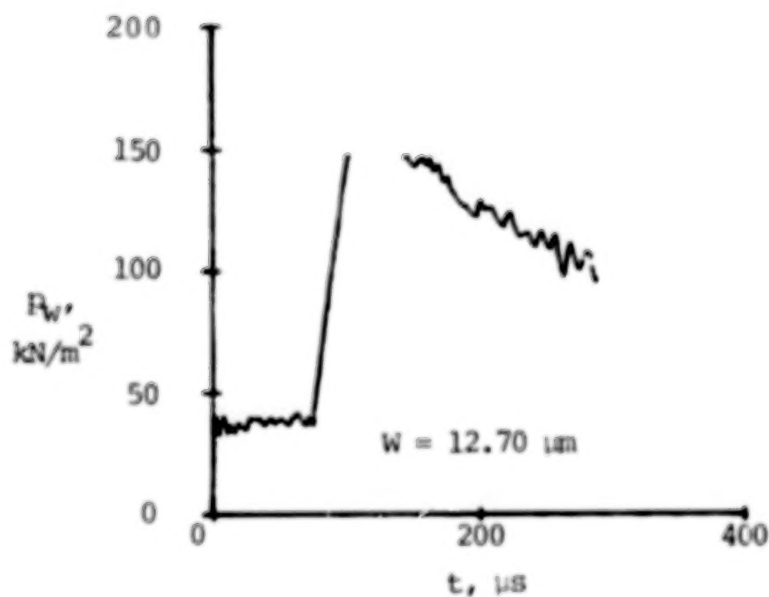
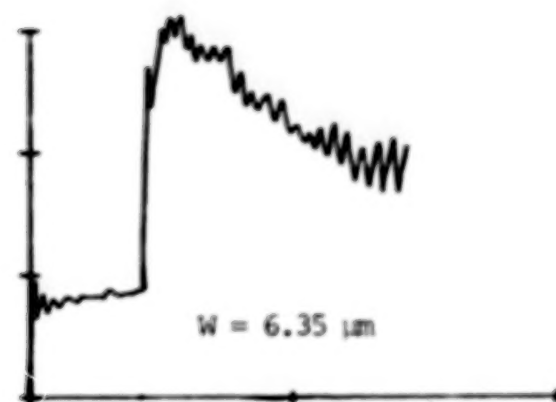
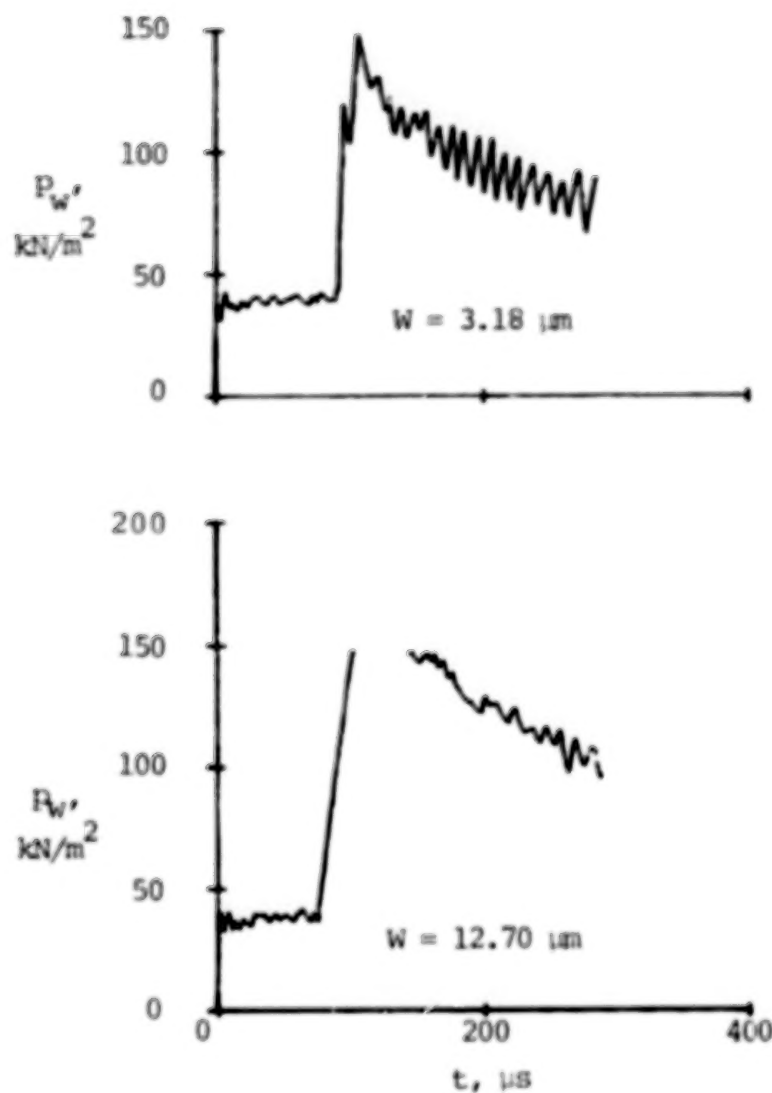
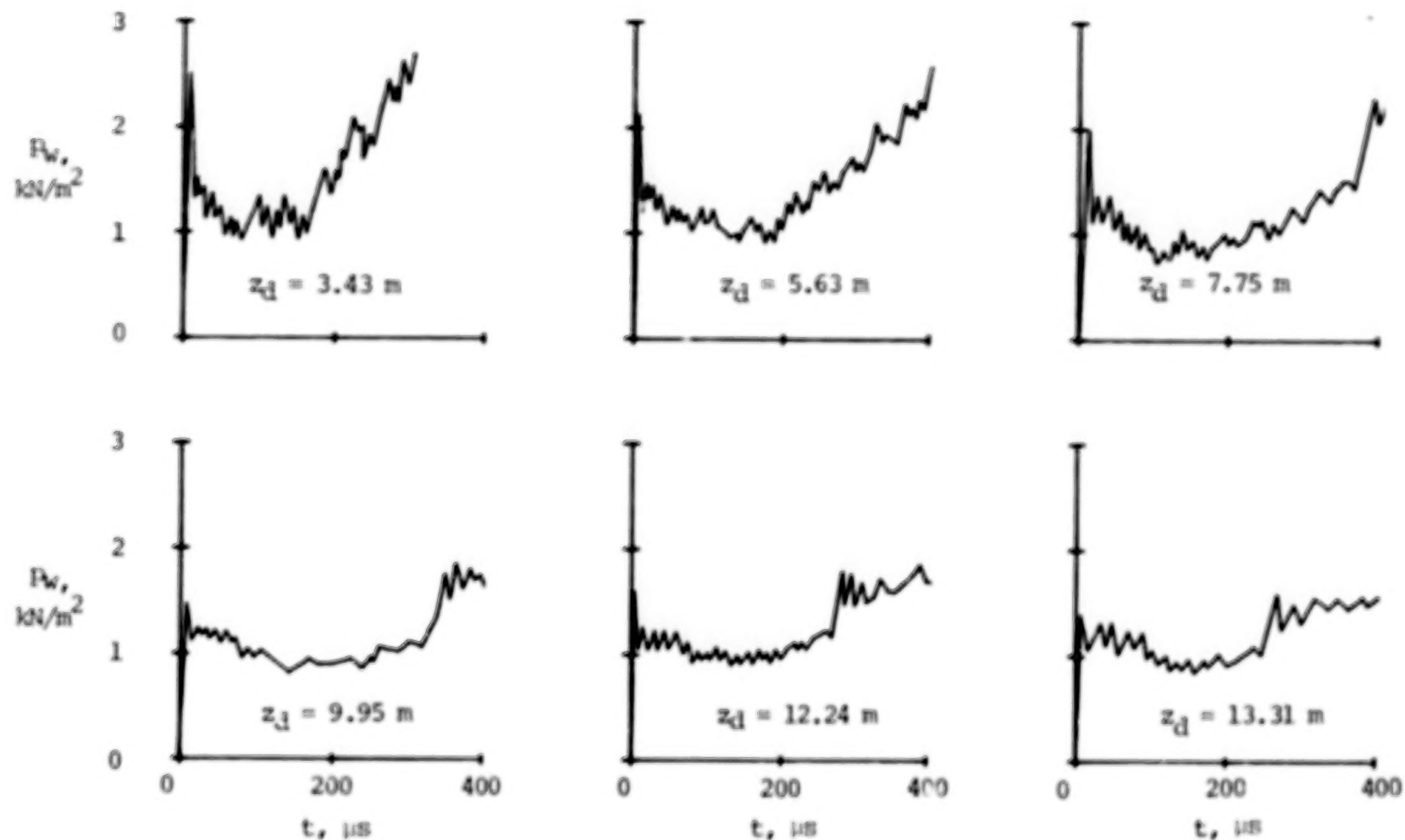


Figure 27.- Effect of secondary-diaphragm thickness on tube-wall-pressure time history measured 11.04 cm upstream of secondary diaphragm.  
 $p_1 = 2.07 \text{ kN/m}^2$ ;  $p_{10} = 16.00 \text{ N/m}^2$ .

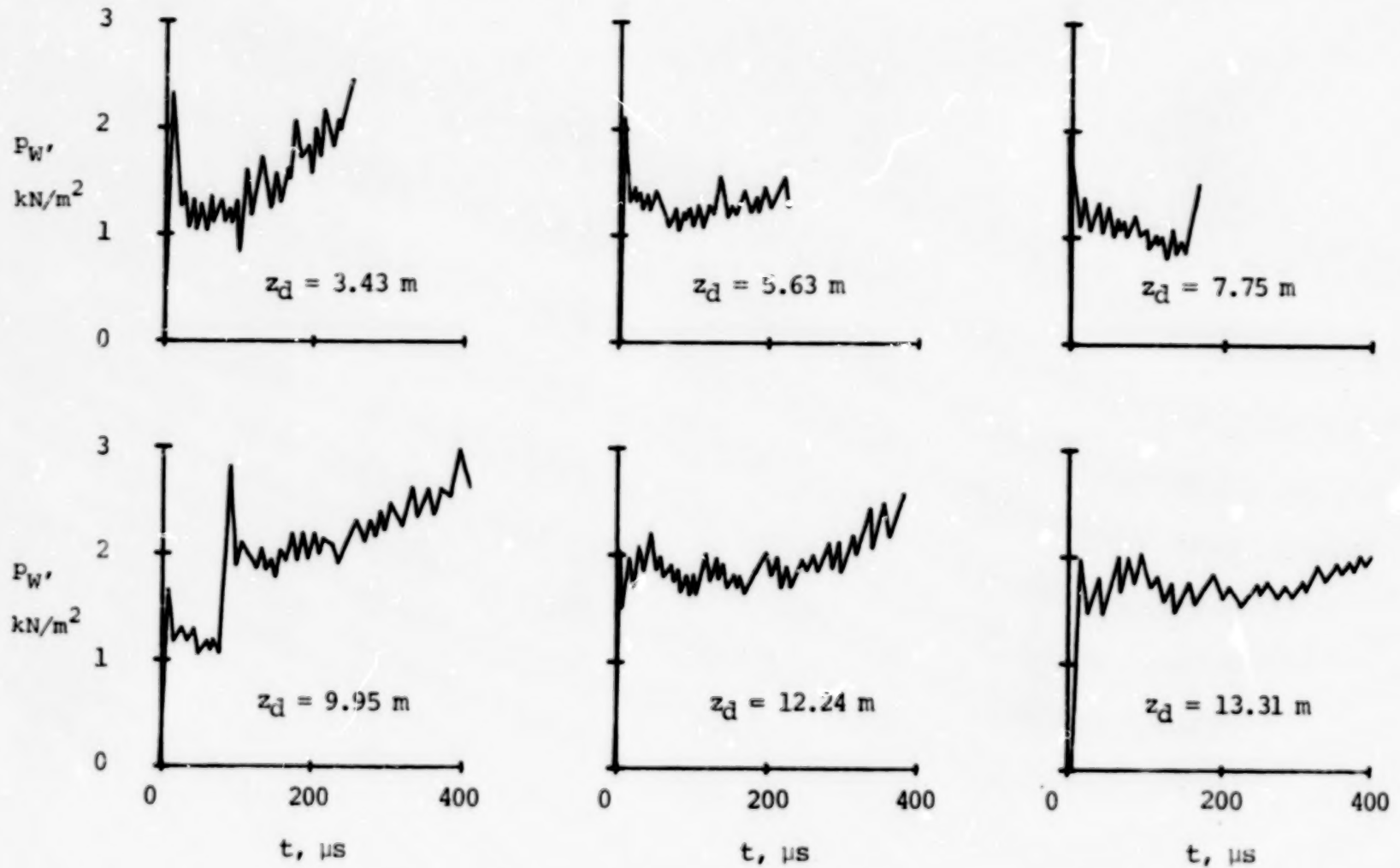


(a)  $W = 3.18 \mu\text{m}$ .

Figure 28.- Measured tube-wall-pressure time history at various distances downstream of secondary diaphragm for various secondary-diaphragm thicknesses.  $p_1 = 2.07 \text{ kN/m}^2$ ;  $p_{10} = 16.00 \text{ N/m}^2$ .



70



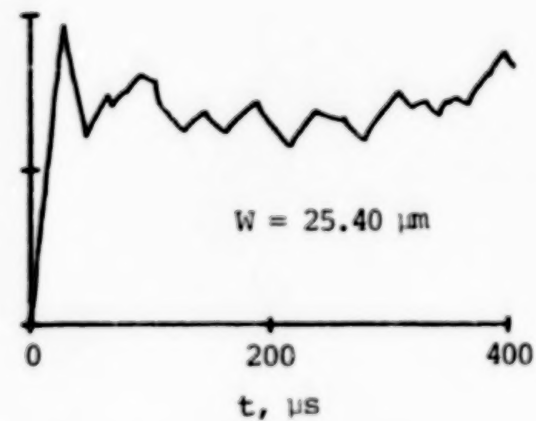
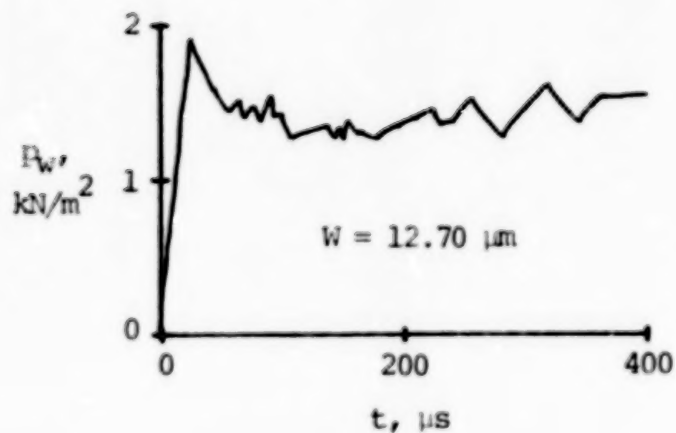
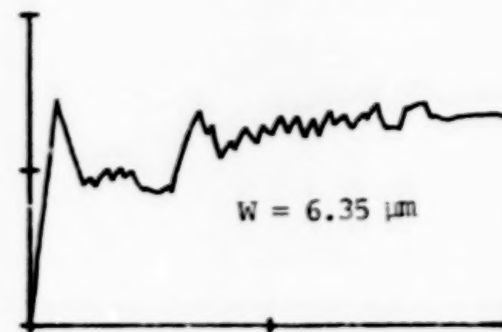
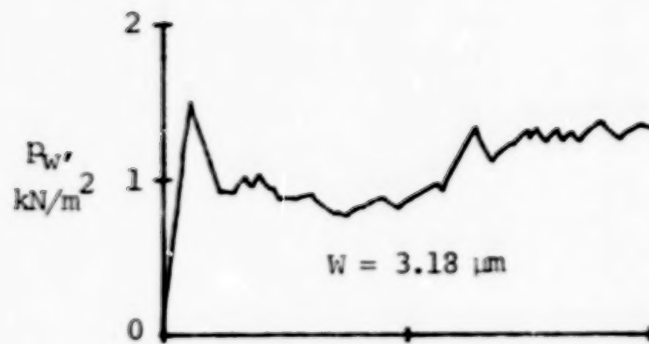


Figure 29.- Effect of secondary-diaphragm thickness on tube-wall-pressure time history  
2.54 cm upstream of tube exit.  $p_1 \approx 2.07 \text{ kN/m}^2$ ;  $p_{10} \approx 16.00 \text{ N/m}^2$ .

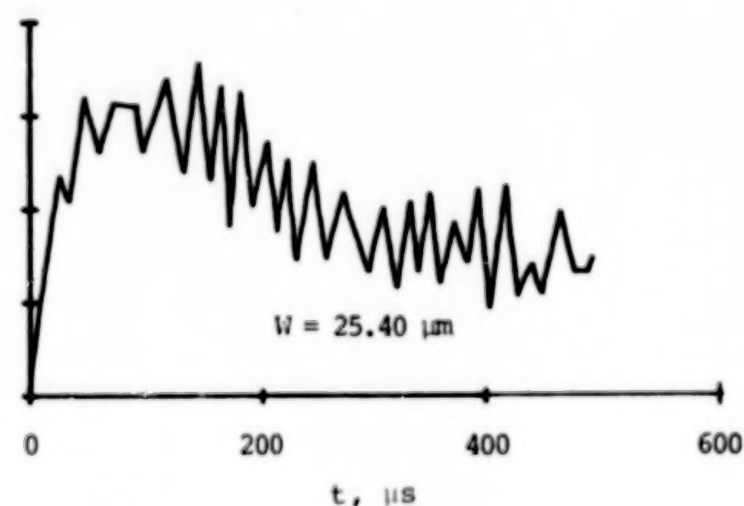
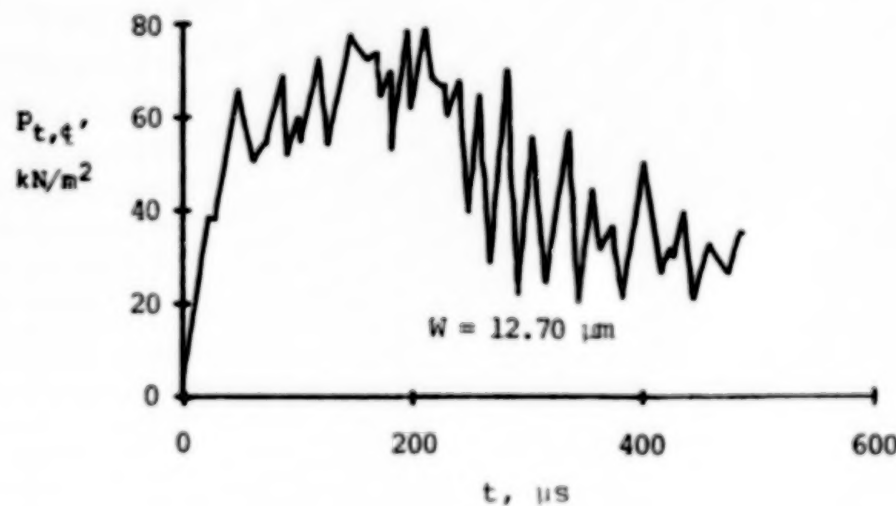
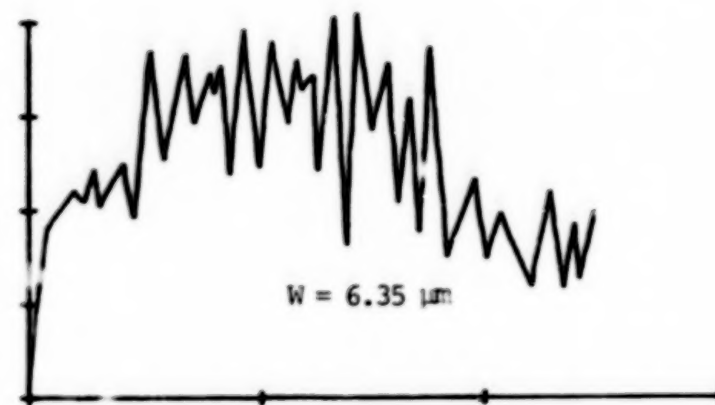
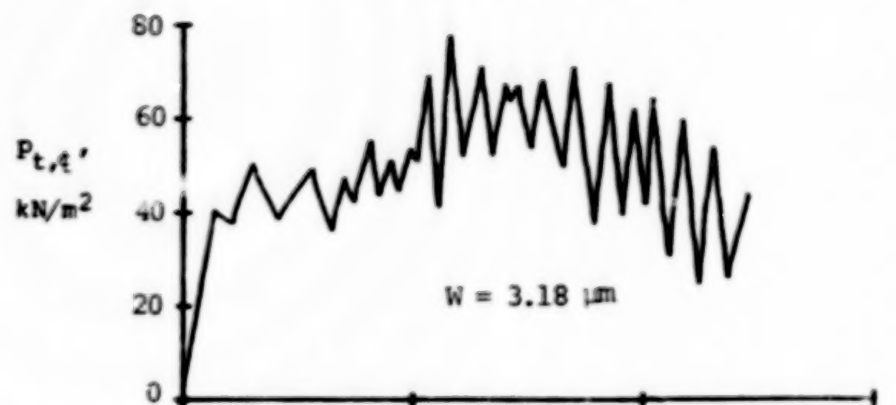
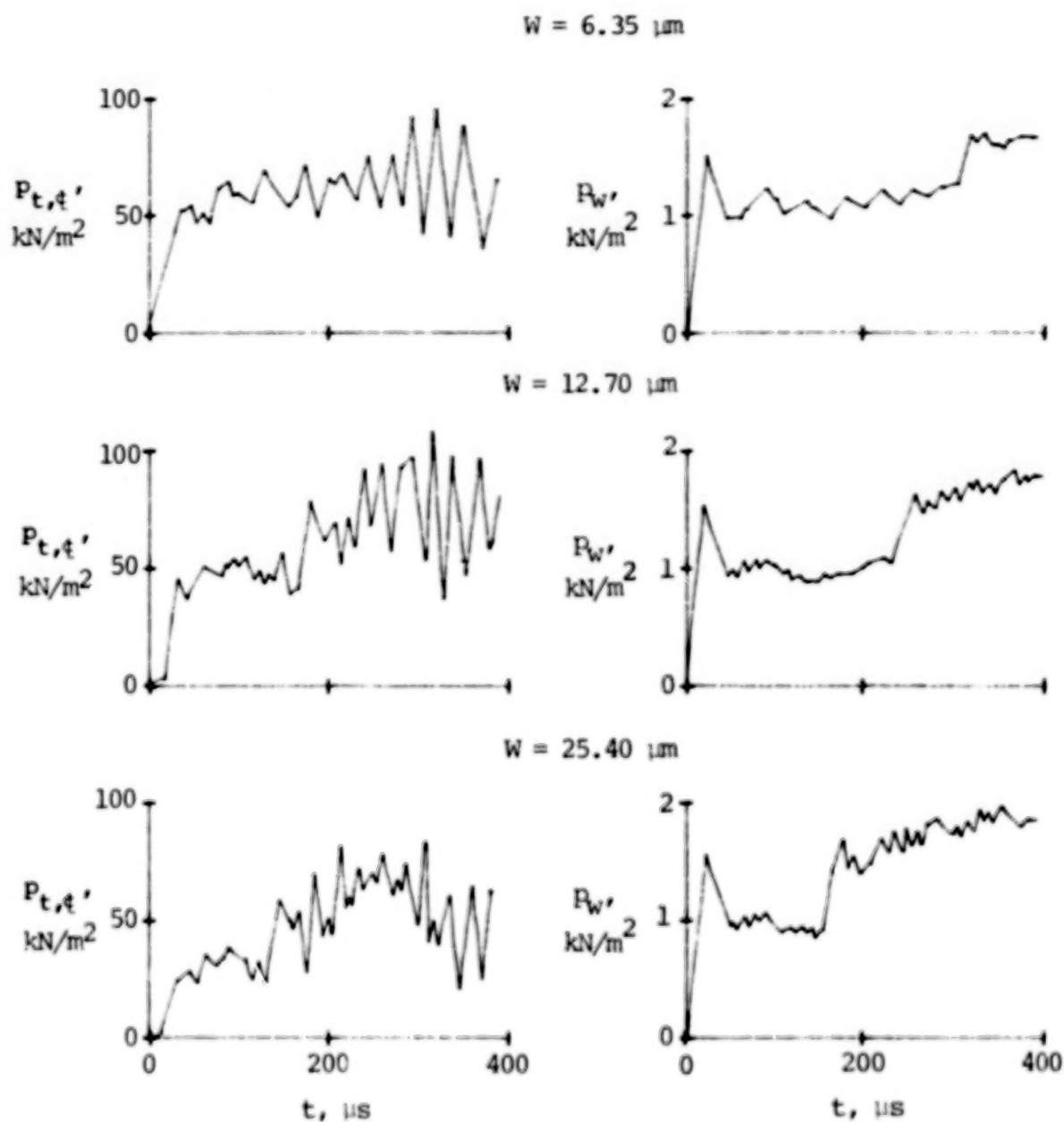
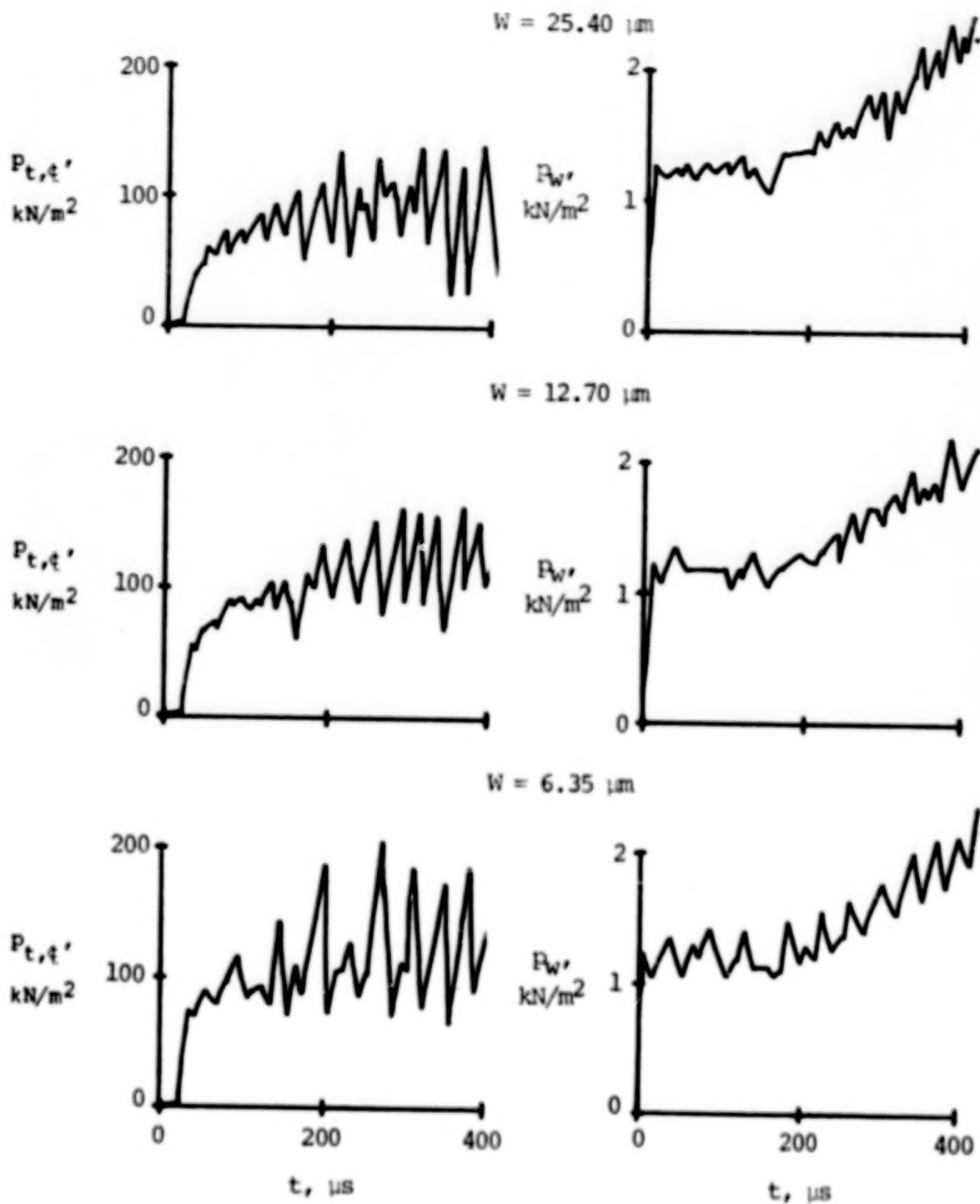


Figure 30.- Effect of secondary-diaphragm thickness on centerline pitot-pressure time history.  $z_e = 5.64 \text{ cm}$ ;  $p_1 \approx 2.07 \text{ kN/m}^2$ ;  $p_{10} \approx 16.00 \text{ N/m}^2$ .



(a)  $p_1 \approx 3.45 \text{ kN/m}^2$ .

Figure 31.- Effect of secondary-diaphragm thickness on time histories of center-line pitot pressure ( $z_e = 5.64 \text{ cm}$ ) and tube-wall pressure  $2.54 \text{ cm}$  upstream of tube exit for two values of  $p_1$ .  $p_{10} \approx 16.00 \text{ N/m}^2$ .



(b)  $p_1 \approx 10.34 \text{ kN/m}^2$ .

Figure 31.- Concluded.

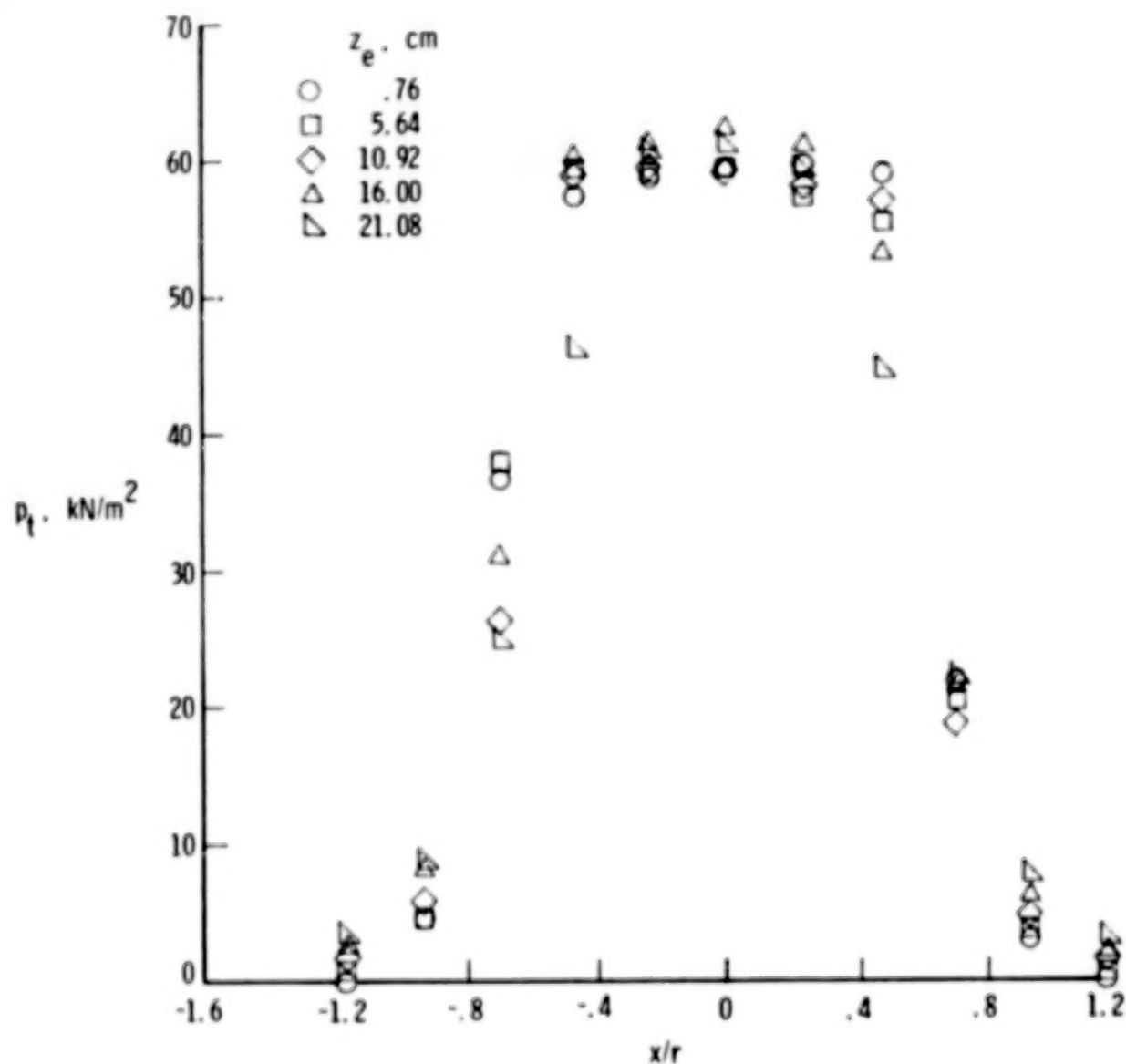


Figure 32.- Pitot-pressure profile at various distances downstream of tube exit.  
 $p_1 \approx 3.45 \text{ kN/m}^2$ ;  $p_{10} \approx 16.00 \text{ N/m}^2$ ;  $t = 200 \text{ } \mu\text{s}$ .



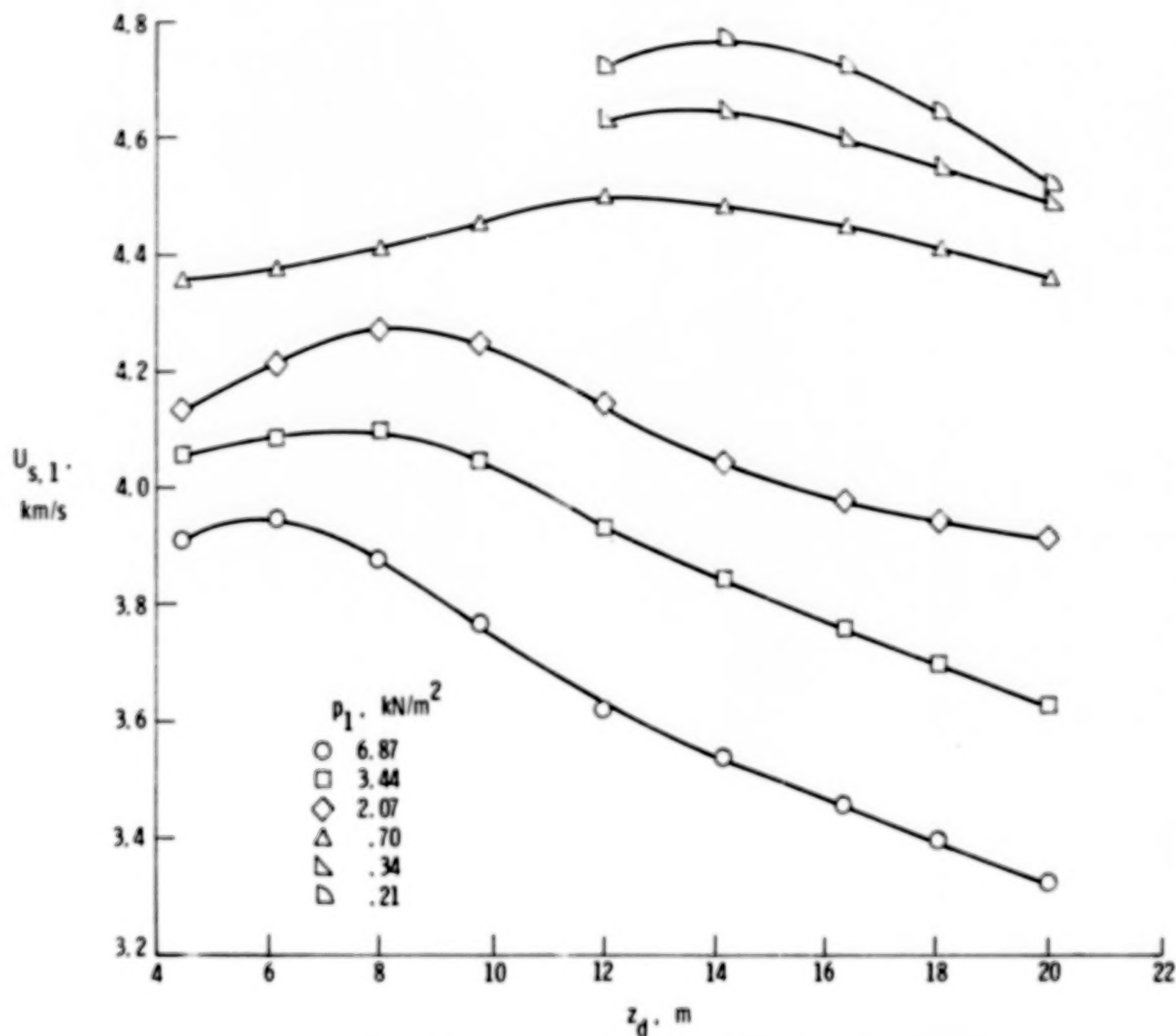


Figure 33.- Measured incident shock velocity as a function of distance downstream of diaphragm for various quiescent test-gas pressures in shock-tube mode.

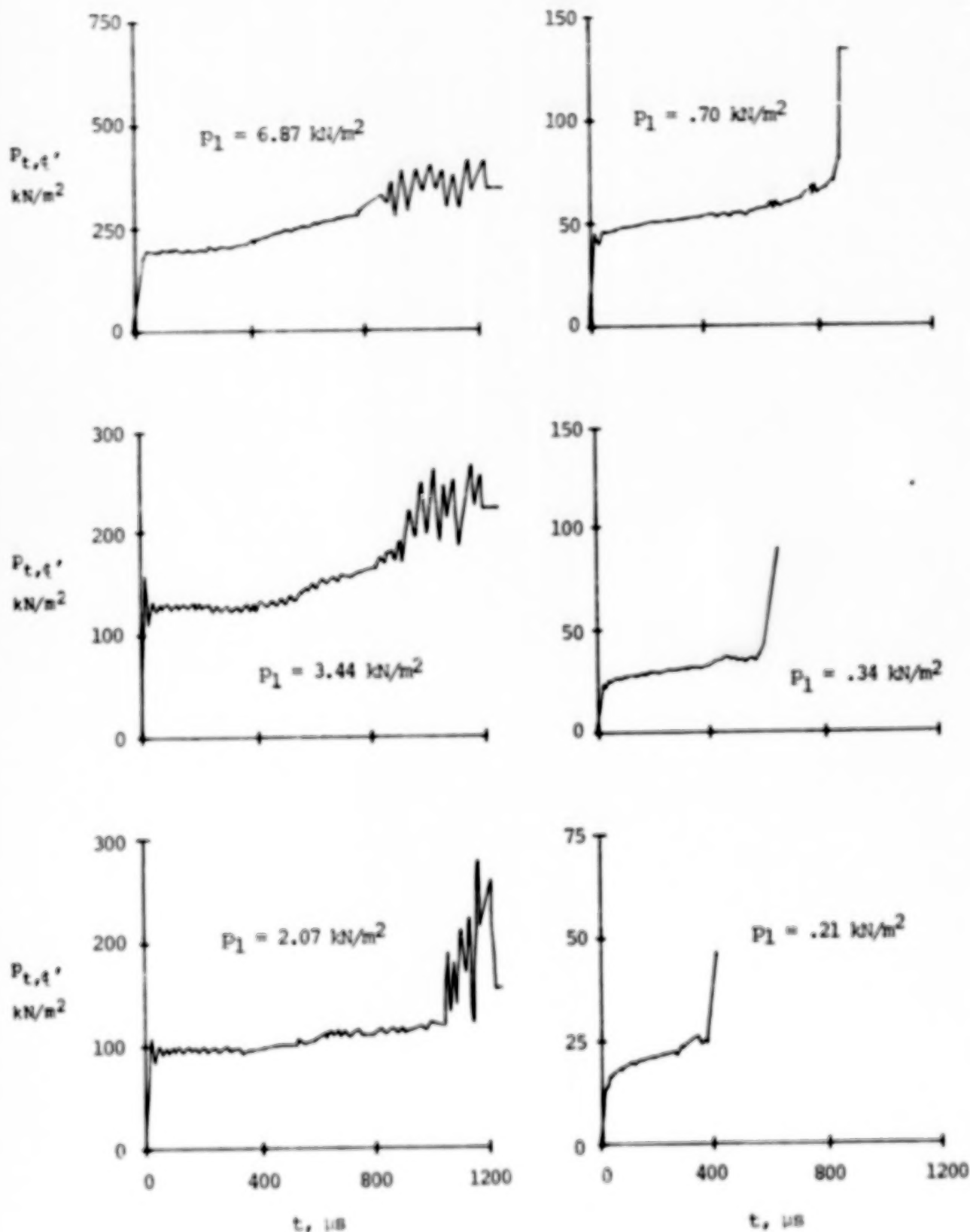


Figure 34.- Effect of quiescent test-gas pressure on centerline pitot-pressure time history in shock-tube mode.  $z_e = 5.64 \text{ cm}$ . Note scale change.

78

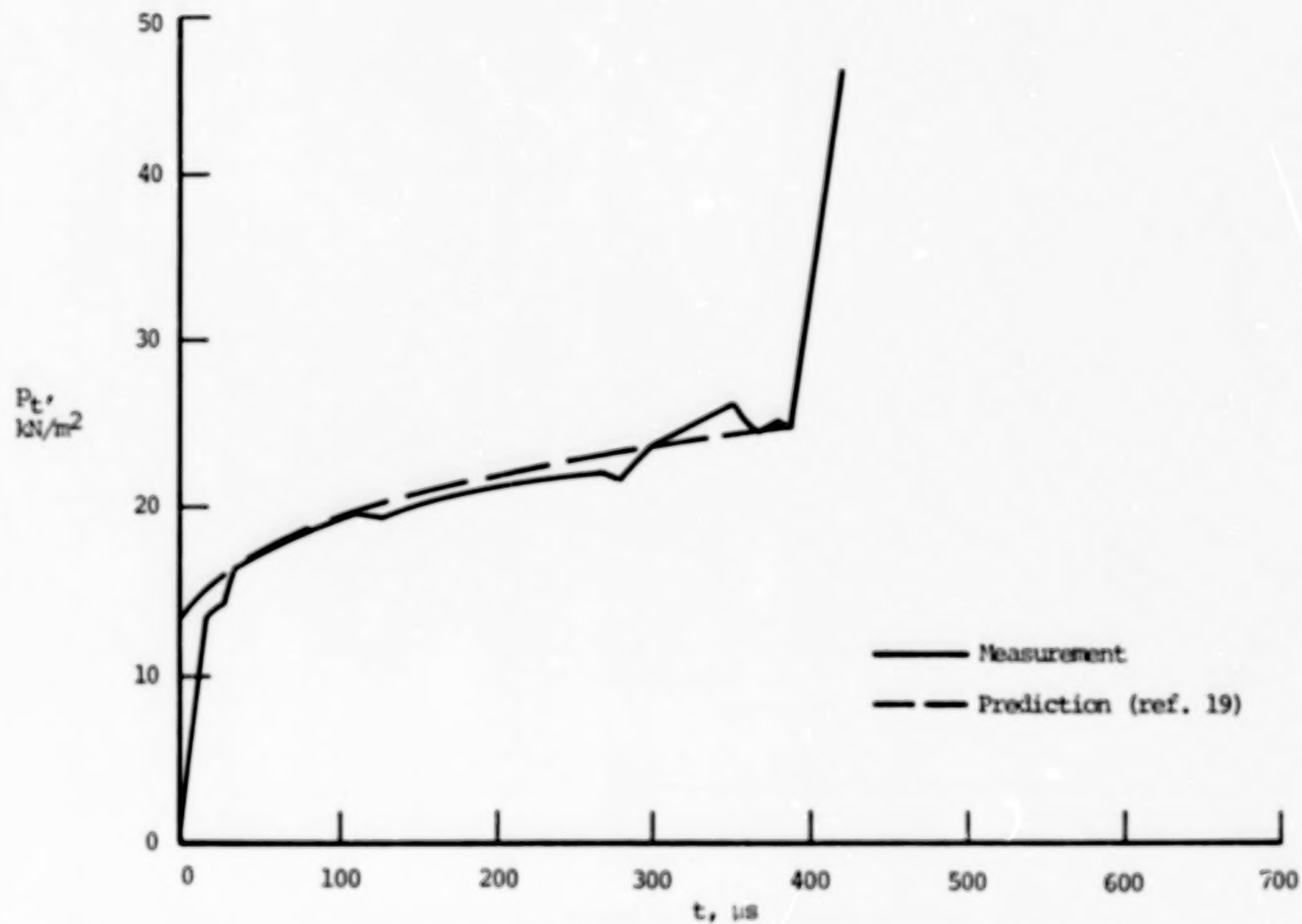
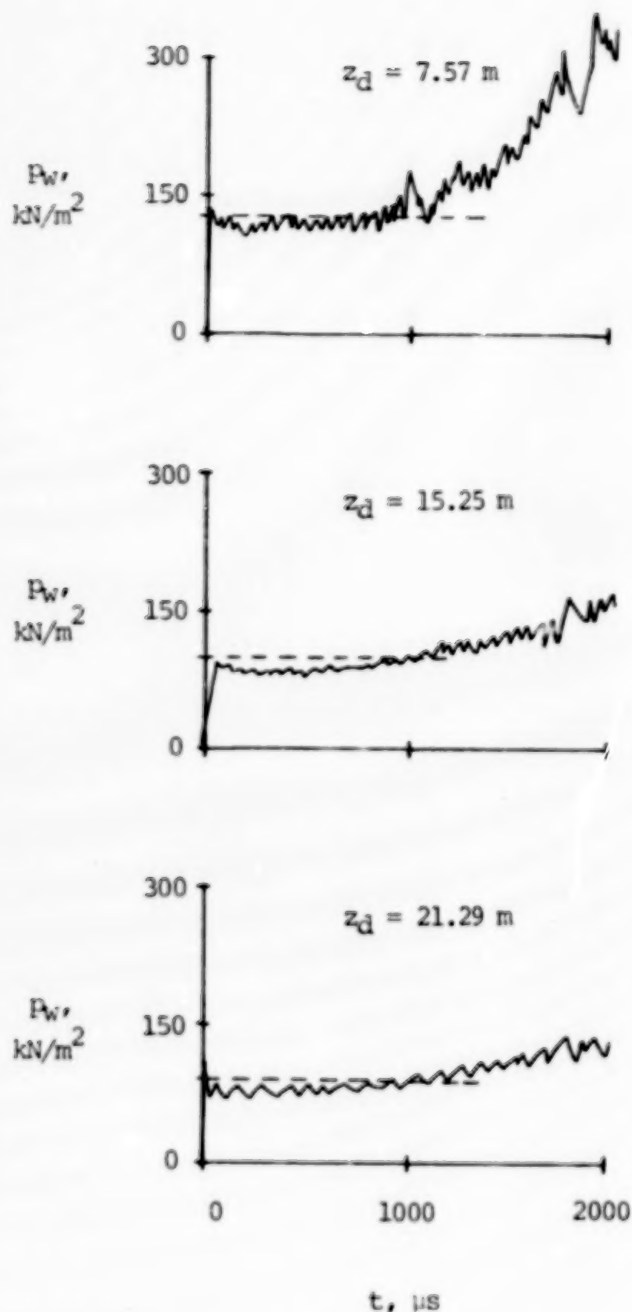
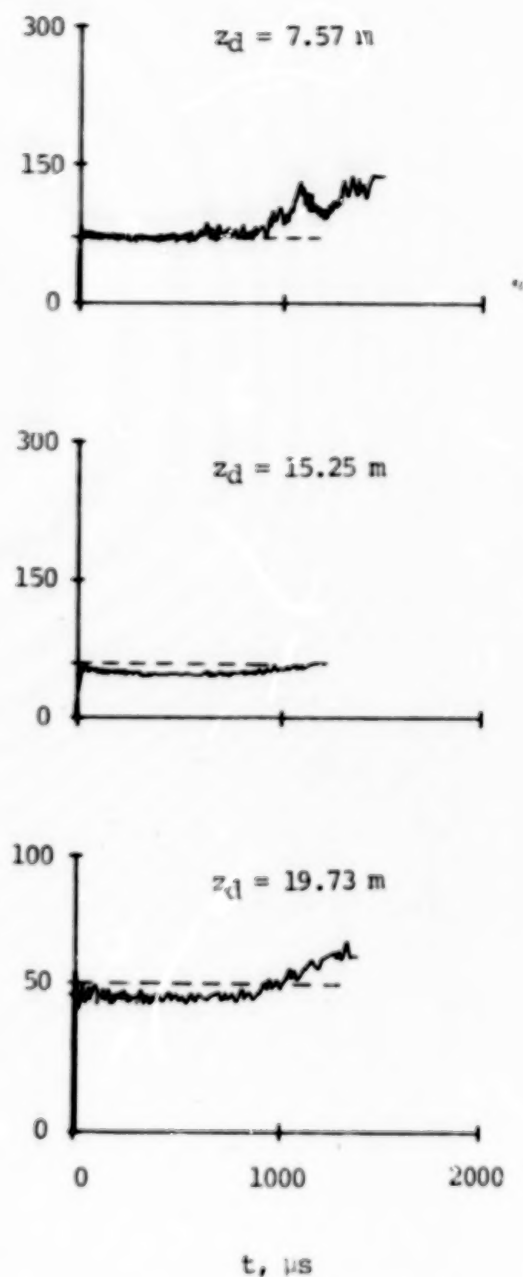


Figure 35.- Comparison of predicted and measured centerline pitot-pressure time histories between incident shock and interface in shock-tube mode.  $p_1 = 0.21 \text{ kN/m}^2$ .

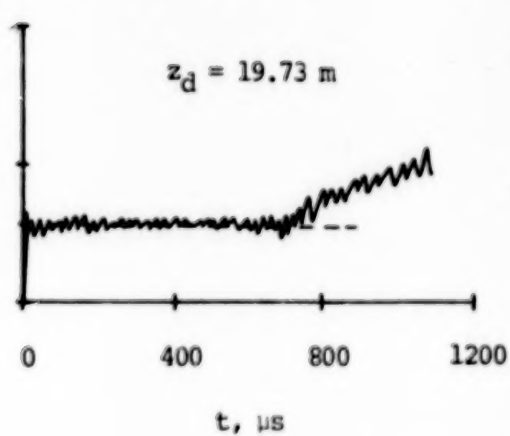
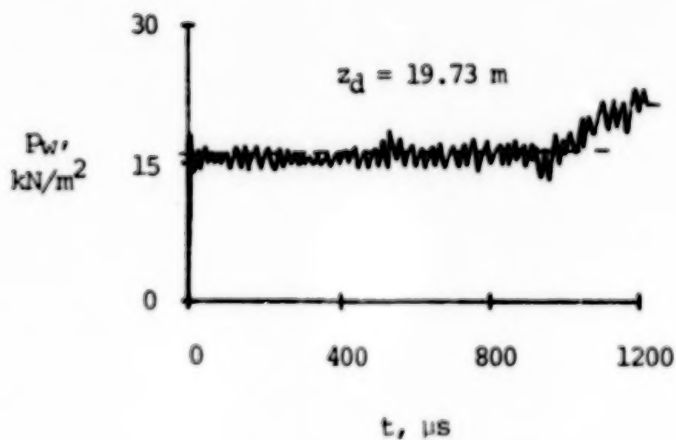
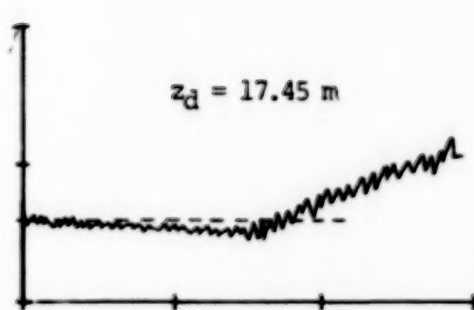
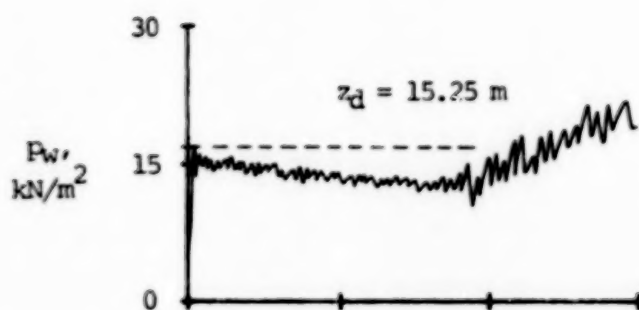
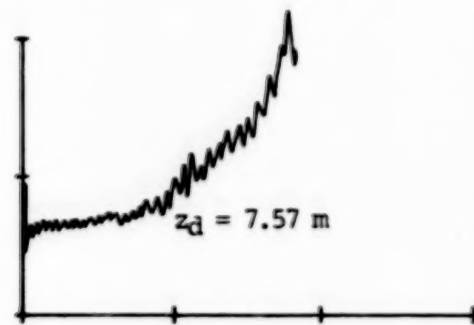
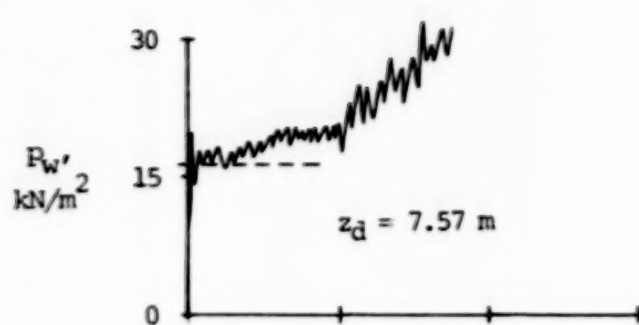


(a)  $p_1 = 6.87 \text{ kN/m}^2$ .



(b)  $p_1 = 3.44 \text{ kN/m}^2$ .

Figure 36.- Tube-wall-pressure time history at various distances downstream of diaphragm in shock-tube mode for several values of  $p_1$ . Dashed lines are computed using conventional shock-tube theory. Note scale change.



(c)  $p_1 = 0.70$  kN/m<sup>2</sup>.

(d)  $p_1 = 0.34$  kN/m<sup>2</sup>.

Figure 36.- Concluded.

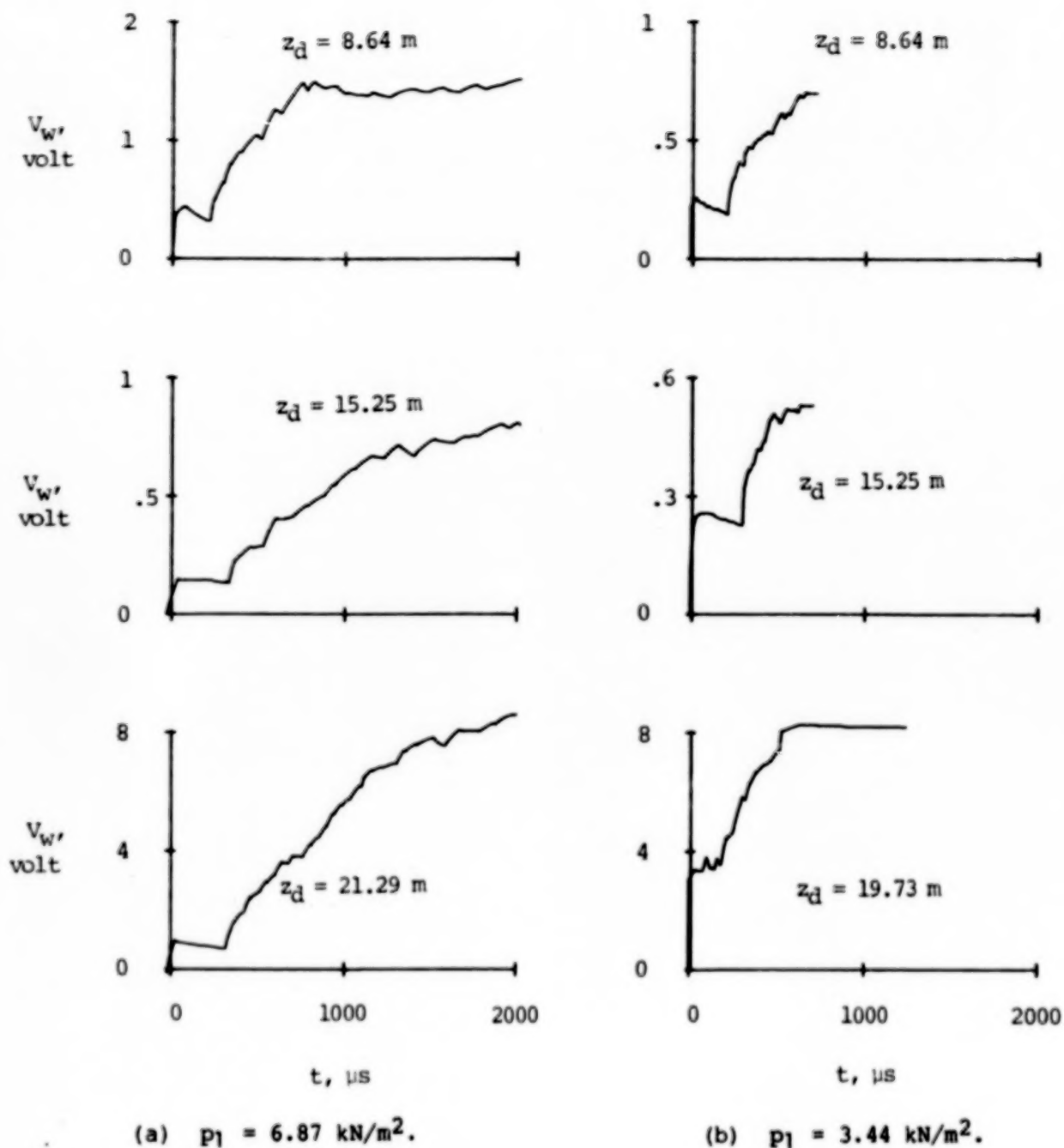
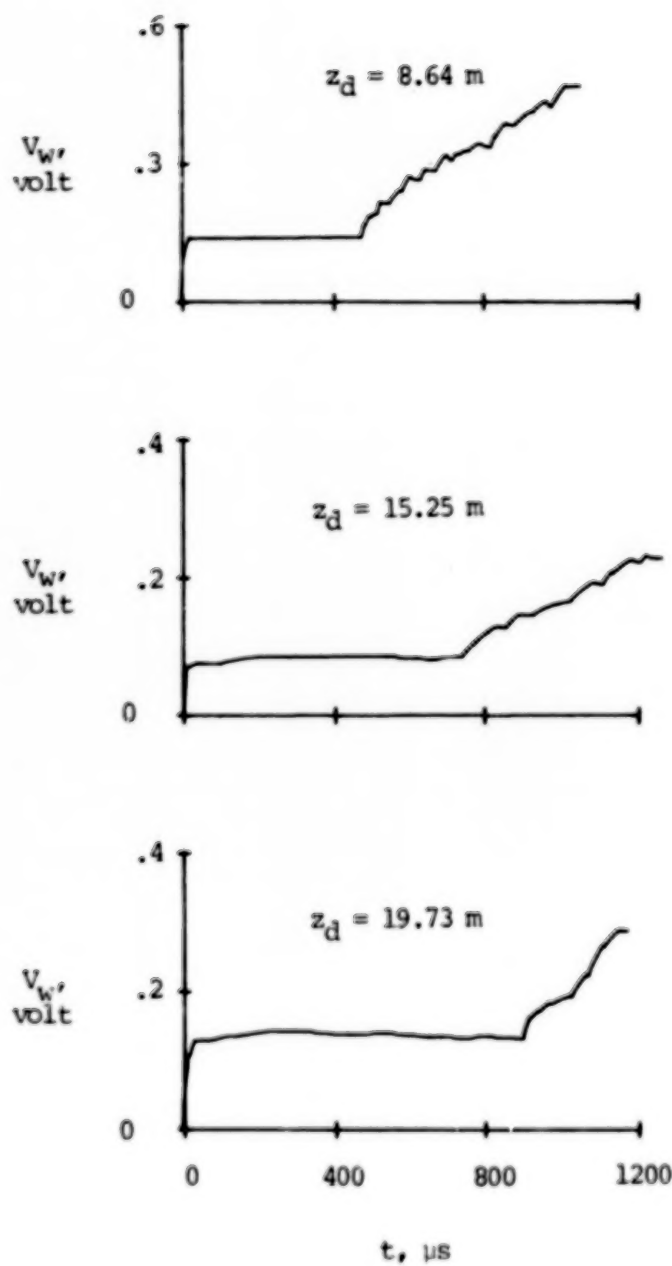
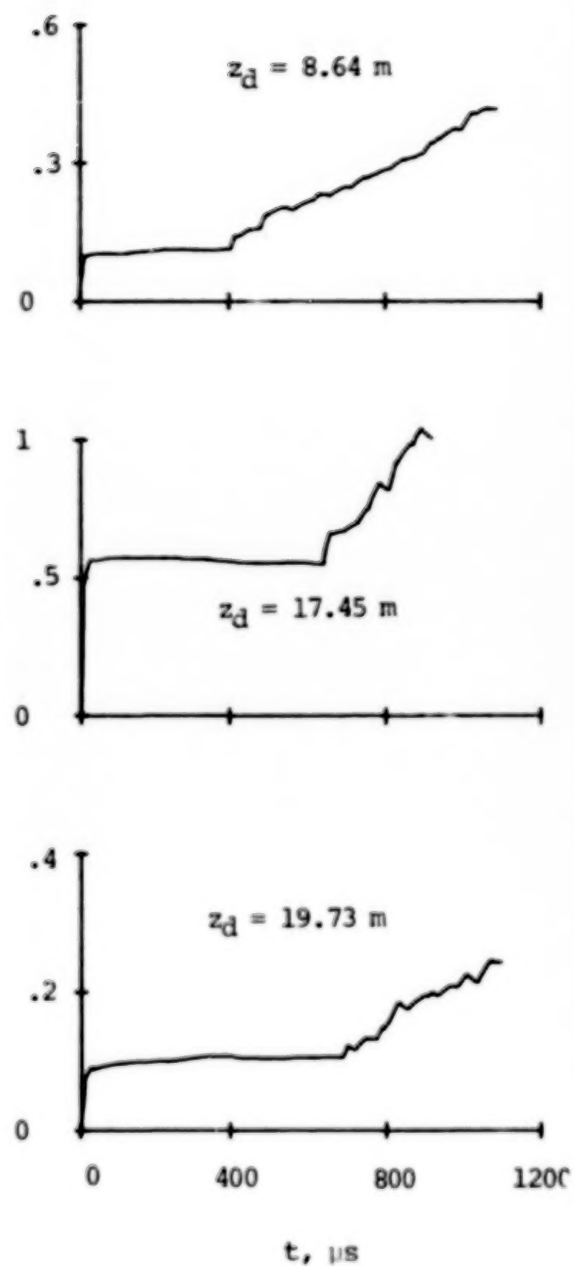


Figure 37.- Time history of tube-wall heat-transfer-gage voltage output at various distances downstream of diaphragm in shock-tube mode. (Note scale change.)





(c)  $p_1 = 0.70 \text{ kN/m}^2$ .



(d)  $p_1 = 0.34 \text{ kN/m}^2$ .

Figure 37.- Concluded.

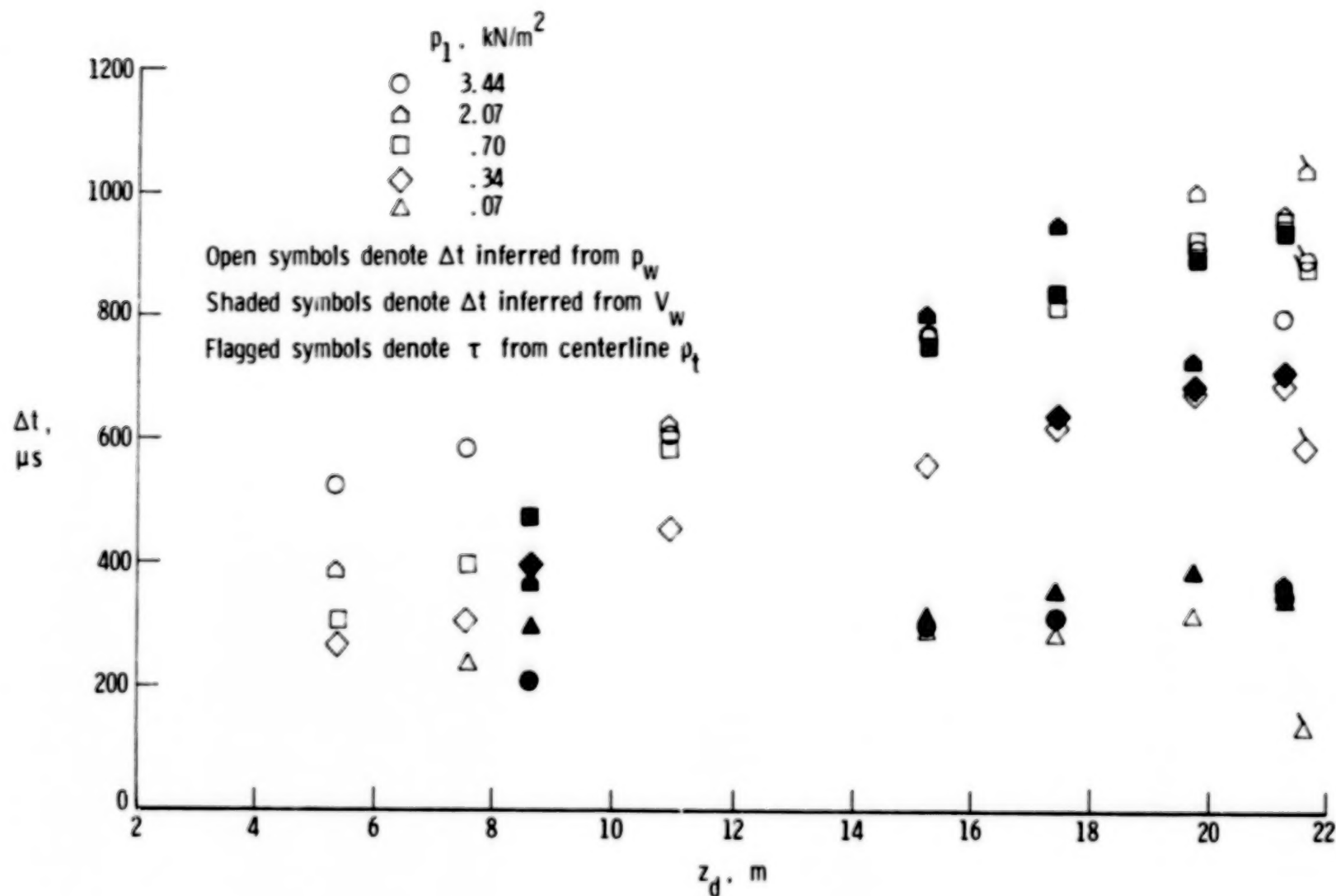


Figure 38.- Time interval between incident shock arrival and departure from quasi-steady flow as a function of distance from diaphragm in shock-tube mode.

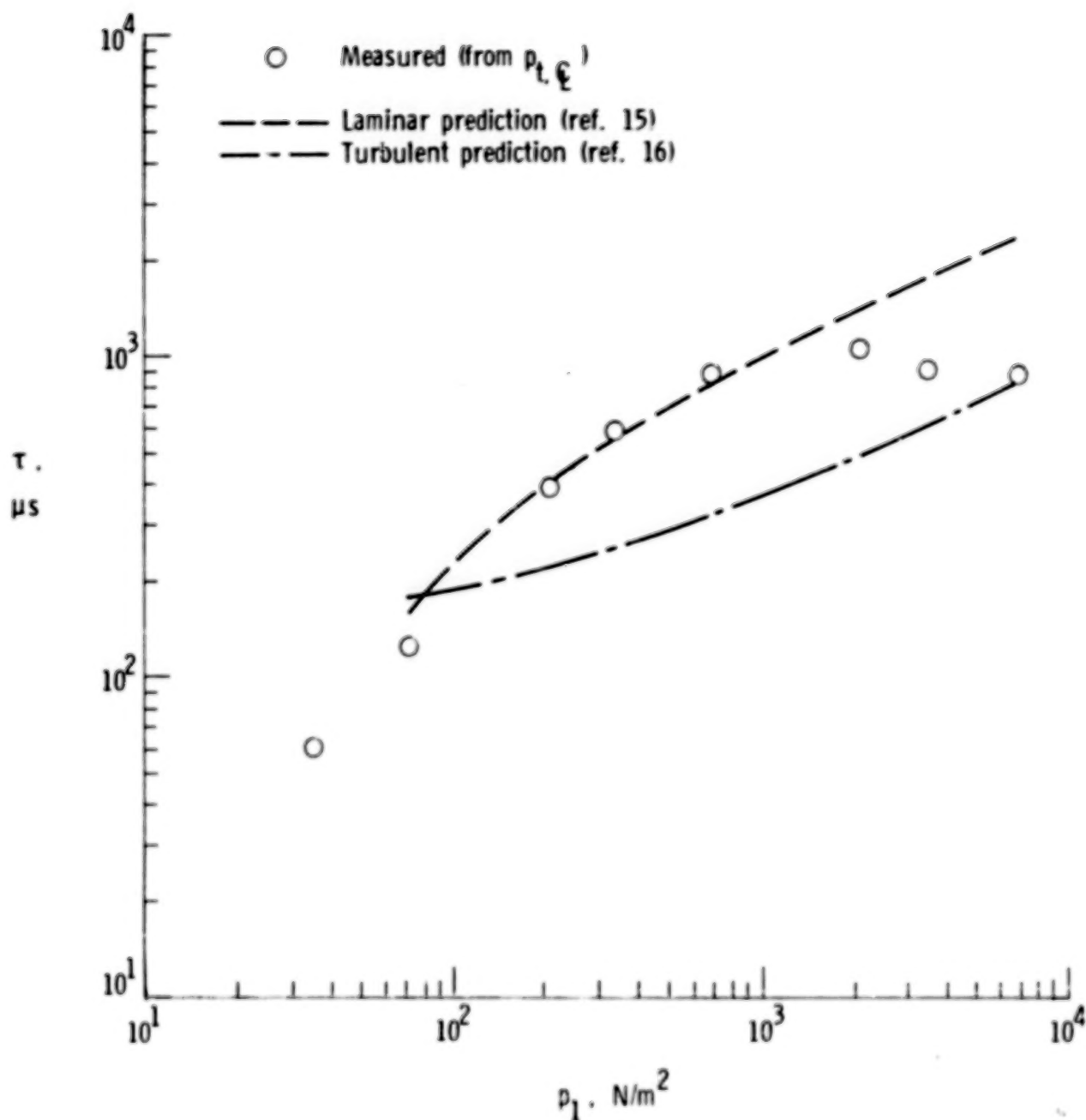


Figure 39.- Time interval between incident shock and interface at  $z_d = 21.6$  m as a function of quiescent test-gas pressure.

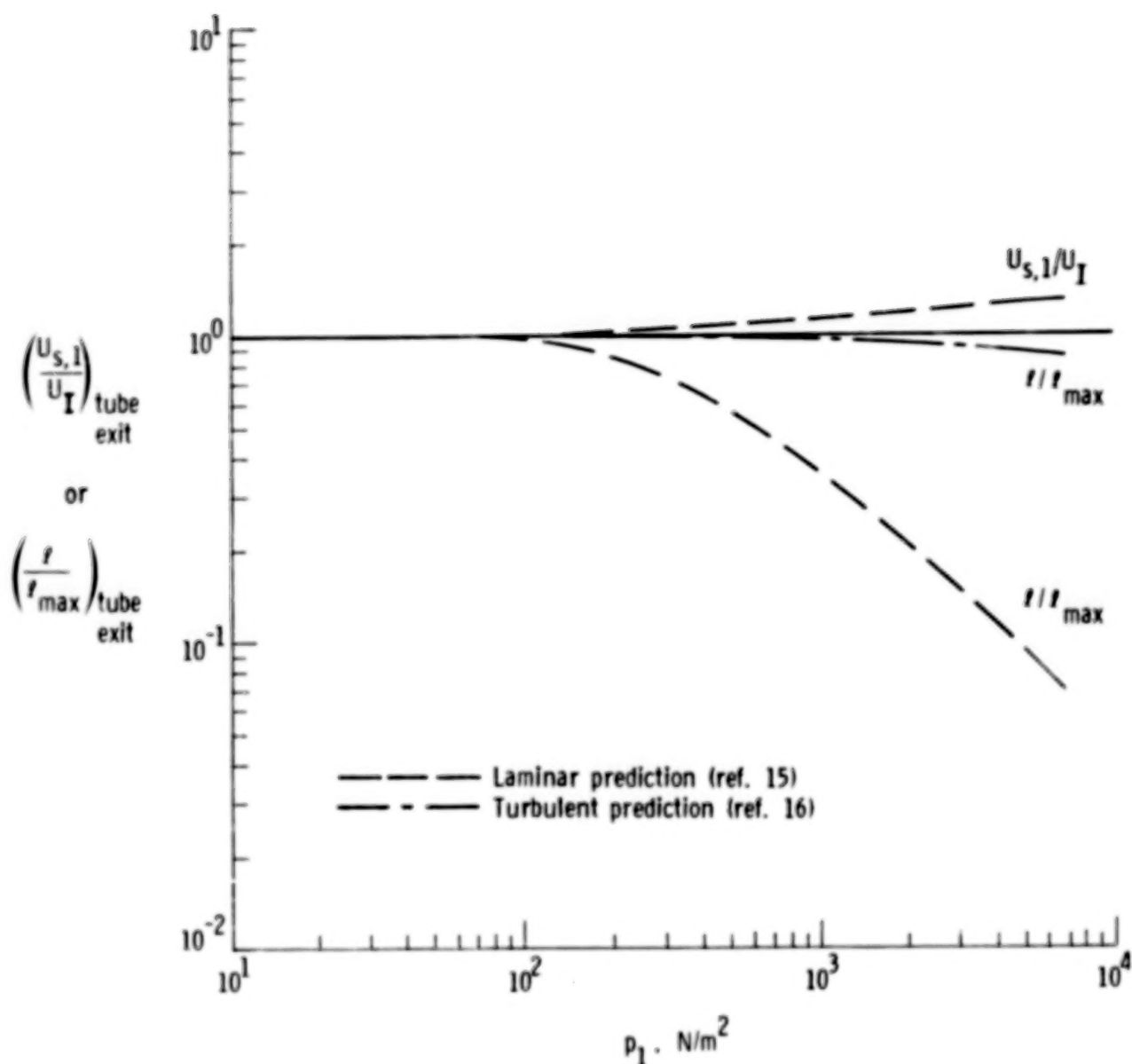


Figure 40.- Predicted ratio of separation distance to maximum separation distance and of incident shock velocity to interface velocity at  $z_d = 21.6$  m as a function of test-gas pressure in shock-tube mode.

1. Report No. NASA TP-1317		2. Government Accession No.		3. Recipient's Catalog No.	
4. Title and Subtitle EXPERIMENTAL PERFECT-GAS STUDY OF EXPANSION-TUBE FLOW CHARACTERISTICS				5. Report Date December 1976	
				6. Performing Organization Code	
7. Author(s) Judy L. Shinn and Charles G. Miller III				8. Performing Organization Report No. L-12407	
				10. Work Unit No. 506-26-13-01	
9. Performing Organization Name and Address NASA Langley Research Center Hampton, VA 23665				11. Contract or Grant No.	
				13. Type of Report and Period Covered Technical Paper	
12. Sponsoring Agency Name and Address National Aeronautics and Space Administration Washington, DC 20546				14. Sponsoring Agency Code	
15. Supplementary Notes					
16. Abstract  Results of an experimental investigation of expansion-tube flow characteristics performed with helium test gas and acceleration gas are presented. The use of helium, which behaves ideally for the conditions encountered in this study, eliminates complex real-gas chemistry in the comparison of measured and predicted flow quantities. The driver gas was unheated helium at a nominal pressure of 33 MN/m <sup>2</sup> . The quiescent test-gas pressure and quiescent acceleration-gas pressure were varied from 0.7 to 50 kN/m <sup>2</sup> and from 2.5 to 53 N/m <sup>2</sup> , respectively. The effects of tube-wall boundary-layer growth and finite secondary-diaphragm opening time were examined through the variation of the quiescent gas pressures and secondary-diaphragm thickness. Optimum operating conditions for helium test gas were also defined.					
17. Key Words (Suggested by Author(s))  Hypervelocity Expansion tube Shock tube Helium test gas			18. Distribution Statement  Unclassified - Unlimited		
			Subject Category 34		
19. Security Classif. (of this report) Unclassified	20. Security Classif. (of this page) Unclassified	21. No. of Pages 85	22. Price* \$6.00		

\* For sale by the National Technical Information Service, Springfield, Virginia 22161

NASA-Langley, 1978

86

90

50

**END**

**MAR 15 1979**